# SYNTHESES AND APPLICATIONS OF Mn-DOPED II-VI SEMICONDUCTOR NANOCRYSTALS

By

HEESUN YANG

A DISSERTATION PRESENTED TO THE GRADUATE SCHOOL
OF THE UNIVERSITY OF FLORIDA IN PARTIAL FULFILLMENT
OF THE REQUIREMENTS FOR THE DEGREE OF
DOCTOR OF PHILOSOPHY

UNIVERSITY OF FLORIDA

2003

Copyright 2003

by

Heesun Yang

This work is dedicated to my wife, Jaeock Kim; my daughter, Yoonji Yang; and my parents in Korea.

ACKNOWLEDGMENTS

Above all, I am greatly grateful to my adviser and my committee chairman, Dr. Paul H. Holloway, who has given me sincere guidance and support for four and one half years. The four and one half years that I worked for Dr. Holloway is the precious period in my life.

It is also my great honor to have four other professors (Dr. David Norton, Dr. Wolfgang Sigmund, Dr. Darryl Butt, and Dr. David Tanner) as my committee members.

For the sample characterizations, I am especially grateful to Eric Lambers and Kerry Siebein of the Major Analytical Instrumentation Center (MAIC) on XPS and HRTEM, respectively. I would like to thank Kwanghoon Kim for helping collect HeCd PL data. Also I am thankful to Dr. Kirk S. Schanze and his graduate student, Garry Cunningham, from the Department of Chemistry for lifetime measurements. In addition, I am thankful to Dr. Swadeshmukul Santra from the Department of Neurological Surgery for informative advice and discussion on biological applications of luminescent nanocrystals.

I also appreciate the valuable help from my colleagues in Dr. Holloway's group. I especially thank Joonbo Shim for useful discussion on electroluminescent devices, and Jungsik Bang for informative discussion on luminescent properties of nanocrystals. Another deep appreciation is expressed to Ludie Harmon for helping out with every detailed miscellaneous task.

Finally, the continual encouragement and support of my parent, wife, and daughter are deeply and sincerely appreciated.

TABLE OF CONTENTS

Page

ACKNOWLEDGMENTS ..... iv

LIST OF TABLES ..... ix

LIST OF FIGURES ..... x

ABSTRACT ..... xiv

CHAPTERS

1 INTRODUCTION ..... 1

2 LITERATURE REVIEW ..... 4

2.1 Fundamentals of Semiconductor Nanocrystals ..... 4
2.1.1 Quantum Confinement Effects ..... 5
2.1.2 Nanocrystal Surfaces ..... 9
2.2 Methods for Synthesis of Semiconductor Nanocrystals ..... 13
2.3 Photoluminescence of Semiconductor Nanocrystals ..... 17
2.3.1 Undoped Semiconductor Nanocrystals ..... 17
2.3.2 Doped Semiconductor Nanocrystals ..... 19
2.4 Hybrid Electroluminescent (EL) Devices ..... 24
2.4.1 Charge Transport Materials ..... 24
2.4.2 Electroluminescence from Semiconductor Nanocrystals ..... 26
2.5 Semiconductor Nanocrystals as Luminescent Biomarkers ..... 30
2.5.1 Conjugation of Semiconductor Nanocrystals with Biomolecules ..... 30
2.5.2 Surface Modification of Semiconductor Nanocrystals for Biomarkers ..... 33

3 PHOTOLUMINESCENT AND ELECTROLUMINESCENT PROPERTIES OF Mn DOPED ZnS NANOCRYSTALS ..... 35

3.1 Introduction ..... 35
3.2 Experimental Section ..... 36
3.2.1 Synthesis of ZnS:Mn Nanocrystals ..... 36
3.2.2 Fabrication of Electroluminescence Devices ..... 38
3.2.3 Characterizations ..... 39
3.3 Results and Discussion ..... 40
3.3.1 Size of ZnS:Mn Nanocrystals ..... 40
3.3.2 Band Gap and Photoluminescent Properties ..... 41

3.3.3 Electroluminescent Properties ..... 43
3.4 Conclusions ..... 49

4 SYNTHESIS AND CHARACTERIZATION OF CdS:Mn/ZnS SEMICONDUCTOR NANOCYRSTALS ..... 50

4.1 Introduction ..... 50
4.2 Experimental Section ..... 54
4.2.1 Materials ..... 54
4.2.2 Synthesis of CdS:Mn Nanocrystals ..... 54
4.2.3 Growth of ZnS Shell on CdS:Mn Nanocrystals ..... 55
4.2.4 Washing and Dispersion/Solubilization of Core/Shell Nanocrystals ..... 56
4.2.5 UV Irradiation Treatments ..... 56
4.2.6 Characterization ..... 56
4.3 Results and Discussion ..... 58
4.3.1 Comparative Studies of Non-Core/Shell and Core/Shell Nanocrystals ..... 58
4.3.2 Size-Controlled CdS:Mn/ZnS Core/Shell Nanocrystals ..... 63
4.3.3 Photoluminescence (PL) and Quantum Yield ..... 68
4.3.4 UV Irradiation and Photooxidation ..... 73
4.3.5 Luminescence Decay Kinetics ..... 82
4.4 Conclusions ..... 86

5 ELECTROLUMINESCENCE FROM HYBRID CONJUGATED POLYMERS-CdS:Mn/ZnS CORE/SHELL NANOCRYSTALS DEVICES ..... 88

5.1 Introduction ..... 88
5.2 Experimental Section ..... 90
5.2.1 Synthesis of CdS:Mn/ZnS Core/Shell Nanocrystals ..... 90
5.2.2 Fabrication of Hybrid Electroluminescence Devices ..... 91
5.2.3 Characterization ..... 92
5.3 Results and Discussion ..... 92
5.3.1 Size Information on Core/Shell Nanocrystals ..... 92
5.3.2 Electroluminescence and Electrical Properties ..... 93
5.3.3 Proposed Energy Diagrams of Devices ..... 101
5.4 Conclusions ..... 104

6 SILICA-OVERCOATED CdS:Mn/ZnS SEMICONDUCTOR QUANTUM DOTS FOR LUMINESCENT BIOMARKERS ..... 105

6.1 Introduction ..... 105
6.2 Synthesis of Water-Soluble Quantum Dots ..... 106
6.3 Results and Discussion ..... 107
6.3.1 Water-Soluble Quantum Dots and Formation of Silica Shell ..... 107
6.3.2 Effects of Silica-Overcoating on PL Emission ..... 113
6.3.3 Photooxidation of Silica-Overcoated CdS:Mn/ZnS Quantum Dots ..... 115
6.4 Conclusions ..... 117

7 CONCLUSIONS ..... 118

7.1 Competitive Reaction Chemistry-Based ZnS:Mn Nanocrystals ..... 118
7.2 Reverse Micelle-Based CdS:Mn/ZnS Core/Shell Nanocrystals ..... 119
7.3 Electroluminescence from CdS:Mn/ZnS Core/Shell Nanocrystals ..... 120
7.4 Silica-Overcoated CdS:Mn/ZnS Core/Shell Nanocrystals ..... 121

LIST OF REFERENCES ..... 122

BIOGRAPHICAL SKETCH ..... 129

LIST OF TABLES

Table page

2-1. Fundamental properties of II-VI bulk semiconductors....4

2-2. Various organic charge transport compounds used in organic LEDs ....26

4-1. Summary of CdS:Mn/ZnS core/shell nanocrystals synthesized under different conditions and Zn/Cd ratios from EDS/ICP versus XPS ....64

LIST OF FIGURES

Figure page

2-1. Variations of HOMO-LUMO transition energy as a function of CdSe nanocrystal size ..... 7

2-2. Evolution of molecular orbitals into band: from diatomic molecules to crystals ..... 8

2-3. Schematic of organic versus inorganic passivations ..... 12

2-4. Illustration of reverse micellar system ..... 15

2-5. Absorption properties of II-VI semiconductor nanocrystals ..... 18

2-6. PL properties of ZnS capped CdSe nanocrystals ..... 19

2-7. Radiative recombination paths in extrinsic luminescence ..... 20

2-8. Luminescent properties of ZnS:Mn nanocrystals ..... 22

2-9. Organic LED structures having two layers and three layers ..... 25

2-10. Chemical structures of some hole transporting conjugated polymers ..... 27

2-11. Double-layered PPV/CdSe nanocrystals EL device ..... 28

2-12. Schematic of several methodologies for bioconjugations ..... 32

2-13. Examples of luminescent quantum dots as biomarkers ..... 33

3-1. Experimental procedures for the synthesis of ZnS:Mn nanoparticles ..... 37

3-2. Schematic of an EL device structure ..... 38

3-3. XRD patterns from bulk and nanocrystalline ZnS:Mn ..... 40

3-4. Transmission electron microscope images and selected area diffraction pattern of ZnS:Mn nanocrystals ..... 41

3-5. PL excitation and emission spectra of ZnS:Mn bulk and nanocrystals ..... 42

3-6. Normalized PL emission spectra from ZnS:Mn nanocrystals with different Mn concentrations....44

3-7. Comparison of current-voltage data from EL devices with and without a PEDOT-PSS layer....45

3-8. Comparison of EL emission spectra from an ITO/PEDOT-PSS/PVK/Al device versus an ITO/PEDOT-PSS/PVK/ZnS:Mn/Al device....46

3-9. EL spectra from an ITO/PEDOT-PSS/PVK/ZnS:Mn NC/Al device at different applied voltages....47

3-10. Normalized EL spectra from an ITO/PEDOT-PSS/PVK/ZnS:Mn NC/Al device with different Mn concentrations....48

4-1. Overall experimental flowchart for synthesis of CdS:Mn/ZnS core/shell nanocrystals....55

4-2. UV-visible absorption spectra of *n*-dodecanethiol capped and ZnS capped CdS:Mn nanocrystals....60

4-3. XPS survey spectra of nanocrystals synthesized via methods 1 and 2....61

4-4. PL emission spectra of unpassivated, *n*-dodecanethiol capped, and ZnS capped CdS:Mn nanocrystals....62

4-5. PL excitation spectra of *n*-dodecanethiol capped and ZnS capped CdS:Mn nanocrystals....63

4-6. X-ray diffraction patterns from CdS:Mn/ZnS core/shell nanocrystals synthesized with different values of $W_1$....64

4-7. PL excitation spectra of core/shell nanocrystals synthesized with different values of $W_1$....65

4-8. XPS survey spectra of CdS:Mn, ZnS:Mn, and CdS:Mn/ZnS core/shell nanocrystals....67

4-9. Transmission electron microscope images of CdS:Mn nanocrystals without and with ZnS shell....69

4-10. PL emission spectra of ZnS-passivated CdS:Mn nanocrystals and ZnS-passivated undoped CdS nanocrystals....71

4-11. PL emission spectra of *n*-dodecanethiol-passivated CdS:Mn nanocrystals....72

4-12. Comparison of PL brightness from *n*-dodecanethiol- and ZnS-passivated CdS:Mn nanocrystals....73

4-13. Variations of PL emission intensity of *n*-dodecanethiol- and ZnS-passivated CdS:Mn nanocrystals versus time exposed to 400 nm UV light ..... 74

4-14. Variations of PL emission intensity of sample 2 versus time exposed to 400 nm UV light..... 75

4-15. Variations of PL emission intensity of sample 1 versus time exposed to 350 nm UV light..... 76

4-16. XPS scans for S 2p of CdS:Mn/ZnS nanocrystals UV-irradiated under different conditions..... 77

4-17. XPS scans for S 2s of nanocrystals irradiated in air and Ar under 366 nm UV for 3 hr..... 79

4-18. Variation of PL emission intensity of *n*-dodecanethiol-capped CdS:Mn/ZnS nanocrystals versus time exposed to 350 nm UV light..... 81

4-19. Decay curve recorded at an emission wavelength of 600 nm from CdS:Mn/ZnS nanocrystals..... 82

4-20. Time-resolved spectra of Mn emission of CdS:Mn/ZnS nanocrystals..... 83

4-21. Time-resolved emission spectra and steady-state emission spectrum of *n*-dodecanethiol-passivated CdS:Mn nanocrystals..... 84

4-22. Time-resolved emission spectra and steady-state emission spectrum of ZnS-passivated CdS:Mn nanocrystals..... 86

5-1. Hybrid EL device structures having PVK and PPV conjugated polymer..... 91

5-2. Transmission electron microscope images with low and high magnification of CdS:Mn/ZnS nanocrystals..... 93

5-3. EL spectra from an ITO//PEDOT-PSS//PVK//CdS:Mn/ZnS//Al hybrid device as a function of applied voltages..... 94

5-4. Peak fitting of PL emission and EL emission spectra by summation of two Gaussian peaks..... 95

5-5. Comparison of PL and EL emission spectra obtained from an ITO//PEDOT-PSS//PVK//CdS:Mn/ZnS//Al device..... 97

5-6. Current (I) versus voltage (V) relations from ITO//PEDOT-PSS//PVK// CdS:Mn/ZnS//Al EL device..... 98

5-7. Comparison of EL emission spectra as a function of applied voltages from ITO//PEDOT-PSS//PPV//CdS:Mn/ZnS//Al and ITO//PEDOT-PSS//PPV//Al EL devices..... 99

5-8. Comparison of PL emission and EL emission spectra obtained from ITO//PEDOT-PSS//PPV//CdS:Mn/ZnS//Al device structures....100

5-9. Comparison of I-V data from ITO//PEDOT-PSS//PPV//CdS:Mn/ZnS//Al and ITO//PEDOT-PSS//PPV//Al EL devices....101

5-10. Proposed energy level diagrams of an ITO//PEDOT-PSS//PVK// CdS:Mn/ZnS//Al device and an ITO//PEDOT-PSS//PPV//CdS:Mn/ZnS//Al EL device....103

6-1. Schematic of experimental procedures of synthesis of silica-overcoated CdS:Mn/ZnS and CdS:Mn quantum dots....108

6-2. Solubility tests of bare and silica-coated CdS:Mn/ZnS quantum dots in water with time....109

6-3. FT-IR spectra of bare and silica-coated CdS:Mn/ZnS quantum dots....110

6-4. Transmission electron microscope images of silica-overcoated CdS:Mn/ZnS quantum dots at low and high magnification....111

6-5. XPS survey spectra of bare and silica-overcoated CdS:Mn/ZnS quantum dots....113

6-6. PL emission spectra of unpassivated, silica-overcoated, and ZnS-passivated CdS:Mn quantum dots....114

6-7. Variation of 585 nm PL emission intensity of silica-overcoated CdS:Mn/ZnS quantum dots versus time exposure to 385 nm UV light....115

6-8. XPS spectra of bare and silica-overcoated CdS:Mn/ZnS quantum dots after 366 nm UV irradiated for 3 hr in air....116

Abstract of Dissertation Presented to the Graduate School
of the University of Florida in Partial Fulfillment of the
Requirements for the Degree of Doctor of Philosophy

SYNTHESES AND APPLICATIONS OF
Mn-DOPED II-VI SEMICONDUCTOR NANOCRYSTALS

By

Heesun Yang

December 2003

Chair: Paul. H. Holloway
Major Department: Materials Science and Engineering

Syntheses, characterizations, and applications of two different Mn-doped semiconductor nanocrystals, ZnS:Mn and CdS:Mn/ZnS core/shell, were investigated.

ZnS:Mn nanocrystals with sizes between 3 and 4 nm were synthesized via a competitive reaction chemistry. A direct current (dc) electroluminescent (EL) device having a hybrid organic/inorganic multilayer structure of an indium tin oxide (ITO) transparent conducting electrode, a (poly(3,4-ethylenedioxythiophene)/ poly(styrenesulfonate) (PEDOT-PSS) and a poly(N-vinylcarbazole) (PVK) bilayer hole transport film, a ZnS:Mn nanocrystal layer, and Al dot contacts was demonstrated to emit blue (~445 and ~495 nm) from PVK and yellow (~600 nm) light from Mn activator in ZnS. The EL emission spectrum was dependent upon both the voltage and Mn concentration, showing a decreasing nanocrystal to PVK emission ratio from 10 at 20 V to 4 at 28 V, and an increasing ratio from 1.3 at 0.40 mol % to 4.3 at 2.14 mol %.

Mn-doped CdS core nanocrystals were produced ranging from 1.5 to 2.3 nm in diameter with a ZnS shell via a reverse micelle process. In contrast to CdS:Mn nanocrystals passivated by *n*-dodecanethiol, ZnS-passivated CdS:Mn (CdS:Mn/ZnS core/shell) nanocrystals were efficient and photostable. CdS:Mn/ZnS core/shell nanocrystals exhibited a quantum yield of ~18 %, and the photoluminescence (PL) intensity increased by 40 % after 400 nm UV irradiation in air. X-ray photoelectron spectroscopy (XPS) data showed that UV irradiation of CdS:Mn/ZnS nanocrystals induces the photooxidation of the ZnS shell surface to $ZnSO_4$. This photooxidation product is presumably responsible for the increased PL emission by serving as a passivating surface layer. Luminescent lifetime data from the core/shell nanocrystals could be fit with two exponential functions, with a time constant of ~170 nsec for the defect-related centers and of ~1 msec for the Mn centers.

The CdS:Mn/ZnS nanocrystals with a core crystal diameter of 2.3 nm and a 0.4 nm thick ZnS shell were used as an electroluminescent material. EL devices were tested having a hybrid organic/inorganic multilayer structure of ITO//PEDOT-PSS//conjugated polymer//CdS:Mn/ZnS nanocrystal//Al. Orange from PVK device and green EL emission from poly(*p*-phenylene vinylene) (PPV) device were observed, respectively. These observations are shown to be consistent with the energy level diagrams of the EL devices.

The CdS:Mn/ZnS core/shell quantum dots are not water-soluble because of their hydrophobicity. Silica-overcoated CdS:Mn/ZnS quantum dots were synthesized to create water-soluble quantum dots. The amorphous and porous silica layer did not significantly modify the optical and photophysical properties of CdS:Mn/ZnS quantum dots.

# CHAPTER 1
# INTRODUCTION

Nanocrystals or quantum dots are nanometer scale particles that are neither small molecules nor bulk solids. Semiconductor nanocrystals whose radii are smaller than the bulk exciton Bohr radius exhibit the quantum confinement effect. Quantum confinement of both electron and hole in all three dimensions leads to an increase in the band gap with decreasing size, consequently creating remarkable change in the optical properties. The first report on the change of optical properties of a semiconductor as a function of crystal size dates back to the early 20th century.[1] Since then, a blue shift of the absorption spectrum from tiny crystals of AgX (X=I or Br) was observed compared to its bulk counterpart,[2,3] however, this unusual phenomenon was not understood in terms of a band structure. It was not until 1982 that the size-dependent optical properties observed in very small semiconductor materials originated from the variations in the density of electronic energy levels (quantum size effects).[4-6]

Tremendous advances in colloidal chemistry have been made over the past 20 years. Among them, the report by the Bawendi group[7] on the synthesis of CdSe luminescent semiconductor nanocrystals has initiated an enormous amount of research on II-VI (e.g., CdSe, CdTe, CdS, and ZnSe) and III-V (e.g., InP and InAs) semiconductor nanocrystals. The engineering of band gap of these undoped semiconductor nanocrystals as a function of size realized tunable emissions from UV (ultraviolet), visible to IR (infrared) spectrum ranges. Furthermore, continual effort has been focusing on the

manipulation of nanocrystal surface states to obtain highly efficient and photostable emission.

Although the optical properties of doped semiconductor (Mn-doped ZnS) nanocrystallines were published in 1983,[8] it was not until the publication by Bhargava's group that a considerable effort on doped semiconductor nanocrystals was made. Since Bhargava et al. reported in 1994 that Mn-doped ZnS nanocrystals exhibited dramatic lifetime shortening as well as high quantum yield,[9] doped semiconductor nanocrystals have been forming a new class of luminescent materials with a wide range of applications in displays, sensors, and lasers.[10]

The aim of the work described in this dissertation is to investigate Mn-doped II-VI semiconductor nanocrystals as a luminescent material and to utilize synthesized nanocrystals in the potential applications such as electroluminescent (EL) components and biological labels.

Chapter 2 reviews the two most important aspects of semiconductor nanocrystals (quantum confinement effects and surface states), general synthetic routes, and the previous studies on undoped versus doped nanocrystals. In addition, this chapter introduces the general understandings of two practical applications of luminescent semiconductor nanocrystals, i.e., hybrid EL devices and luminescent biomakers. In Chapter 3, the synthesis and characterization of Mn-doped ZnS nanocrystals are shown. Synthesized ZnS:Mn nanocrystals are utilized as an emitting layer in hybrid EL structure. Several ZnS:Mn nanocrystals with different Mn concentrations are prepared, and their effects on luminescent properties are discussed. In Chapter 4, a unique synthesis of CdS:Mn/ZnS core/shell nanocrystals is presented. And most importantly, core/shell

structured nanocrystals are shown to be advantageous over non-core/shell counterpart with respect to quantum yield and photostability. The comprehensive studies on UV irradiation-stimulated photooxidation of CdS:Mn/ZnS nanocrystals and its effects on the luminescent properties are described in detail. Finally, luminescence decay kinetics of CdS:Mn/ZnS core/shell nanocrystals are reported. Chapter 5 presents results on CdS:Mn/ZnS core/shell nanocrystal-based hybrid EL devices. Two hybrid EL devices are fabricated using different conjugated polymers, i.e., PVK and PPV, as a hole transport material. Different EL properties, depending on conjugated polymers used, are observed. Energy diagrams of hybrid EL device structures are proposed to interpret different EL behaviors and electrical properties. In Chapter 6, synthesis of water-soluble silica-overcoated CdS:Mn/ZnS quantum dots for luminescent biomarkers is presented. Successful formation of silica shell on CdS:Mn/ZnS quantum dot is achieved, and effects of silica shell on optical and photophysical properties of CdS:Mn/ZnS quantum dots are discussed. Finally, Chapter 7 draws conclusions.

# CHAPTER 2
# LITERATURE REVIEW

## 2.1 Fundamentals of Semiconductor Nanocrystals

Nanocrystals (quantum dots), lying in between the atomic/molecular unit and extended bulk crystalline solids, are intermediate in their physical dimensions. Over the past two decades semiconductor nanocrystals have been, in particular, of interest due to their unique properties and promising applications. Semiconductor nanocrystals as a function of the size exhibit substantial variations in physical, optical and electrical properties. An enormous range of fundamental properties is realized by manipulating the size of crystal in a material of a single chemical composition. Some fundamental properties of selected II-VI semiconductors are presented in Table 2-1. There are two major effects responsible for these size-dependent properties. First, in semiconductor nanocrystals the density of electronic energy levels as a function of the size varies systematically, known as quantum size effects.[5,11-14] Second, the number of surface atoms

Table 2-1. Fundamental properties of II-VI bulk semiconductors[15-17]

| | band gap, $E_g$ (300 K) (eV) | exciton Bohr radius, $a_B$ (Å) | relative dielectric constant, $\varepsilon$ | effective mass of electron, $m_e$ | effective mass of hole, $m_h$ | crystal structure | lattice const., $a$ (Å) | electron affinity, $\chi$ (eV) |
|---|---|---|---|---|---|---|---|---|
| **CdSe** | 1.70 | 54 | 9.4 | 0.13 | 11.7 | wurzite | a: 4.299<br>c: 7.010 | ~4.9 |
| **ZnSe** | 2.58 | 38 | 8.8 | 0.17 | | zinc blende | 5.667 | ~4.1 |
| **CdS** | 2.42 | 30 | 8.6 | 0.19 | 0.8 | zinc blende | 5.832 | ~4.4 |
| **ZnS** | 3.68 | 25 | 8.3 | 0.25 | 0.59 | zinc blende | 5.406 | |

versus interior atoms in semiconductor nanocrystals is a relatively large fraction. Both of these effects are important in the luminescent properties of nanocrystals, as discussed below.

**2.1.1 Quantum Confinement Effects**

Quantum confinement (size) effects are the widening of the energy between the highest occupied molecular orbital (HOMO)-lowest unoccupied molecular orbital (LUMO) gap with decreasing crystal size, and their implications for the electronic structure and photophysics of the crystals have generated considerable interest. In semiconductor crystals, the electronic excitation consists of a loosely bound electron-hole pair (Mott-Wannier exciton) through Coulombic interactions, which is usually spread over a dimension much larger than the lattice constant.[11] This bound state has an energy slightly lower than the energy of the band gap. As the diameter of the semiconductor crystals approaches this exciton Bohr diameter, the optical properties begin to change and quantum confinement effects set in.[12,13] The Bohr radius of the exciton ($a_B$) is given by the following equation:

$$a_B = \frac{\hbar^2 \varepsilon}{e^2}\left[\frac{1}{m_e} + \frac{1}{m_h}\right]$$

where is $\varepsilon$ is the dielectric constant, $\hbar$ is the reduced Plank constant, $e$ is the electronic charge, and $m_e$ and $m_h$ are the electron and hole effective mass, respectively.

When the radius of a nanocrystal approaches the size of excitonic Bohr radius, the motion of the electrons and holes becomes confined spatially to its dimensions. A created electron-hole pair must be compressed into such a small regime, i.e., into the quantum dot. Thus, additional energy is required to confine these localized charge carriers, raising its excitonic transition energy. On the other hand, the electron and hole are closer

together than in the macrocrystalline material, and thus the Coulombic interaction between electron and hole cannot be neglected.

There are two approaches to understand and explain quantum confinement effects quantitatively. The most widely discussed model is the effective mass approximation (EMA) first proposed by Efos[14] and later modified by Brus.[5] For a free particle, delocalized electron waves follow a quadratic relationship between wave vector $k$ and energy $E$:

$$E = \hbar^2 k^2 / 2m^*$$

where $E$ is the energy of a particle, $k$ is the wave vector, and $m^*$ is the effective mass. In the effective mass approximation, this relationship is assumed to hold for an electron or hole in the periodic potential well of semiconductor, implying that the energy band is parabolic near the band gap.[5,6,11] The size-dependent excitonic energy (band gap) shift of a nanocrystal with respect to bulk counterpart can be derived as

$$\Delta E_g = \frac{\hbar^2 \pi^2}{2\mu R^2} - \frac{1.8e^2}{\varepsilon R} = \frac{\hbar^2 \pi^2}{2R^2}\left[\frac{1}{m_e} + \frac{1}{m_h}\right] - \frac{1.8e^2}{\varepsilon R}$$

where $\Delta E_g$ (eV) is band gap shift of a nanocrystal compared to that of bulk, $R$ is the radius of nanocrystal, and $\mu$ is reduced mass of an electron-hole pair. The first term represents the particle-in-a-box quantum localization energy (or confinement energy) with a $1/R^2$ dependence and the second term represents the Coulomb interaction energy with a $1/R$ dependence. Consequently, the first excitonic transition (or band gap) increases in energy with decreasing size. Figure 2-1 compares the variations of the theoretical and experimental HOMO-LUMO gap as a function of CdSe nanocrystal size.[7] This EMA model is not quantitatively accurate as shown by the deviation from

experimental values, particularly for very smaller nanocrystals. This breakdown of the EMA model for such smaller nanocrystals is because the eigenvalues of the lowest excited states are for a region of the energy band that is no longer parabolic.[11,18]

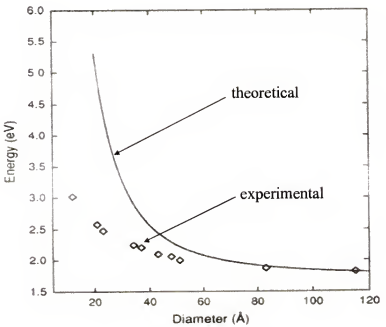


Figure 2-1. Variations of HOMO-LUMO transition energy as a function of CdSe nanocrystal size experimentally observed versus theoretically obtained using the simple effective mass approximation.[7]

The second approach uses a linear combination of atomic orbitals-molecular orbitals (LCAO-MO) theory, providing a natural framework to understand the evolution of clusters from molecules to bulk and the size dependence of the band gap.[11,19] Figure 2-2 illustrates this approach quantitatively. In the diatomic limit, the atomic orbitals (AOs) of the two individual atoms are combined, producing two (bonding and anti-bonding) molecular orbitals (MOs). In this approach nanometer-sized semiconductor nanocrystals are described as very large molecules. As the number of atoms increases, the number of sets of AOs increases, evolved from an incomplete, discrete energy band structure to continuous bands. The HOMO and LUMO form the quantum states at the top of the

valence band and the bottom of the conduction band, respectively. The size of nanocrystals places them intermediate between the atomic/molecular and extended bulk crystalline descriptions and properties. The energy difference between the HOMO and

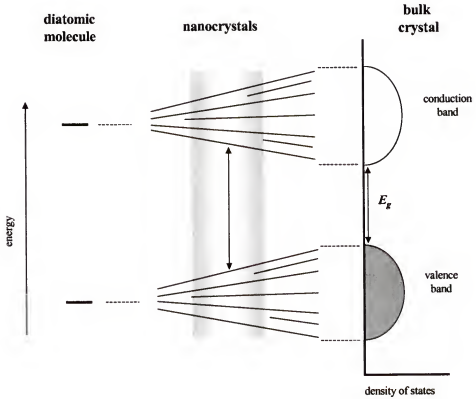


Figure 2-2. Evolution of molecular orbitals into band: from diatomic molecules to crystals.

LUMO (band gap) increases and the bands split into discrete energy levels with a decreasing number of atoms due to reduced mixing of atomic orbitals. Compared to the effective mass approximation, the LCAO-MO theory provides a good method to calculate the energy structure of even the smallest semiconductor nanocrystals.[11,18] However, it is not possible to calculate the energy level structure of large nanocrystals due to limitations of the currently available computers.

The degree of quantum confinement is determined by the ratio of the crystal radius ($R$) to bulk excitonic Bohr radius ($a_B$).[11,20-22] At crystal sizes greater than the excitonic Bohr diameter ($2a_B$), semiconductor crystals exhibit translational motion confinement of the fully coupled exciton due to a strong Coulombic interaction between the electron and hole, i.e., weak confinement regime. In contrast, at the crystal sizes much smaller than $2a_B$, the crystal is expected to exhibit complete decoupling of the electrons and holes, i.e., single-particle confinement behavior (or strong confinement regime). In the intermediate size range, the transition energies of photoexcited carriers in the crystal are determined by the relative strengths of the kinetic energy of confinement and the electron-hole Coulombic interaction.

**2.1.2 Nanocrystal Surfaces**

For nanocrystals in such a small size regime, a large portion of the atoms is located on or near the surface. For a 50 Å-CdS, ~15 % of the atoms sits on the surfaces.[11] This high surface-to-volume ratio of tiny nanocrystals suggests that surface properties should have significant effects on their structural and optical properties.[19] While the surfaces of nanocrystals appear to influence only mildly the optical absorption, it is well-known that the emission efficiency, spectrum, and time evolution are very strongly affected by the surfaces.[23,24] This is generally thought to result from the presence of surface states in the band gap arising from the surface non-stoichiometry, unsaturated bonds, etc.[23] The surface states are thought to trap electrons and/or holes, induce the nonradiative recombination of these charge carriers, and thus reduce the luminescence efficiency. In some cases, the surface states can also be involved in radiative transitions.

Passivation is the chemical process by which these surface atoms are bonded to another material with a much higher band gap, to reduce the energy levels inside the forbidden band gap. There are two major approaches, i.e., the use of organic versus inorganic passivating (capping) agents.

The surface passivation by organic molecules consists of coordination between capping molecules and anionic or cationic surface atoms. The organic capping agents not only contribute to surface passivation, but also increase the solubility in specific solvents and prevent the agglomeration of nanocrystals. In most sulfide nanocrystals, such as CdS and ZnS, thiolates ($R\text{-}S^-$) are used as capping agents by coupling sulfur group to cationic ($Cd^{2+}$ or $Zn^{2+}$) sites on the surface. One difficulty with organic capping arises in matching the organic ligands with surface atoms of the crystallites. Most organic capping molecules are conical or distorted in shape, and large and bulky. Thus the coverage of capping molecules on the surface atoms is limited by steric effects, depending on the curvature of surface.[19] Nanocrystals of CdSe have been capped by *n*-trioctylphosphine oxide (TOPO), where the surface Cd sites are coordinated by a monolayer of TOPO molecules. The capping coverage increases from half of all Cd sites on a flat crystal surface to all Cd sites on a 2 nm-CdSe nanocrystals.[19] It is generally very difficult to simultaneously passivate both anionic and cationic surface sites by organic capping, i.e., there are always some dangling bonds on the surface. Another disadvantage of organic capping is instability. The bonding at the interface between capping molecules and surface atoms is generally metastable, leading to the failure of bonding and further degradation upon the exposure to UV or visible light. This is known as the photooxidation process, and it has placed limits on the application of II-VI semiconductor

nanocrystals. The uncapped surface of CdS[25] or CdSe[26] nanocrystals are unstable when exposed to air and light due to surface photooxidation. For the photooxidation reaction shown below, oxygen and charge carriers are required at the nanocrystal surface. Photoexcited electrons/holes trapped by surface states and oxygen molecules physisorbed on the surface contribute to these photochemical reactions.[25,26]

$$CdS + O_2 \xrightarrow{h\nu} Cd^{2+} + SO_4^{2-}$$

$$CdSe + O_2 \xrightarrow{h\nu} Cd^{2+} + SeO_2$$

There has been widespread interest in the possibility of passivating nanocrystals with an inorganic shell (core/shell structured nanocrystals). In this way, the lattice matching between core and shell is important for the epitaxial growth of shell layer on the surface of core crystal. It was reported that in CdSe/CdS[27] or CdSe/ZnS[23,28] core/shell nanocrystals the CdS or ZnS shell on the CdSe core surface grew epitaxially. CdSe/CdS and CdSe/ZnS core/shell nanocrystals have a lattice mismatch of 3.9 % and 11.6 %, respectively. In certain CdSe/CdS superlattices, strain has been shown to persist for layers up to 50 Å without relaxation.[27] However, typical shell thickness in core/shell nanocrystals is normally <10 Å. Therefore, it is likely that even a relatively large lattice mismatch could be tolerated in epitaxial growth without relaxation. Organically and inorganically passivated nanocrystals are compared schematically in Figure 2-3. Growth of inorganic epitaxial shells on core nanocrystals can generate novel nanocrystal systems, where the surface-related defect states are eliminated by simultaneously passivating dangling bonds at both anionic and cationic surface sites. Furthermore, since the core material may be passivated by an inorganic material of wider band gap, a potential step (or band offset potential) of several tenths of an eV at the interface could reduce the

probability for charge carriers to reach the surface, i.e., the charge carriers are confined in the core material. This combination could lead to both enhanced photostability as well as improved luminous efficiency. The most efficient energy transition would be from the highest probability of electron/hole wave function overlap into the core due to carrier confinement, and of the recombination of these carriers away from the nonradiative traps/defects associated with nanocrystal surface. Since a robust inorganic shell replaces the weakly, metastably bonded organic molecules, better photostability is realized. Furthermore, the confinement of charge carriers into core material by potential barriers makes the charge carriers less accessible to surface states. Consequently, the charge carriers required for the photooxidation are deficient at surface sites, again leading to enhanced photostability.

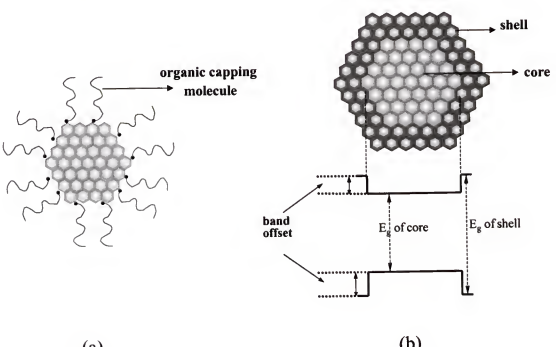


Figure 2-3. Schematic of (a) organic versus (b) inorganic passivations.

### 2.2 Methods for Synthesis of Semiconductor Nanocrystals

Many synthetic methods have been developed in preparing II-VI and III-V semiconductor nanocrystals. The solution chemical methods for the synthesis of these compounds are classified into three categories: controlled precipitation methods, synthesis in a structured medium, and molecular precursor methods.[16]

Controlled precipitation methods are based on traditional precipitation techniques, involving the formation of stable sol from the mixture of the chemical components of the respective ionic sources. The control of particle size can be achieved by introducing surfactants (organic molecules), or by varying the concentration of precursor and the reaction temperature. Typically, nuclei of a material are grown to the desired size and then passivated by one of many possible organic molecules. Competitive reaction chemistry (CRC), belonging to this category, has been widely used for the preparation of CdS and ZnS nanocrystals.[18,29,30] In the initiation step of the synthesis, a solution containing $Cd^{2+}$ or $Zn^{2+}$ ions is introduced into a solution containing $S^{2-}$ and $RS^-$ to generate small particles of CdS or ZnS. Subsequently a propagation step is used, in which particle aggregation competes with the growth-terminating reaction of the thiolate with the cations on the surface. Finally, the surface of nanocrystals is capped by covalent bonding of thiol groups to surface sites, preventing further aggregation of the nanocrystals. The eventual size of particle is determined by the relative rates of the propagation/termination reactions, and in turn by the relative concentrations of the initiating (sulfide) and terminating (thiolate) species.[30]

For synthesis in a structured medium (second category), a number of matrices have been devised for the preparation of semiconductor nanocrystals, e.g., zeolites, layered solids, molecular sieves, micelle/microemulsions, polymers, and glasses.[16] These

matrices can be viewed as nanoreactors that limit the crystal growth and thus determine the size. The properties of the nanocrystals are controlled not only by the confinement of the host material but also by the properties of the system such as the internal/external surface properties of the zeolite and the lability of micelles.[16] As a result of the spatial confinement of the medium employed, the range of particle sizes available is limited. For example, in zeolites the diameter of nanocrystals is limited by the pore size of the zeolite, typically smaller than 20 Å. One of the most popular techniques for the confined crystal growth in structured medium is the reverse micelles (RMs). The reverse micellar system consists of two immiscible liquids (water and oil). The nanometer-sized water droplets are dispersed in a continuous nonpolar organic solvent such as heptane or octane and stabilized by a monolayer film of surfactant molecules localized at the water/oil interface. Dioctyl sulfosuccinate, sodium salt (AOT) is one of the most widely used surfactants. Since AOT possesses both hydrophilic and hydrophobic groups in respective ending sides, numerous tiny water droplets form spontaneously and stably in the continuous oil phase. This reverse micellar system is heterogeneous on a molecular scale but is thermodynamically stable.[31] Reverse micelles are suitable reaction media for the production of nanocrystals, because water droplets serve as nanoreactors which favor the formation of small crystallites with narrow size distribution.[32-34] Continuous exchange of the micellar contents through dynamic collision enables the crystal growth to proceed, however growth of the particle beyond the dimensions of micelles is inhibited. As a final stage, the thiolate reagent is added to the continuous organic solvent to passivate the surface of the grown nanocrystals. A simplified schematic illustrating reverse micellar growth is shown in Figure 2-4. Because the semiconductor nanocrystals are assumed to

grow to approximately the same size as the water pool of the micelle, the micelle dimensions correlate with the final particle size. The size of the micelle and subsequently the size of the crystal are dictated by the water-to-surfactant ratio (W). A more precise relationship between W and the radius ($r$) of the micelle water pool is given by[35]

$$[(r + 15) / r]^3 - 1 = 27.5 / W$$

When the values of W are 5 and 10, resulting radii of micelle are 17 Å and 27 Å, respectively.

Finally, the molecular precursor method involves the pyrolysis of organometallic reagents, followed by homogeneous nucleation and slow growth. II-VI semiconductor nanocrystals such as CdSe and CdTe have been prepared via this method. In a synthesis

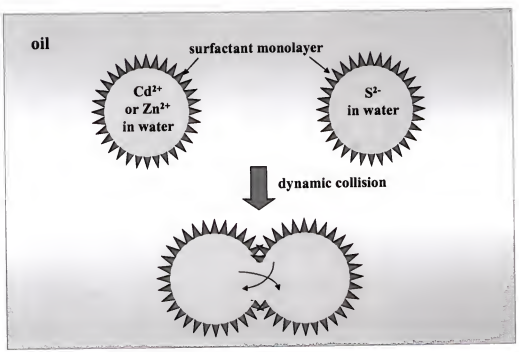


Figure 2-4. Illustration of reverse micellar system.

of CdSe nanocrystals, solutions of dimethylcadmium [$(CH_3)_2Cd$] and tri-*n*-octylphosphine selenide (TOPSe) are injected into hot tri-*n*-octylphosphine oxide (TOPO) in the temperature ranges of 120–300 °C, yielding TOPO capped CdSe nanocrystals. This injection of reagents into the hot reactor results in a short burst of homogenous nucleation. Subsequent crystal growth is known to be consistent with "Ostwald ripening." In the Ostwald ripening, the higher surface free energy of small crystallites makes them less stable with respect to dissolution in the solvent versus larger crystallites. The net result is slow diffusion of material from small particles to the surface of larger particles.[7] The TOPO acts as a coordinating solvent, stabilizing the resulting colloidal dispersion and electronically passivating the semiconductor surface. These TOPO capping groups provide a significant steric barrier to the addition of material to the surface of a growing crystallite, slowing the growth kinetics. The size of nanocrystals is controlled mainly by the reaction temperature and time, with larger sizes being obtained at higher temperatures and longer times. This synthetic method has advantages over other strategies, including monodispersity ($\sigma \cong 5$ %) and nearly perfect crystallinity. However, the TOPO method is limited by use of expensive, hazardous compounds. The organometallic compounds such as $(CH_3)_2Cd$ are extremely toxic, pyrophoric, unstable at room temperature, and explosive at elevated temperatures due to release of large quantities of gas.[36] For these reasons, less hazardous alternative precursors have been investigated. The use of cadmium oxide[36] or cadmium acetate[37] instead of $(CH_3)_2Cd$ was successful for the preparation of high quality CdTe, CdSe, and CdS nanocrystals.

## 2.3 Photoluminescence of Semiconductor Nanocrystals

### 2.3.1 Undoped Semiconductor Nanocrystals

Both undoped II-VI (CdSe, CdTe, CdS, and ZnSe) and III-V (InP, InAs) nanocrystals have been synthesized and studied. Among these, CdSe nanocrystals are undoubtedly the most widely studied due to their tunable emission in the visible range. The small band gap (1.74 eV) of bulk wurtzite CdSe allows tuning of nanosized CdSe from blue to red emission by the size-dependent quantum confinement effect. Initially nanocrystals were mainly prepared in aqueous solution with addition of stabilizing agents (thioglycerol or polyphosphate), but low quality nanocrystals were produced with poor luminescence efficiencies and broad size distribution. In 1993, Bawendi and coworkers[7] developed a unique synthesis of CdS, CdSe, and CdTe nanocrystals using the high-temperature organometallic procedure (TOPO technique), which resulted in high quality nanocrystals with a narrow size distribution and relatively high quantum efficiency. Figure 2-5 (a) shows the absorption spectra of ~20–30 Å diameter CdS, CdSe, and CdTe nanocrystals. All three samples show the effect of quantum confinement, i.e., the CdS, CdSe, and CdTe absorption edges are shifted to shorter wavelengths (higher energies) than their 512, 716, and 827 nm bulk band gaps, respectively. The systematic shift of the absorption spectrum of CdSe nanocrystals ranging from ~12 to115 Å in diameter is shown in Figure 2-5 (b). A quantum yield of ~10 % was reported from 35 Å diameter TOPO capped CdSe nanocrystals at room temperature.

Overcoating nanocrystallites with higher band gap inorganic materials has been shown to improve the photoluminescence quantum yields by passivating surface nonradiative recombination sites.[23,27,28,38] In addition, these core/shell composite nanocrystals are more robust than those passivated organically. Some important examples

of the core/shell structured nanocrystals reported include ZnSe[35] capped, ZnS[23,28,39] capped, or CdS[27] capped CdSe nanocrystals. Hines et al.[23] developed ZnS capped (overcoated) CdSe (i.e., CdSe/ZnS) core/shell nanocrystals that exhibit quantum yield of

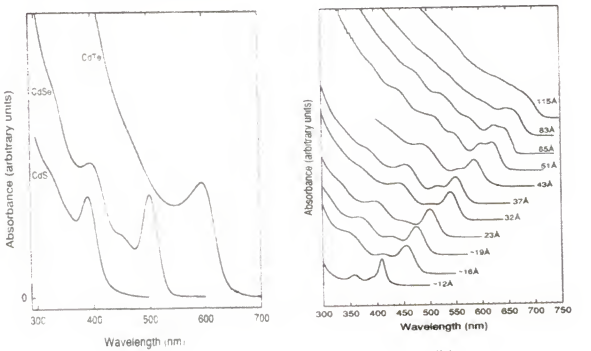


Figure 2-5. Absorption properties of II-VI semiconductor nanocrystals, i.e., (a) absorption spectra of CdS,CdSe, and CdTe nanocrystallites with ~20-30 Å in diameter and (b) evolutions of absorption spectrum of CdSe nanocrystals as a function of the size.[7]

50 %. Figure 2-6 (a) represents the photoluminescence spectra of band edge (band-to-band) transitions from TOPO capped versus ZnS capped CdSe nanocrystals, respectively.[23] While TOPO capped CdSe nanocrystal has a broad PL tail due to surface traps (700-800 nm), the fluorescence spectra of ZnS capped CdSe nanocrystals consist of a more intense peak with the absence of a surface state-related broad emission tail. Dabbousi et al.[28] also reported CdSe/ZnS composite nanocrystals, with the CdSe core ranging from 23 to 55 Å in diameter, to have a narrow band edge luminescence spanning

from 470 to 624 nm and high quantum yields of 30–50 %. Figure 2-6 (b) shows the colors emitted from a series of ZnS capped CdSe nanocrystals with various CdSe sizes excited with a handheld UV lamp.

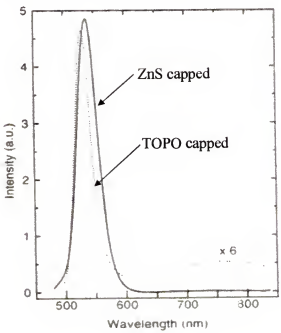

(a) (b)

Figure 2-6. PL properties of ZnS capped CdSe nanocrystals, i.e., (a) PL spectra of TOPO capped versus ZnS capped CdSe nanocrystals[23] and (b) a series of ZnS capped CdSe nanocrystals under UV excitation.

### 2.3.2 Doped Semiconductor Nanocrystals

Luminescence from the band-to-band transition, the recombination of an electron in the conduction band with a hole in the valence band, can be observed in undoped semiconductors such as GaAs, CdSe, and CdTe. Luminescence caused by intentionally incorporated impurities (activators) is classified as extrinsic luminescence in contrast to intrinsic (band edge) luminescence. The radiative mechanism in extrinsic luminescence is in principle an electron-hole recombination. This event can occur via either a conduction

band to acceptor state, donor state to valence band, or donor state to acceptor state recombination as shown in Figure 2-7.

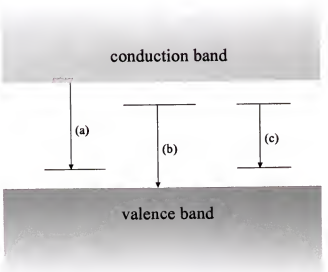


Figure 2-7. Radiative recombination paths in extrinsic luminescence.

When a dopant with quantum states remote from the valence and conduction band edges are added to the semiconductor host, another radiative mechanism is involved. This mechanism results in localized (atomic transition) luminescence, not band edge recombinations, since the luminescence excitation and emission processes are confined in a localized luminescence center. These localized transitions are classified as allowed (intershell) or forbidden (intrashell) based on the parity selection rule.[40] Some of examples for allowed transitions include $s \leftrightarrow p$ and $f \leftrightarrow d$ transitions. Forbidden transitions include $d \leftrightarrow d$ and $f \leftrightarrow f$ transition types. In a $d \leftrightarrow d$ transition, *d*-orbitals extend furthest from the atom nucleus and remain unshielded by any other electron orbital, thus they are strongly influenced by the surrounding host crystal. Due to this fact, the energy levels of the *d*-orbitals are split by the surrounding crystal field, leading to

band type emission.[41] $Mn^{2+}$, $Fe^{2+}$, and $Cr^{3+}$ impurity centers belong to this type of transition. In a $f \leftrightarrow f$ transition however, the $4f$ energy levels are shielded by the $5s$ and $5p$ electrons and are thus relatively unaffected by host lattice. This weak influence of surrounding host crystal on $f$ energy levels typically leads to sharp peaks (atomic-like) in the emission spectrum. Trivalent rare earth ions such as $Tm^{3+}$, $Er^{3+}$, $Tb^{3+}$, and $Eu^{3+}$ show these $f \leftrightarrow f$ type transitions.

The $Mn^{2+}$ ion, used in many luminescent materials, has a $d^5$ configuration. The $Mn^{2+}$ ion exhibits a broad peak emission, whose position depends strongly on the host lattice due to different crystal field strength ($\Delta$). The emission color can vary from green to deep red, corresponding to a $^4T_1$-$^6A_1$ transition.[41] Since this transition is not spin-allowed, the typical luminescent relaxation time of this emission is of the order of milliseconds.[41-43] Bulk ZnS:Mn has been widely used as a phosphor[44], particularly in alternating current thin film electroluminescence (ACTFEL) devices.[45-47] $Mn^{2+}$ ion $d$-electron states act as efficient luminescent centers while interacting strongly with $s$-$p$ electronic states of ZnS host into which external electronic excitation is normally directed. The subsequent transfer of electron and hole pairs into the electronic level of the $Mn^{2+}$ ion leads to the characteristic emission from the $Mn^{2+}$ $^4T_1$-$^6A_1$ transition.[44]

Bhargava et al.[9,44] first reported that Mn-doped semiconductor nanocrystals exhibited both high luminescence efficiencies and lifetime shortened from ms to ns. They reported a photoluminescent efficiency for 27–33 Å ZnS:Mn nanocrystals passivated with methacrylic acid of 18 % at room temperature, and the efficiencies increased with decreased size of crystals. They also reported that the luminescent decay rate of ZnS:Mn nanocrystals was at least 5 orders of magnitude faster than the corresponding $Mn^{2+}$

transition in the bulk crystals. The photoluminescent emission (PL) and excitation (PLE) data from ZnS:Mn nanocrystals are compared to those from bulk ZnS:Mn powder in Figure 2-8 (a).[9] A large shift to higher energy in the PLE spectra was observed for ZnS:Mn nanocrystals due to quantum confinement effects. Figure 2-8 (b)[9] shows the dependence of quantum yield on crystal size. They suggested that spatial confinement of the electron/hole in the nanocrystal resulted in a strong hybridization of the *s-p* states of the ZnS host and the *d* states of the $Mn^{2+}$ impurity. This hybridization results in fast energy transfer between the ZnS host and $Mn^{2+}$ impurity, producing a higher quantum efficiency. In addition, this hybridization caused the spin-forbidden $^4T_1$-$^6A_1$ transition of the $Mn^{2+}$ luminescent center to be less spin-forbidden, leading to a faster luminescent

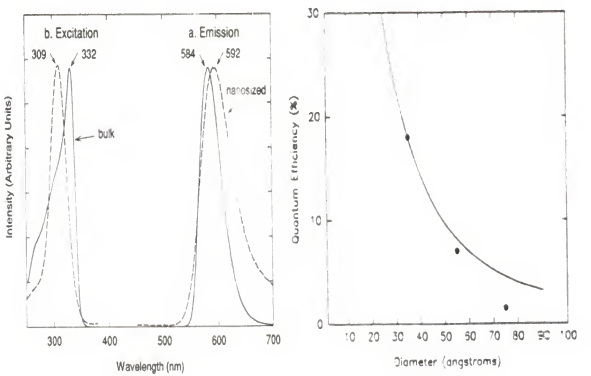


Figure 2-8. Luminescent properties of ZnS:Mn nanocrystals, i.e., (a) PL and PLE spectra of ZnS:Mn nanocrystal versus and bulk and (b) dependence of the quantum yield on the crystal size.[9]

relaxation rate. These spectacular results suggest that doped semiconductor nanocrystals may lead to a new class of luminescent materials.

The influence of quantum confinement on the luminescence of ZnS:Mn has had a great impact on the research on doped semiconductor nanocrystals. For other nanocrystallline semiconductors such as ZnS:Tb[48], ZnS:Eu[48], and ZnTe:Mn[49], the same trend of a reduced lifetime (from ms to ns) was reported. However, the theoretical explanation for this dramatic reduction in lifetime is lacking. In addition, later experiments failed in some cases to show such dramatic increases in quantum efficiency and decreases of lifetime. Data from Meijerink and coworkers[42,50-52] for ZnS:Mn nanocrystals contradict the high luminescent efficiencies and short lifetimes reported by Bhargava et al.[9,44] They report that the quantum yields from 3.8 nm diameter ZnS:Mn nanocrystals (room temperature synthesis) with different Mn concentrations range from 0.5 to 3.8 %, which are far below Barghava's reported value of 18 %. Also a decay time of 1.9 ms was observed for the $^4T_1$-$^6A_1$ transition of the $Mn^{2+}$. In fact, the decay curves could be fit with two exponentials with two distinct time constants of ~100 ns and ~1.9 ms. Meijerink et al. concluded that the short decay time constant should be ascribed to a defect-related emission of ZnS host, and not to the $^4T_1$-$^6A_1$ transition of $Mn^{2+}$. These results were confirmed by other research groups.[43,53] The nanosecond decay times reported by Barghava et al. for the $Mn^{2+}$ emission are most likely due to defects reflected by the broad emission tail with some overlaps with the $Mn^{2+}$ emission at ~590-600 nm.

Recently, luminescent semiconductor nanocrystals have been intensively investigated as electroluminescent (EL) components and luminescent biomarkers. In next

sections, the practical applications of luminescent semiconductor nanocrystals to these two main categories will be reviewed.

### 2.4 Hybrid Electroluminescent (EL) Devices

The integration of organic and inorganic materials into hybrid optoelectronic structures enables active devices that combine the diversity of organic materials with the high performance electronic and optical properties of inorganic nanocrystals.[54] Electroluminescece (EL) of inorganic semiconductor nanocrystal, combined with organic light emitting diodes (LEDs) structure, is a promising field for the application of luminescent nanocrystals.

#### 2.4.1 Charge Transport Materials

The operation of organic LEDs depends on the injection of holes from the anode and electrons from the cathode when a voltage is applied across the device. These injected electrons and holes move through the organic emitting layers until they meet each other and form an exciton. The exciton with the neutral excited state then relaxes into the ground state, resulting in light emission. However, unless the energy levels of the cathode and anode are extremely well matched to the molecular levels of the organic emitting compound, electron and hole currents are not balanced, leading to low device efficiency.[55,56] Therefore one of the most challenging design aspects of LEDs is how to bring electrons and holes together in small regions so that they recombine efficiently to emit photons without escaping or dissipating.[57] Considerably better carrier balance via enhanced electron and/or hole injection and transport, and consequently improvement of device efficiency could be accomplished from two- or three-layer structures by adding an electron transport layer (ETL) and a hole transport layer (HTL) surrounding a single emitting layer (EML). The main purposes of the incorporation of the charge transport

layer(s) are not only to limit the flow of electron (or hole) current into the HTL (or ETL), but also to lower the energy barrier for injection of charge carriers into the emitting layer. Figure 2-9 shows the typical energy band structures for a two- and a three-layer organic LED, respectively.

Several charge transport compounds that are widely used in organic LEDs are shown in Table 2-2. The organic materials are classified as small molecules (e.g., $Alq_3$, TPB) or conjugated polymers (e.g., PPV, PVK). Since these organic materials show semiconducting properties, with a HOMO-LUMO gap ranging from 1.5 to 3 eV, recombination within them leads to visible light emission and spectral overlap with emitting layers.

Unlike other compounds that act as both a charge transport and an emitting layer,

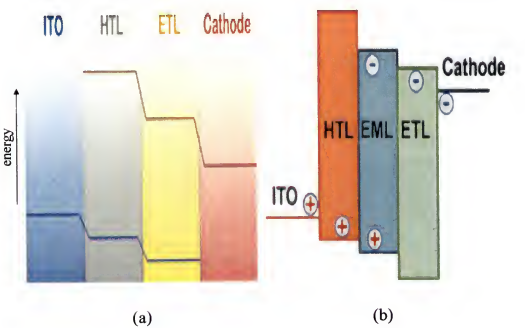


Figure 2-9. Organic LED structures having (a) two layers and (b) three layers.

Table 2-2. Various organic charge transport compounds used in organic LEDs [58-63]

| | |
|---|---|
| **hole transport materials** | poly(*p*-phenylenevinylene) (PPV) |
| | polyvinyl carbazole (PVK) |
| | tetraphenylbenzidine (TPB) |
| | N,N'-diphenyl-N,N'-bis(3-methyphenyl)-(1,1'-biphenyl)-4,4'-diamine (TPD) |
| | poly(3,4-ethylenedioxythiophene) /poly(styrene sulfonate) (PEDOT-PSS) |
| **electron transport materials** | 8-hydroxyquinoline aluminium ($Alq_3$) |
| | oxadiazole derivative (butyl-PBD) |

PEDOT-PSS exhibits only charge transport. PEDOT-PSS has a high ionization potential (or a low HOMO level), and therefore when placed between the anode and hole transporting layer, it leads to enhanced hole injection and lower operating voltages. It is also reported that this conducting polymer smoothes the indium tin oxide (ITO) surface and avoids direct contact between ITO anode and hole transport layer.[62] The chemical structure of some conjugated polymers used as hole transport layers are shown in Figure 2-10.

Inorganic semiconductor nanocrystals as an emitting component can be incorporated into organic LEDs, forming hybrid-structured EL devices. These charge transport materials play a crucial role in nanocrystal-based EL devices for better device performances.

### 2.4.2 Electroluminescence from Semiconductor Nanocrystals

In principle, the same electroluminescence (EL) mechanism used in organic LEDs can be applied to semiconductor nanocrystal-based EL devices. The electrons and holes

injected from respective electrodes would recombine inside the semiconductor nanocrystals, and characteristic light would be emitted as a result.

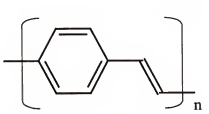

Poly(phenylene vinylene)
PPV

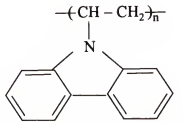

Poly(vinyl carbazole)
PVK

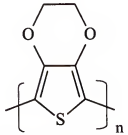

Poly(3,4-ethylenedioxythiophene)
PEDOT

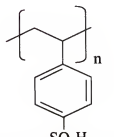

Poly(4-styrenesulfonic acid)
PSS

Figure 2-10. Chemical structures of some hole transporting conjugated polymers: PPV, PVK, and PEDOT-PSS.

Improvement by incorporation of charge transporting organic layers for efficient charge injection and transport has been demonstrated by comparing device structures with and without such layers. While a double layer structure consisting of a PPV HTL and a CdSe nanocrystal layer showed reasonable EL performance, a single CdSe nanocrystal layer device did not exhibit appreciable EL emission.[24] Figure 2-11 depicts the energy level diagram for the EL device consisting of double layers of PPV/CdSe nanocrystals (a), and the variation of EL emission spectra as a function of the applied voltages (b). Under an applied field, injected electrons and holes traverse respectively the CdSe nanocrystal layer and the PPV layer, and recombine resulting in characteristic light emission. The color is governed by where the recombination takes place, which can be

controlled by the magnitude of the external voltages, as shown in Figure 2-11 (b). Using the energy level diagram in Figure 2-11 (a), electrons traversing the CdSe nanocrystal layer are confronted with a barrier at the PPV/CdSe interface, leading to a build-up negative charge. These confined carriers promote electroluminescent efficiency both by locating the recombination zone away from the electrodes (where quenching may occur) and by creating large electric fields at the heterojunction that enhance tunneling of the electrons into the PPV and holes into the CdSe.[24] Consequently, recombination occurs throughout an extended recombination zone, leading to simultaneous emission from both

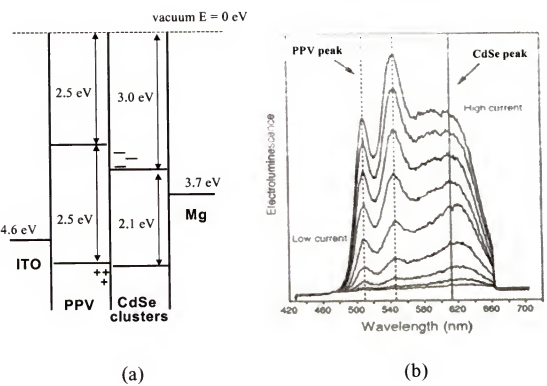


Figure 2-11. Double-layered PPV/CdSe nanocrystals EL device showing (a) energy level diagram and (b) voltage-dependent emission behaviors.[24]

CdSe and PPV. The external quantum efficiency (photons out divided by electrons in) of this PPV/CdSe device is known to be in the range of 0.001-0.01 %, and the typical device

lifetime is less than 10 min under bias in air.[24] The device lifetime is usually limited by the oxidation of the organic materials in both OLEDs and hybrid EL devices.[64,65]

While the organic HTLs are likely to limit hybrid EL device lifetime, the use of core/shell nanocrystal structures has led to better hybrid EL devices, resulting in a factor of 8 increase in external quantum efficiency (~0.1 %) and a factor of 10 increase in device lifetime over organically (TOPO) capped CdSe nanocrystals.[66] This improved stability of CdSe/CdS nanocrystals compared to TOPO capped CdSe might result from the presence of energy offsets between the core and shell valence/conduction bands, which would prevent the charge carriers from reaching the surface. In addition, carrier confinement should increase quantum efficiency.

Advanced designs of hybrid EL devices have been devised to obtain even higher efficiencies. One approach is a three layered hybrid EL structure consisting of only a single monolayer of CdSe/ZnS core/shell nanocrystals sandwiched between two organic films of $Alq_3$ (ETL) and TPD (HTL).[54] This structure is in contrast to previous devices that utilized thicker layers of nanocrystals, i.e., 10-20 nanocrystal diameters thick. The thick nanocrystal layer had a dual function of both transporting electrons and serving as the emitting layer. Poor electron conduction through nanocrystal multilayers leads to an injected charge imbalance, and consequently poor luminescence efficiency.[54] Furthermore, a high density of pinhole defects in the nanocrystal layer causes inconsistent device performance.[54] In contrast, the single monolayer nanocrystal EL device enables CdSe/ZnS to primarily participate in only the luminescence process, not charge conduction. External quantum efficiencies as high as ~0.5 % were reported. In another modification, nanocrystals embedded in conjugated polymers can be utilized for

hybrid EL device structure. Tessler and coworkers[67] fabricated spin-deposited composite films, where near-infrared (1.3 μm) emitting InAs/ZnSe core/shell nanocrystals were embedded in the conjugated polymer, poly[2-methoxy-5-(2-ethylhexyloxy)-1,4-phenylenevinylene] (MEH-PPV). By taking advantage of an efficient energy (charge) transfer from the MEH-PPV host to InAs/ZnSe nanocrystals, external quantum yield of ~0.5 % were obtained.

## 2.5 Semiconductor Nanocrystals as Luminescent Biomarkers

### 2.5.1 Conjugation of Semiconductor Nanocrystals with Biomolecules

Labeling of biomolecules using fluorescent tags is a common and essential field in the biological science.[68-78] Recent advances in nanomaterials have produced a new class of fluorescent markers (labels) using semiconductor quantum dots conjugated with biocognition molecules.[69] The well-developed high-temperature organometallic-derived CdSe/CdS or CdSe/ZnS core/shell quantum dots were demonstrated to have both dramatically enhanced quantum yields (up to 40–50 %) along with narrow full-width-at-half-maximum (FWHM) of emission and photostability under some conditions.[23,27,28] These remarkable properties of luminescent inorganic semiconductor quantum dots provide a promising possibility for the practical application of quantum dots to biological and biomedical fields. As fluorescent probes, luminescent quantum dots (or inorganic fluorophores) have several advantages over conventional organic fluorophores (dyes). Organic dye molecules suffer from several limiting factors.[71,72,75,76] First, their narrow absorption bands make it difficult to excite several colors with a single excitation source. Second, their large spectral overlaps between the emissions of dye fluorophores limit multicolor imaging process. Third, the emission intensity of organic dyes depends on their environment, indicating that photobleaching may be occurring. On the other hand,

the inorganic quantum dots exhibit large absorption bands, narrow spectral emission bands, and are (most importantly) photochemically stable.[72,75,76]

The bioconjugated quantum dots, accomplished by coupling luminescent colloidal nanocrystals to biomolecules such as proteins and DNA, have been used in immunoassay[74] and DNA hybridization.[79] Quantum dots are also emerging as a new class of fluorescent labels for *in vivo* bioassays.[69] An important property of quantum dots for *in vivo* applications is their high photostability, allowing real-time monitoring of intracellular processes over relatively long periods of time. With an inert layer of surface coating, the quantum dots are believed to be less toxic than organic dyes.[69]

For linkage of quantum dots to biomolecules, several methodologies can be used. First, the biomolecules may be linked covalently to functionalized surface of quantum dots, where a bifunctional ligand such as mercaptoacetic acid is utilized for attaching quantum dots to biomolecules. This is exemplified by standard carbodiimide-based chemistry to couple amine-functionalized biomolecuels (antibodies) such as IgG transferrin to mercaptoacetic acid (carboxyl)-functionalized quantum dots. Secondly, the biomolecules can also be coupled to quantum dots via noncovalent interactions such as electrostatic and hydrophobic attraction. One example of electrostatic interaction-based bioconjugation is synthetically engineered proteins with a linear polylysine chain directly adsorbed onto negatively charged quantum dots capped with dihydrolipoic acid (DHLA).[73,80] Also, hydrophobic TOPO capped quantum dots are coupled to biomolecules functionalized with modified acrylic acid polymer via hydrophobic attraction. The simple schematic of the bioconjugation methods is illustrated in Figure 2-12.

IgG and avidin (streptavidin) are two widely used molecules for bioconjugation in fluorescence labeling. Labeling of specific cellular targets by qunatum dot-IgG conjugate probes are visualized in Figure 2-13 (a).[75] Figure 2-13 (a) presents successful detection of a cancer marker (Her2), overexpressed on the surface of human breast cancer cells, with green (535 nm) emitting CdSe/ZnS quantum dot-IgG bioconjugates. The circle-type

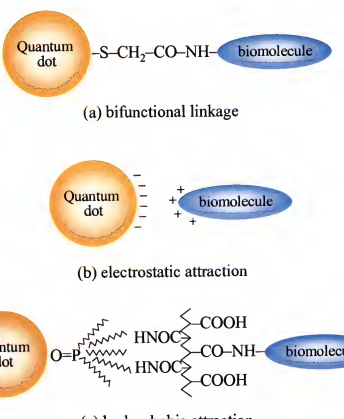


Figure 2-12. Schematic of several methodologies for bioconjugations.[69]

nuclei were stained in blue color by organic dyes (Hoechst 33342). CdSe/ZnS quantum dots and organic dyes (Alexa 488) are compared with respect to photostability in Figure 2-13 (b).[75] Nuclear antigens were labeled with red-emitting quantum dots-streptavidin

complex, and microtubules were labeled with green-emitting Alexa 488-IgG conjugate. Whereas labeling signals of Alexa 488 faded quickly and became undetectable within 2 min, the signals of quantum dots did not change for the entire 3 min UV illumination period.

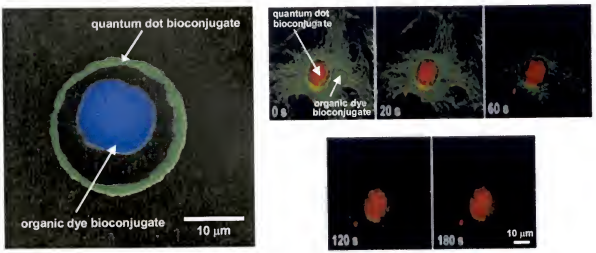


(a) (b)

Figure 2-13. Examples of luminescent quantum dots as biomarkers illustrating (a) detection of a cancer marker with green (535 nm) CdSe/ZnS quantum dot-IgG bioconjugates and (b) comparison of photostability of quantum dots versus organic dyes as a function of UV illumination period.[75]

**2.5.2 Surface Modification of Semiconductor Nanocrystals for Biomarkers**

Important technical challenges for using quantum dots for biological studies include: (i) designing hydrophilic quantum dots with surface chemistry adaptable to various biological applications; (ii) developing versatile techniques for selectively and specifically labeling cells and biomolecules; and (iii) demonstrating that quantum dots do not interfere with normal physiology. Among these challenges, modification of quantum dots surface chemistry for hydrophilicity is a prerequisite task. The poor solubility of luminescent semiconductor quantum dots in water, indicative of incompatibility with biological environments or aqueous assay conditions, has placed limits on their use.

Several synthetic strategies for surface functionlization have been used to solubilize inherently hydrophobic quantum dots in water. Mercaptoacetic acid, consisting of thiolated and carboxylic acid groups, was used as a coupling reagent with CdSe/ZnS core/shell quantum dots, where a thiolated group is linked to Zn atom on the surface, and the polar carboxylic acid group renders quantum dots hydrophilic, rendering the quantum dots soluble in water.[74] This type of surface functionalization, direct bonding of an organic coupling agent to a surface atom, is reproducible, rapid, and produces quantum dots with regular, well-oriented and thin coating. However, poor colloidal stability remains as a drawback, suggesting that desorption of mercaptoacetic acid molecules occurs slowly from the surface of quantum dots.[69,77] Instead, more extended core/shell chemistry has been utilized, where individual core/shell quantum dots are encapsulated completely by adding a third layer such as amorphous silica,[68,72] amphiphilic polymer,[70,75] or micelle-forming hydrophilic polymer-grafted lipids.[77] These encapsulation chemistries typically yield quantum dots with good colloidal stability, but the coating process is long and the uniform coating is difficult to control.[72,77]

# CHAPTER 3
# PHOTOLUMINESCENT AND ELECTROLUMINESCENT PROPERTIES OF Mn DOPED ZnS NANOCRYSTALS

## 3.1 Introduction

Nanocrystals or quantum dots are nanometer scale particles that are neither small molecules nor bulk solids. Semiconductor nanocrystals (NCs), which exhibit properties different from bulk materials, are a new class of material that hold considerable promise for numerous applications in the fields of electronics and photonics.[7,81-83] As the diameter of semiconductor crystal approaches its exciton Bohr diameter, the optical properties begin to change and quantum confinement effects become important. As a consequence of quantum confinement, the optical absorption onset of small semiconductor crystal occurs at higher energies (blue-shift) versus absorption of bulk materials.[12,13]

Due to the fascinating color tunability as a function of the size of semiconductor nanocrystals such as CdSe, CdTe, and CdS, most studies have been on undoped rather than doped semiconductor nanocrystals. However, since the observation of ~18 % photoluminescent quantum efficiency from Mn doped ZnS nanocrystal by Bhargava et al.,[9] doped semiconductor nanocrystals have been recognized as a promising form of luminescent materials.

ZnS:Mn is widely recognized as an efficient electroluminescent phosphor. $Mn^{2+}$ ion *d*-electrons act as efficient luminescent states which interact strongly with *s-p* electronic states of the host material into which the external electronic excitation is normally directed. The subsequent transfer of electron and hole pairs (excitons) into

electronic levels of the Mn ion leads to the characteristic emission from the $^4T_1$-$^6A_1$ transition of $Mn^{2+}$. It was proposed[9,10] that ZnS:Mn NC's high efficiency is a consequence of fast energy transfer of excited electron-hole pairs onto Mn impurity ions and a subsequent fast radiative recombination of *d*-electrons. An electronic confinement of *s-p* states of ZnS and corresponding increase in their spatial overlap with localized Mn *d*-electron states is believed to result in this rapid energy transfer of electron-hole pairs to the *d*-electron sites.

Recently, direct current electroluminescent devices using undoped or doped semiconductor nanocrystals have been proposed.[24,66,84-87] Most of the nanocrystal (NC) based EL devices consist of a hybrid organic/inorganic structure, where an inorganic nanocrystalline separate layer is used, or the nanocrystals are embedded in an organic conjugated polymer matrix (e.g., poly(*p*-phenylene vinylene) (PPV) or its derivatives).

In this study, the photoluminescent (PL) and hybrid organic/inorganic electroluminescence (EL) properties of ZnS:Mn nanocrystals are reported. The dependence of the EL properties upon voltage and Mn concentration are presented.

## 3.2 Experimental Section

### 3.2.1 Synthesis of ZnS:Mn Nanocrystals

The ZnS:Mn nanocrystals were synthesized using the competitive reaction chemistry (CRC) method, involving a propagation step of ZnS with growth terminated by adsorption of thiolate on the nanoparticle surface. The crystal size is controlled to the nanometer range by the relative rates of the propagation and termination reactions, which are controlled by the relative concentrations of initiating (sulfide) and terminating (thiolate) species.

Experimental procedures for the synthesis of ZnS:Mn nanoparticles are illustrated in Figure 3-1. Three stock solutions were prepared: (I) 1.8346 g of zinc acetate and 0.0087, 0.0173, 0.0346, 0.0519 g of manganese acetate in 80 mL of methanol and 20 mL of acetonitrile, yielding [Zn]=0.1 M, and Mn solution concentrations of 0.5, 1, 2, 3 mol % relative to Zn; (II) 0.3902 g of sodium sulfide in 25 mL of water and 25 mL of methanol, yielding $[S^{2-}] = 0.1$ M; and (III) 0.621 g of *p*-thiocresol in 50 mL of acetonitrile, yielding $[S^{2-}]$/[*p*-thiocresol] = 1 (molar ratio). To form nanoparticles, solutions (II) and (III) were stirred together first, then solution (I) was added in a dropwise fashion with continuous stirring. This immediately resulted in a white cloudy solution, which was stirred for 30 to 40 min, and then washed with methanol and centrifuged (8000 rpm, 7 min). For removal

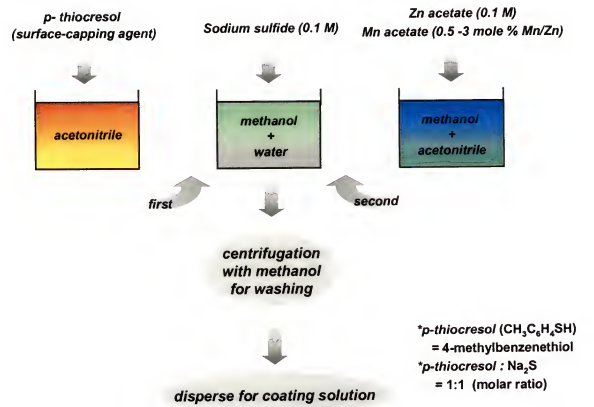


Figure 3-1. Experimental procedures for the synthesis of ZnS:Mn nanoparticles.

of by-products such as sodium acetate and residual surface capping species, the nanocrystals were exhaustively washed three or more times with methanol.

### 3.2.2 Fabrication of Electroluminescence Devices

After washing, ZnS:Mn nanocrystal was dispersed in acetone. A dc EL multilayer device, composed of layers of ITO/PEDOT-PSS/PVK/ZnS:Mn/Al was constructed. The schematic of an EL device structure is shown in Figure 3-2. The 50 nm thick poly(3,4-

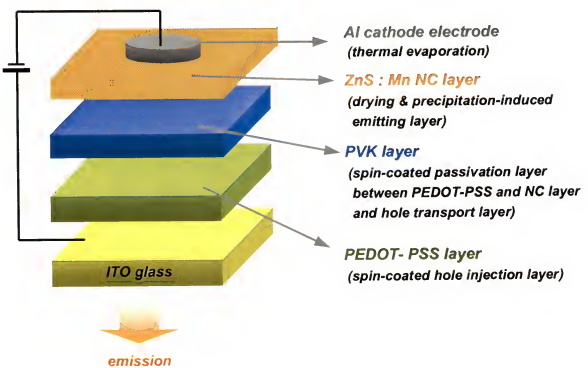


Figure 3-2. Schematic of an EL device structure.

ethylenedioxythiophene)/poly(styrenesulfonate) (PEDOT-PSS) layer was spin-coated onto the cleaned ITO-coated glass substrate. The 200 nm poly (N-vinylcarbazole) (PVK) layer was spin-coated on the PEDOT-PSS layer, followed by deposition of acetone-dispersed nanocrystals. The ZnS:Mn NC layer was dried using a hot plate in air. After drying, the nanocrystal layer had a thickness of 130 to 150 nm. The 300 nm thick Al

electrode was vacuum evaporated onto the nanocrystal layer to complete the device. The PEDOT-PSS layer lowered the hole injection barrier at the ITO interface.[62,63] However, nanocrystals directly deposited on the PEDOT-PSS layer exhibited a chemical reaction between the PEDOT-PSS and the *p*-thiocresol surface capping agent. Therefore the PVK layer, which is also known as a hole transport and light emitting species, was inserted as a passivation layer between the PEDOT-PSS and nanocrystal layers. To operate the device, positive and negative voltages were applied to the ITO and Al electrodes, respectively.

### 3.2.3 Characterizations

Information on structure and crystal size of the ZnS:Mn was obtained from a Philips APD 3720 x-ray powder diffractometer. Powder x-ray diffraction (XRD) spectra were collected in the step scan mode, typically with 2θ data collection and 1° steps. The accelerating voltage and current were 40 kV and 20 mA, respectively, for Cu $K_\alpha$ radiation. The nanocrystal size was estimated by the Scherrer formula from the FWHM of XRD peaks. 'Bulk' ZnS data were collected from 5 μm sized powder. Inductively coupled plasma (ICP) analysis with a Perkin-Elmer Optima 3200 RL was used to determine the actual Mn concentrations in ZnS nanocrystals.

A JEOL 200 CX transmission electron microscope (TEM) was used for imaging and direct determination of crystal size. For TEM samples, nanocrystals were dispersed in dimethylformamide (DMF) and a drop of the solution was placed on a carbon-coated copper grid, dried and placed in the microscope.

Photoluminescent (PL) excitation and emission spectra from ZnS:Mn 'bulk' and nanocrystals were measured at room temperature using a monochromatized Xe light source. A HeCd laser (325 nm) was also used to excite PL emission. The EL brightness

was characterized as a function of voltage or current across the device. EL emission was collected by a fiber optic and dispersed onto a CCD Si detector (Ocean Optics Spectrometer).

## 3.3 Results and Discussion

### 3.3.1 Size of ZnS:Mn Nanocrystals

The patterns of x-ray diffraction for ZnS:Mn 'bulk' and nanocrystalline materials are shown in Figure 3-3. The XRD pattern from cubic ZnS:Mn gave sharp intense peaks, with the Miller indices shown for selected peaks. Diffraction peaks from nanocrystals were very broad, but matched the Bragg angles measured for bulk ZnS (111), (220), and (311) planes. The size of nanocrystals was determined from the full width at half maximum (FWHM) via the Scherrer formula:

$$D = 0.9 \lambda / B \cos \theta$$

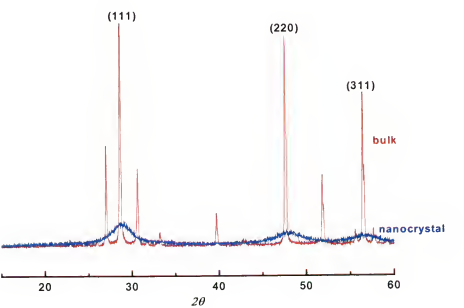


Figure 3-3. XRD patterns from bulk and nanocrystalline ZnS:Mn, with Miller indices labeling selected peaks.

where D is the crystal diameter (Å), λ is the wavelength of x-ray radiation (1.54 Å), B is the full width at half maximum (radian) of the peak, and θ is the diffraction angle. The obtained nanocrystal size was 3.1 nm. The nanocrystal size determined from the TEM images shown in Figure 3-4 is 4 nm. The selected area diffraction pattern (SADP) from the area in Figure 3-4 consisted of diffuse rings, indicating random orientation of nanocrystals.

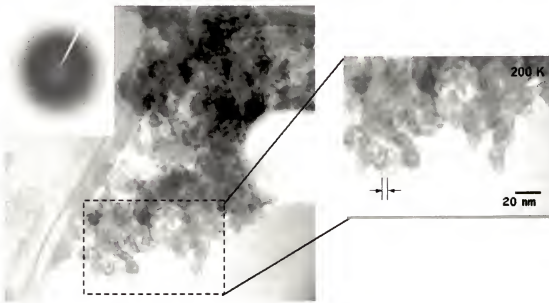


Figure 3-4. Transmission electron microscope images and selected area diffraction pattern of ZnS:Mn nanocrystals with a mean particle size of 4 nm.

### 3.3.2 Band Gap and Photoluminescent Properties

Photoluminescence (PL) excitation and emission spectra for ZnS:Mn 'bulk' and nanocrystals are compared in Figure 3-5. The PLE maximum shifted from 342 nm to 308 nm for 'bulk' versus nanocrystalline ZnS, respectively, a quantum shift of 0.37 eV. The TEM nanoparticle size of 4 nm was used in the effective mass approximation (EMA) model[5,14] to calculate an excitation maximum of 304 nm, in close agreement with

experimental data. It is well-known that the EMA model tends to overestimate the band gap for very small quantum dots, but appears to be accurate for dots of 4 nm.

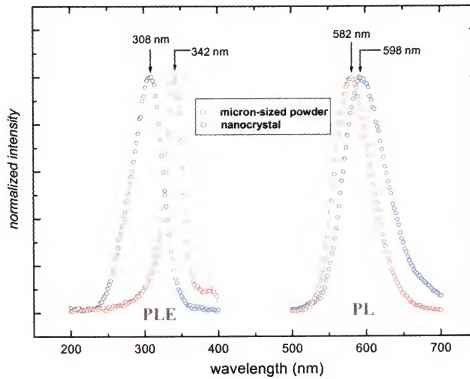


Figure 3-5. PL excitation and emission spectra of ZnS:Mn 'bulk' (micrometer) and nanocrystals (3-4 nm) sized powders. The maximum PL emissions occur at 582 and 598 nm for 'bulk' (micrometer size powder) and nanocrystals, respectively. The excitation maxima for PL emission are 342 and 308 nm for 'bulk' and nanocrystals, respectively.

Since photon emission from a doped semiconductor phosphor is governed by the impurity-related transition between its localized quantum levels in the band gap of the host material, the PL emission spectra from Mn (Figure 3-5) is consistent with emission from the $^4T_1$-$^6A_1$ transition in both 'bulk' and nanocrystalline ZnS:Mn. The only difference is a very small (~16 nm) red shift for emission from nanocrystals. It has been suggested[88] that this red (Stoke) shift of emission might be caused by a large density of surface states in the nanocrystals, or by a strong electron-phonon coupling in

nanocrystals. It seems more likely that a size-dependent crystal field effect is responsible for this red shift.

ZnS:Mn nanocrystals from Mn solution concentrations ranging from 0.5 to 3 mol % were synthesized to investigate the effect of Mn concentration on PL. ICP analysis showed that the actual Mn concentrations in ZnS nanocrystals (0.40, 0.78, 1.47, and 2.14 mol %) are lower than the Mn concentrations in the solution (0.5, 1, 2, and 3 mol %, respectively). No significant shifts of normalized PL emission were observed for different Mn concentrations. This result is consistent with the lack of emission shifts versus Mn concentration as reported by Chen et al.[88] It is well-known that the PL emission from bulk ZnS:Mn is red shifted as the Mn concentration is increased due to the Mn-Mn exchange interaction.[89] For ZnS:Mn nanocrystals, only a small fraction of Mn is initially incorporated during synthesis of the nanocrystals.[90] This limited degree of doping is thought to lead to weak Mn-Mn interaction and thus the absence of a PL emission shift versus Mn concentration. A broad emission band peaking at ~460 nm was observed from the nanocrystals (Figure 3-6) which is ascribed to radiative recombination involving localized surface states. This emission suggests that the *p*-thiocresol surface capping agent is not completely effective in preventing surface states at the nanocrystal surface.

**3.3.3 Electroluminescent Properties**

The operation of a polymer light emitting device (PLED) depends on the injection of holes from the anode and electrons from the cathode when a voltage is applied across the device. These injected electrons and holes move through the organic layers until they meet and recombine to the ground state, resulting in light emission. However, generally the highest occupied and lowest unoccupied molecular orbitals (HOMO and LUMO, respectively) are mismatched in energy with the work functions of the cathode and anode

contacts, resulting in a barrier to charge injection, high operating voltages, and a low device efficiency.[55,56] Better carrier balance from improved electron and hole injection

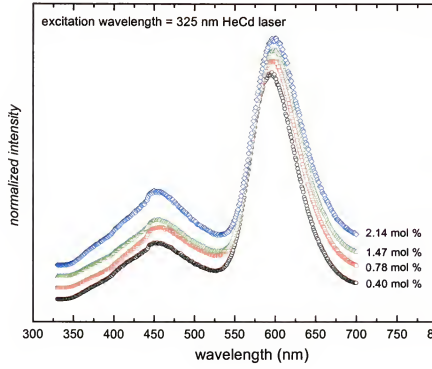


Figure 3-6. Normalized PL emission spectra from ZnS:Mn nanocrystals with different Mn concentrations.

and transport can be accomplished by adding electron transport (ETL) and hole transport layers (HTL), leading to improved device efficiency.[91,92] For semiconductor nanocrystal-based electroluminescence devices, the same processes of charge injection, transport and recombination must be accomplished as in PLEDs. Therefore, incorporation of organic compounds as layers for efficient charge injection and transport would be important to these devices. It was reported by Schlamp et al.[66] that the double layer structure of a separate poly(*p*-phenylene vinylene) (PPV) hole transport layer and a CdSe nanocrystal layer for electron transport and recombination showed a reasonable EL performance. In

contrast, a single layer structure of CdSe nanocrystals did not exhibit appreciable EL emission. The current-voltage (I-V) curves of EL devices with and without a PEDOT-PSS layer are shown in Figure 3-7. Obviously the PEDOT-PSS layer leads to enhanced current flow through the device. This is thought to result from the fact that PEDOT-PSS layer would both lower the energy barrier for hole injection from ITO electrode, as well as enhance the hole mobility and therefore the number of holes reaching the ZnS for

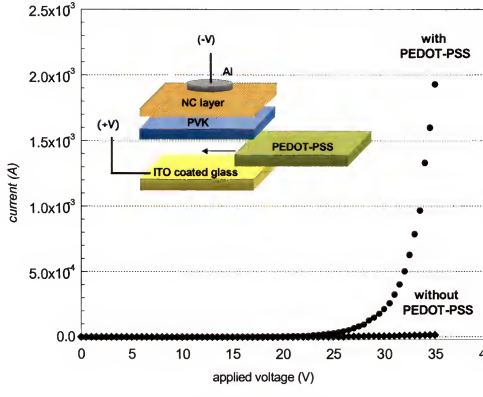


Figure 3-7. Comparison of current-voltage data from EL devices with and without a PEDOT-PSS layer. Note the lack of current in the devices without the PEDOT-PSS layer.

recombination. Typical EL spectra from devices consisting of ITO/PEDOT-PSS/PVK/Al and ITO/PEDOT-PSS/PVK/ZnS:Mn NC/Al are shown in Figure 3-8. In the structure without ZnS:Mn nanocrystals, EL emission from PVK is observed at 360-490 nm, consistent with literature reports of PVK emission wavelengths. When the

nanocrystalline layer is added, EL emission from Mn at ~600 nm ($^4T_1$-$^6A_1$ transition) is observed in addition to PVK peaks near ~445 and ~495 nm.

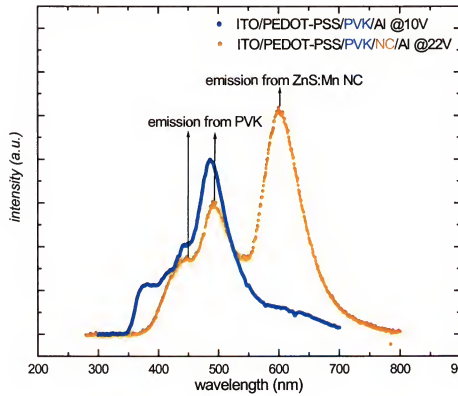


Figure 3-8. Comparison of EL emission spectrum from an ITO/PEDOT-PSS/PVK/Al device at an applied voltage of 10 V, with that from an ITO/PEDOT-PSS/PVK/ZnS:Mn/Al device at an applied voltage of 22 V. Note the emissions from both PVK and ZnS:Mn when nanocrystals are present in the device.

The intensity of EL emission increased as the applied voltages is increased as shown in Figure 3-9. This EL device was fabricated using nanocrystals with a Mn concentration of 2.14 mol %. Notice that at 20 V, the ratio of Mn to PVK emission is ~10 while at 28 V, this ratio has been reduced to ~4. This change in the ratio leads to a color shift, with yellow emission at low voltages, consistent with charge recombination

primarily in the ZnS:Mn nanocrystal layer. At higher voltages, the blue emission components from PVK increase and the color shifts to a yellow-green. A voltage-dependent EL color shift has also been reported from an ITO/PPV/CdSe/Mg EL nanocrystal device, where increased green emission from a PPV layer causes the shift.[24,66]

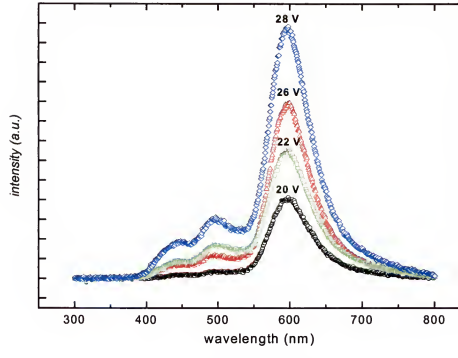


Figure 3-9. EL spectra from an ITO/PEDOT-PSS/PVK/ZnS:Mn (2.14 mol %) NC/Al device at different applied voltages. Note the increased ratio of emission intensities from PVK to ZnS:Mn when the voltage is increased.

It is speculated that the color shift results from electrons experiencing an energy barrier at the organic/ZnS:Mn interface, and consequent accumulation of negative charge. This accumulated charge could create large electric fields at the interface, which could enhance tunnel injection of electrons into the HTLs, leading to more emission from PVK.

The effects of Mn concentration on normalized EL emission are shown in Figure 3-10 where a constant operating voltage of 28 V was used. The wavelength of the Mn $^4T_1$-$^6A_1$ transition at ~600 nm was independent of the Mn concentration. There is an obvious dependence of emission peak shape upon the Mn concentration, with low Mn resulting in

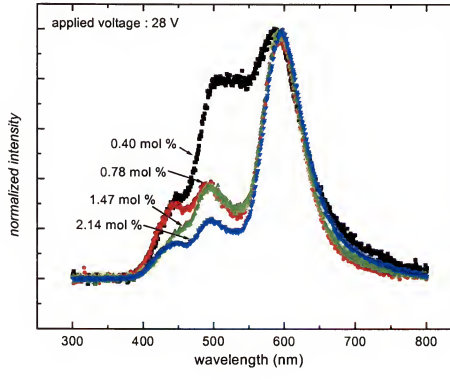


Figure 3-10. Normalized EL spectra from an ITO/PEDOT-PSS/PVK/ZnS:Mn NC/Al device with different Mn concentrations. Note the lack of shift in spectral distribution with increasing Mn concentration. Note also the higher emission intensity ratio from PVK to ZnS:Mn when the Mn concentration is lower.

a low ratio (1.3) of the emission due to Mn (~600 nm) to that from PVK (~495 nm). As the Mn concentration increased to 2.14 mol %, this ratio also increased to 4.3. Presumably this change in ratio simply reflects the increased probability of emission from ZnS:Mn versus PVK as the concentration of Mn centers increased. Since the PVK layer

is constant and independent of Mn concentration, its emission intensity remained constant.

### 3.4 Conclusions

ZnS:Mn nanocrystals capped with *p*-thiocresol were synthesized from a competitive reaction process which resulted in a particle size of 3 to 4 nm. The expected quantum confinement effects on photoluminescence excitation, a blue shift of 0.37 eV from 342 to 308 nm, was observed for nanocrystals versus 'bulk' micrometer sized ZnS particles. Radiative recombination from both Mn and localized surface states was observed in the PL emission spectrum, suggesting that the surface capping agent (*p*-thiocresol) was not completely effective in passivating the nanocrystal surfaces. Variation of the Mn concentration in the nanocrystals from 0.40 to 2.14 mol % did not affect the position or shape of the of PL emission spectrum. An electroluminescence nanocrystal device consisting of a multilayer structure of ITO/PEDOT-PSS/PVK/ZnS:Mn/Al, was characterized for EL emission. The PEDOT-PSS layer is critical for improved hole injection and transport, while the PVK layer eliminates reactions between the capped ZnS:Mn nanocrystals and the PEDOT-PSS layer. Emission from both the Mn in the ZnS nanocrystals, as well as from the PVK was observed. The ratio of emission from Mn to that from the PVK layer increased as the operating voltage decreased and as the Mn concentration increased. The origins of these changes in emission intensity ratios were discussed.

# CHAPTER 4
# SYNTHESIS AND CHARACTERIZATION OF CdS:Mn/ZnS SEMICONDUCTOR NANOCYRSTALS

## 4.1 Introduction

Luminescent semiconductor nanocrystals (quantum dots) are the subject of intensive investigation. In undoped II-VI semiconductors (e.g., CdSe, CdTe and ZnSe), the band gap is engineered by control of the crystal size that leads to tunable band-edge emission. By doping the nanocrystals with luminescent activators, the excitation can be tuned by quantum size effects, even though the activator-related emission energy is largely unchanged. Since a large portion of the atoms is located on or near the surface in the nanocrystals, the surface properties should have significant effects on their structural and optical properties.[93] For example, a 50 Å diameter CdS nanocrystal has ~15 % of atoms on the surface.[11]

The surface chemistry of luminescent II-VI semiconductor nanocrystals has been extensively investigated to improve the luminescent characteristics such as quantum efficiency and photostability. The surface states of nanocrystals are known as photodegradation and luminescent quenching sites.[23,25-27,94,95] The surface states are likely to trap electrons and/or holes and induce the nonradiative recombination of these charge carriers, leading to the reduction of luminescence efficiency. Besides, the surface states can also be involved in radiative transitions. In most of organically passivated II-VI semiconductor nanocrystals, a relatively large portion of unpassivated surface sites still exists due to the limited interaction of organic passivating species with either anionic or

cationic sites, resulting in partial coverage of the nanocrystal surface.[11] One difficulty from organic capping arises in matching the organic ligands with surface atoms of the nanocrystals. Furthermore, most of organic capping molecules are distorted in shape and large, bulky in size. Thus the coverage of capping molecules on the surface atoms is limited by the steric effect, depending on the curvature of surface.[93] In addition, the bonding at the interface between capping molecules and surface atoms is metastable and not strong enough, leading to the failure of bonding and further degradation.[93,96]

As an alternative to organically capped nanocrystals, inorganically capped (core/shell structured) nanocrystals have been proposed.[23,27,38,39] For inorganically passivated (or core/shell) nanocrystals, surface passivation of a core material is accomplished by inorganic shell material of wider band gap, often grown epitaxially on the core surface. Such a shell passivation could not only lead to significant reduction of surface-related defect states, but also to confinement of charge carriers into the core region due to the band offset potentials, resulting in more efficient and photostable luminescent nanocrystals.[23,27,28,38] Several undoped core/shell nanocrystals, such as CdSe/CdS,[27] CdSe/ZnS,[28] and ZnSe/ZnS,[38] have been shown to have much higher quantum efficiencies and better photostability when compared to unpassivated or organically passivated nanocrystals. Hines et al.[23] developed ZnS capped CdSe (CdSe/ZnS) core/shell nanocrystals, which exhibited dramatically enhanced quantum yields of 50 %. It was also reported[23] that this high quantum yield fluorescence is stable for months, and is fairly insensitive to the environment. A ZnSe/ZnS core/shell nanocrystal reported by Song et al.[38] showed a 2000% enhancement of luminescence quantum yield compared to bare ZnSe nanocrystals. CdS capped CdSe nanocrystal

reported by Peng et al.[27] exhibited a quantum yield near 100 % for well-synthesized nanocrystals. In particular, CdSe/ZnS nanocrystals with quantum yields of 30–50 % have been used for practical applications such as fluorescent biological labels.[68,71,74,77]

Among a number of possible synthesis strategies, high temperature (>300 °C) reaction-based organometallic chemistry is a well established route for the production of CdSe-based semiconductor nanocrystals.[23,27,28,97] Since this synthesis route provides sufficient thermal energy to anneal defects (nonradiative relaxation paths), high quality nanocrystals can typically be produced. However, due to the use of high temperature and organometallic precursors, this method has disadvantages with regard to costs and toxicity. The reverse micelle technique can also be used for the preparation of core/shell structured nanocrystals. Successful reverse micelle-derived syntheses of CdSe/ZnS,[39] CdSe/ZnSe,[35] and CdS:Mn/ZnS[98] core/shell nanocrystals have been reported. In the reverse micelle route, "water-in-oil" microemulsions are used consisting of nanometer-sized water pools dispersed in a continuous oil medium and stabilized by surfactant molecules. The nanocrystals are generated inside the water pools (nanoreactors) whose dimension limits the size of the nanocrystals.

Depending on the surface passivation, different PL characteristics as a function of UV irradiation have been proposed. It is well-known that ZnS:Mn nanocrystals passivated with polymers such as poly(vinyl alcohol) (PVA) or poly(vinyl butyral) (PVB), or monomers such as methacrylic acid (MA), exhibit more than 200 % increase of PL emission under UV irradiation.[52,90] This increase of PL emission was attributed to UV-stimulated increased polymerization and cross-linking, leading to more complete surface passivation. In addition, ~10 % increase of PL quantum efficiency of

unpassivated ZnS:Mn nanocrystals upon UV irradiation was reported by Bol et al.[52] They speculated that photooxidation of the ZnS nanocrystal surface in the presence of oxygen and water led to the formation of $ZnSO_4$ and/or $Zn(OH)_2$. These phases can serve as passivating barriers on ZnS nanocrystal surfaces. Manna et al.[99] reported that colloidal CdSe nanorods passivated by graded CdS/ZnS shells exhibited enhanced PL quantum yield by UV light excitation because of a structural rearrangement of chemical bonds at the core/shell interface via a photochemically activated process.

Since early reports by Bhargava et al.[9] on shortened (nanosecond range) lifetimes of Mn emission from ZnS:Mn nanocrystals versus bulk powder (millisecond range), the lifetime of impurity-related emission from doped semiconductor nanocrystals has been controversial. Bhargava et al.[9] also reported increased quantum efficiency of Mn emission, and proposed that strong hybridization between the *s-p* states of ZnS and *d* states of Mn, with subsequent fast energy transfer from ZnS to Mn, could explain the enhanced quantum yield. They also speculated that this hybridization could lead to an increased rate for the forbidden $^4T_1$-$^6A_1$ transition of Mn, resulting in a shorter lifetime. However, subsequent measurements of the Mn lifetimes from ZnS:Mn,[43,50] CdS:Mn,[100] and ZnSe:Mn[101] nanocrystals have shown normal relaxation times, leading to the conclusion that the hybridization process and lifetime reduction do not occur.

In all cases, inorganic passivation has only been reported using undoped semiconductor nanocrystals. Here, we report highly luminescent and photostable yellow-emitting CdS:Mn/ZnS core/shell nanocrystals via a reverse micelle method. The effective surface passivation by ZnS shell are evidenced by comparing organically capped CdS:Mn nanocrystals in terms of PL emission spectra and quantum yields. Based on the

observation from CdS:Mn/ZnS nanocrystals that PL emission increases with UV irradiation, a photochemical reaction (photooxidation) is suggested. Also, the luminescence decay kinetics, including relaxation lifetime, of CdS:Mn/ZnS nanocrystals will be discussed.

## 4.2 Experimental Section

### 4.2.1 Materials

Cadmium acetate dihydrate ($Cd(CH_3COO)_2 \cdot 2H_2O$, 98 %), manganese (II) acetate ($Mn(CH_3COO)_2$, 98 %), sodium sulfide ($Na_2S$), zinc acetate ($Zn(CH_3COO)_2$, 99.99 %), dioctyl sulfosuccinate, sodium salt (AOT, 98 %), heptane (99 %), and *n*-dodecanethiol ($CH_3(CH_2)_{11}SH$, 98 %) were purchased from Aldrich and used to synthesize or passivate the CdS:Mn nanocrystals.

### 4.2.2 Synthesis of CdS:Mn Nanocrystals

Each ($Cd^{2+}$ + $Mn^{2+}$)- and $S^{2-}$-containing standard aqueous solution was prepared by dissolving $Cd(CH_3COO)_2 \cdot 2H_2O$, $Mn(CH_3COO)_2$, and $Na_2S$ in water. The concentrations of $Cd^{2+}$ and $S^{2-}$ in water were 0.1 M and the ratio of $Mn^{2+}$ to $Cd^{2+}$ was fixed to 2 mole %. Then, each aqueous solution was stirred with an AOT/heptane stock solution (the concentration of AOT in heptane was 0.1 M). The water-to-surfactant molar ratios, $W_1$, for the formation of CdS:Mn core nanocrystals were 2.5, 5, and 10. CdS:Mn core nanocrystals were produced by injecting ($Cd^{2+}$ + $Mn^{2+}$)- micellar solutions into the $S^{2-}$-containing solution and mixing rapidly for 15 min. A surplus of $S^{2-}$ ions was maintained in the mixture to support subsequent ZnS shell growth. For a comparative study, *n*-dodecanethiol (organically) passivated CdS:Mn nanocrystals were synthesized with W=10 and the same Mn concentration. An excess of *n*-dodecanethiol in heptane was added into CdS:Mn nanocrystal micellar solution and mixed rapidly for 1 hr. Overall

experimental flowchart for synthesis of CdS:Mn/ZnS core/shell nanocrystals are shown in Figure 4-1.

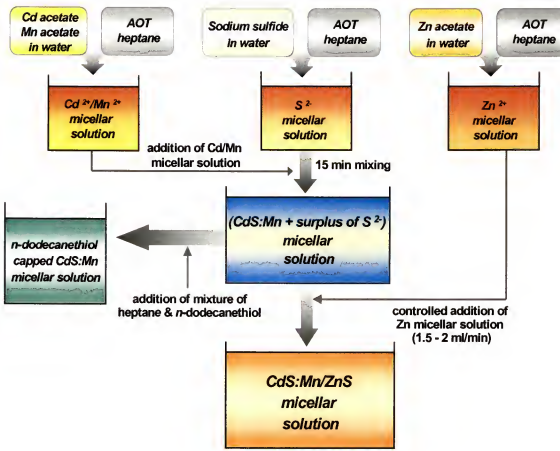


Figure 4-1. Overall experimental flowchart for synthesis of CdS:Mn/ZnS core/shell nanocrystals.

### 4.2.3 Growth of ZnS Shell on CdS:Mn Nanocrystals

A ZnS shell layer was grown on CdS:Mn core nanocrystals using a 0.26 M solutions of $Zn(CH_3COO)_2$ in water prepared as described above. The $Zn^{2+}$ aqueous solution was mixed with an AOT/heptane stock solution. The water-to-surfactant ratios, $W_2$, for $Zn^{2+}$ micellar solutions were 10 and 20. Values of $W_2$ higher than 20 resulted in unstable micellar solution with opacity and precipitation. The $Zn^{2+}$ micellar solution was dispensed by a transfer pump at a very slow rate of 1.5–2 ml/min into the CdS:Mn

nanocrystal micellar solution. The unwanted nucleation and growth of a separate ZnS phase was suppressed by maintaining a slow addition of the $Zn^{2+}$ solution. The molar ratio of ZnS to CdS in solution concentration was 8. Some CdS:Mn/ZnS nanocrystals were surface-modified with *n*-dodecanethiol to render the nanocrystals solubilized in chloroform via the procedure described in 4.2.2.

### 4.2.4 Washing and Dispersion/Solubilization of Core/Shell Nanocrystals

A small amount of methanol was added to the micelle solution to precipitate the nanocrystals. Precipitated nanocrystals were washed thoroughly using methanol and centrifugation (9000 rpm, 8 min.), then dispersed in methanol. Nanocrystals capped with *n*-dodecanethiol were solubilized in chloroform.

### 4.2.5 UV Irradiation Treatments

For photostability studies, a dried layer of CdS:Mn/ZnS on a glass substrate was UV-irradiated in air using a handheld UV lamp which provided 254 and 366 nm multiband emission with an intensity of 1200 and 1350 $\mu W/cm^2$, respectively. For UV irradiation in Ar, a sample was placed in a glove box filled with argon with ~1 ppm of oxygen and a dew point of –80 °C.

### 4.2.6 Characterization

Inductively coupled plasma (ICP) and energy-dispersive spectroscopy (EDS) analysis were used to determine a quantitative chemical composition of CdS:Mn/ZnS nanocrystals, especially Zn and Cd. A JEOL JSM 6400 electron microscope operated at 15 kV and a Perkin-Elmer Optima 3200 RL were used for EDS and ICP analysis, respectively. For ICP samples, core/shell nanocrystals were dissociated in the diluted nitric acid (70 vol. % in water). The solid-state (dried) CdS:Mn/ZnS nanocrystal film on a glass substrate was used for EDS measurements.

Crystal structure and size were determined using x-ray diffraction (XRD) patterns from a Philips MRD X'Pert system. XRD data were collected in the step scan mode, typically with a scan range of 15 °–80 °, a step of 0.01 °, and a grazing incidence angle of 1 °. A JEOL 2010F transmission electron microscope (TEM) operated at 200 kV was used for high resolution imaging and direct determination of crystal size. For TEM samples, the dilute solution of nanocrystals in methanol was dropped onto a carbon-coated copper grid, dried and placed in the microscope.

UV-visible absorption spectra were measured using a Perkin-Elmer Lambda 800 spectrometer. The nanocrystals solubilized in chloroform were used for measurements. PL emission spectra were collected from both a monochromatized 300 W Xe light and 325 nm HeCd laser as excitation sources. And, a monochromatized 300 W Xe light source was used for PL excitation (PLE) spectra and as the UV source to study PL emission intensity as a function of UV irradiation time. Dried nanocrystal films were used for all of these data.

Quantum yields of *n*-dodecanethiol- and ZnS-passivated CdS:Mn nanocrystals solubilized in chloroform were determined by comparing the integrated emission to those of Coumarin 6, Coumarin 30, and perylene at the excitation wavelength of 385 nm. Coumarin 6, Coumarin 30, and perylene were dissolved in ethanol, acetonitrile, and cyclohexane, respectively. The optical densities of the sample and reference solutions were 0.065 ± 0.003 at the excitation wavelength used. And then, final quantum yields can be obtained by the equation below:

$$QY = QY_s \frac{(1-10^{-At})}{(1-10^{-A})}\left(\frac{n}{n_s}\right)\left(\frac{EA}{EA_s}\right)$$

where $QY$, $A$, and $EA$ are quantum yield, absorbance, and integrated PL emission area of sample, respectively. The $n$ is refractive index of solvent. The subscript ($s$) represents the standard (reference) samples.

Perkin-Elmer PHI 5100 x-ray photoelectron spectroscopy (XPS/ESCA) was performed using both Al $K_\alpha$ x-ray (1486.6 eV) and Mg $K_\alpha$ x-ray (1253.6 eV). Survey scans were collected from 1100 to 0 eV with a step of 0.5 eV, a time/step of 30 ms, and a pass energy of 89.45 eV. High resolution scans were colleted with a step of 0.1 eV, a time/step of 50 ms, and pass energy of 35.75 eV. Dried films of CdS:Mn/ZnS were used for measurements.

For lifetime data, a source with an excitation wavelength of 370 nm and repetition rate of 200 kHz was used. The lifetime of emission at 600 nm was measured using 10 nm bandpass interference filter and a photomultiplier tube (PMT) in combination with a Tektronix 2440 oscilloscope. Also, time-resolved emission spectra were used for lifetime measurements. Time-resolved emission spectroscopic measurements were performed by using the third harmonic (355 nm) of a 10 ns pulsed Quanta-ray Nd:yttrium aluminum garnet (YAG) laser as the excitation source running at 10 Hz.

## 4.3 Results and Discussion

### 4.3.1 Comparative Studies of Non-Core/Shell and Core/Shell Nanocrystals

Several synthetic routes based on the reverse micelle have been used to produce CdS:Mn core/ZnS shell nanocrystals. Among them, the synthetic route (method 1) that was developed by Kortan et al.[39] for the synthesis of CdSe core/ZnS shell nanocrystal was used to produce the present CdS:Mn/ZnS nanocrystals. In this method, after Mn-doped CdS core nanocrystals were formed by mixing ($Cd^{2+}$ + $Mn^{2+}$)- and $S^{2-}$-containing micellar solutions as explained in 4.2.2, $Zn^{2+}$- and $S^{2-}$-containing micellar solutions were

injected partially (in steps of 1/10 of their total volumes) and alternately into the core nanocrystal solution. The ZnS shell layer was expected to grow on the core nanocrystal via partial and alternate injection of $Zn^{2+}$ and $S^{2-}$ micellar solutions. However, the ZnS shell layer did not grow on the core uniformly using 'method 1'. For the successful growth of a shell layer, a different synthetic route (method 2) was devised, where $Zn^{2+}$-containing micellar solution is added at a very slow rate (1.5-2 ml/min) into the CdS:Mn nanocrystal micellar solution (while maintaining a surplus of sulfur ions to support ZnS shell growth). The nucleation and growth of a separate ZnS phase were suppressed by the very slow addition of the $Zn^{2+}$ micellar solution. Note that the ratio of solution concentration of ZnS to CdS is 4 and the water-to-surfactant ratios of $W_1$ and $W_2$ are 10, and other synthetic parameters are identical to those specified in 4.2.2 and 4.2.3.

The UV-visible absorption spectra of CdS:Mn and CdS:Mn/ZnS nanocrystals are shown in Figure 4-2, along with the absorption edge expected from bulk CdS. There is a blue shift (~110 nm) of absorption shoulder for both types of nanocrystals in comparison with bulk CdS due to the quantum confinement effect. No significant differences can be detected between CdS:Mn and CdS:Mn/ZnS nanocrystals, which suggests that the electronic states of the CdS core material have not been modified. Lack of differences further suggests that there has been no significant incorporation of Zn ions into the CdS nanocrystals, i.e., that $Cd_{1-x}Zn_xS$ alloys have not been formed.

X-ray photoelectron spectroscopy (XPS) was used in conjunction with energy dispersive spectroscopy (EDS) to verify the core/shell structure of nanocrystals. XPS is a surface sensitive method,[102] while EDS is a 'bulk' method of analysis.[102] Thus XPS spectra should be dominated by the shell, while EDS spectra should exhibit the elements

in both the shell and the core structure averaged over many nanocrystal thickness. Figure 4-3 shows XPS (Al $K_\alpha$ radiation) survey spectra of the nanocrystals synthesized via the

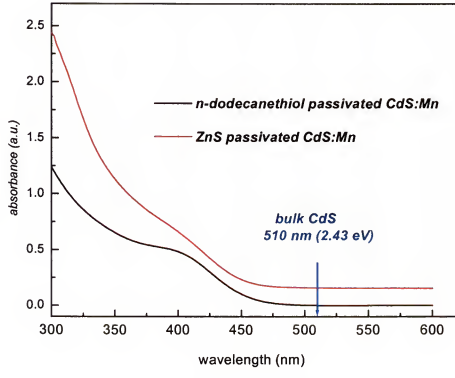


Figure 4-2. UV-visible absorption spectra of *n*-dodecanethiol capped (dotted line) and ZnS capped (solid line) CdS:Mn nanocrystals. The band gap of bulk CdS is indicated for a comparison.

two different synthetic routes (method 1 and 2). By comparison of the ratio of the intensities of the Zn $2p_{3/2}$ and Cd $3d_{5/2}$ peaks, 'method 2'-derived nanocrystals have a larger amount of Zn on the surface. Accurate atomic ratios of Zn/Cd were obtained by integrating the peak area and dividing by the atomic sensitivity factors.[103] The Zn/Cd ratios from 'method 1' and 'method 2' nanocrystals are 1.5 and 2.3, respectively. In contrast, the 'bulk' composition from EDS data showed a Zn/Cd ratio of 1.7 and 1.6 for 'method 1' and 'method 2' nanocrystals, respectively. Thus, the EDS data show that the

'bulk' Zn/Cd ratio was nearly constant, while the XPS data show that method 2 created a better ZnS shell.

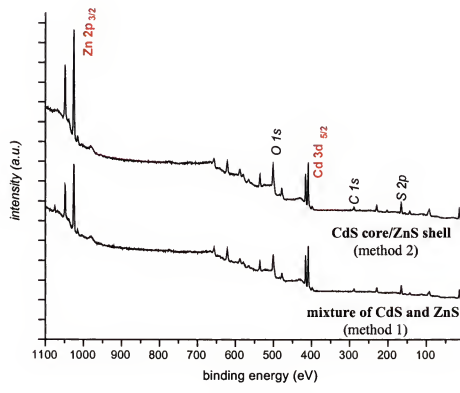


Figure 4-3. XPS survey spectra of nanocrystals synthesized via methods 1 and 2. Note that the peak-to-peak ratio of Zn $2p_{3/2}$ and Cd $3d_{5/2}$ is higher in method 2 than in method 1.

The PL emissions from unpassivated, *n*-dodecanethiol capped, and ('method 2') ZnS capped CdS:Mn nanocrystals are shown in Figure 4-4. The PL emission spectra were collected using a monochromatized 300 W Xe light excitation source. While the passivated CdS:Mn nanocrystals exhibit significant PL emission, the unpassivated CdS:Mn nanocrystals show negligible emission. Presumably the emission is weak due to the fact that most of the excited *e-h* pairs relax nonradiatively at the unpassivated surface states, therefore PL emission of unpassivated CdS:Mn nanocrystals is negligible. In

addition, nanocrystals produced by 'method 1' showed very dim PL emission, suggesting a lack of surface passivation of CdS:Mn core by the incomplete ZnS shell layer. Compared to PL emission from *n*-dodecanethiol capped CdS:Mn nanocrystals, CdS:Mn/ZnS core/shell nanocrystals prepared by 'method 2' show much more intense

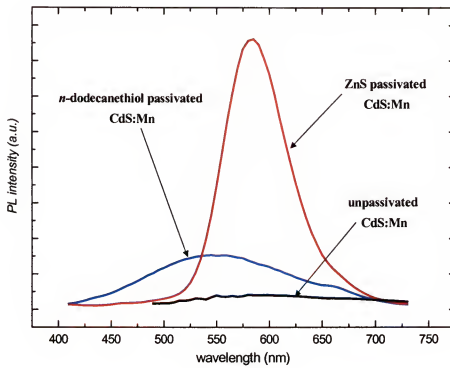


Figure 4-4. PL emission spectra of unpassivated, *n*-dodecanethiol capped, and ZnS capped CdS:Mn nanocrystals. The excitation wavelength for PL emissions is 400 nm for all.

and narrower PL emission. This enhancement of PL emission presumably results from suppression of nonradiative recombination due to reduced concentrations of surface states, consistent with successful growth of a ZnS shell layer on a CdS:Mn core. The PL excitation spectra of *n*-dodecanethiol and ZnS capped CdS:Mn nanocrystals are shown in

Figure 4-5. Both spectra exhibit the same excitation maxima at ~410 nm and a similar peak shape.

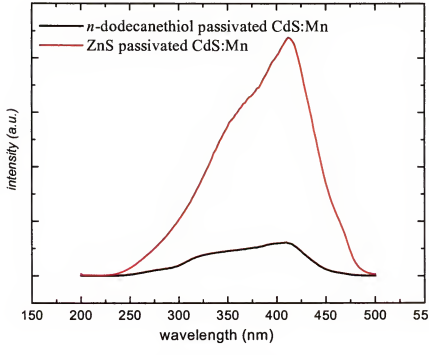


Figure 4-5. PL excitation spectra of *n*-dodecanethiol capped and ZnS capped CdS:Mn nanocrystals. The detected wavelengths for PL excitations are 570 and 585 nm for *n*-dodecanethiol capped and ZnS capped CdS:Mn nanocrystals, respectively.

### 4.3.2 Size-Controlled CdS:Mn/ZnS Core/Shell Nanocrystals

The CdS:Mn/ZnS core/shell nanocrystals prepared under different synthesis conditions and their Zn/Cd ratios from EDS/ICP versus XPS are summarized in Table 4-1. In the reverse micelle approach, crystal growth is confined to the nanosized-water pool, whose size is controlled by the water-to-surfactant molar ratio, W. CdS:Mn core nanocrystals with different sizes were prepared by varying $W_1$. XRD patterns and PL excitation spectra of samples 2, 3, and 4 are shown in Figures 4-6 and 4-7, respectively. As $W_1$ decreases, the size of the crystals decreases, as shown by broader peaks in the

XRD patterns and by larger shifts to higher energy in the PL excitation spectra. Also the color of CdS:Mn/ZnS nanocrystals in ambient light varies from white to yellow with an

Table 4-1. Summary of CdS:Mn/ZnS core/shell nanocrystals synthesized under different conditions and Zn/Cd ratios from EDS/ICP versus XPS

| samples | Zn/Cd ratio used | $W_1$ | $W_2$ | Zn/Cd ratio from EDS/ICP | Zn/Cd ratio from XPS |
|---|---|---|---|---|---|
| 1 | 8 | 10 | 10 | 5.5 | 6.6 |
| 2 | 8 | 10 | 20 | 5.4 | 6.4 |
| 3 | 8 | 5 | 20 | 5.3 | 6.4 |
| 4 | 8 | 2.5 | 20 | 4.6 | 5.5 |

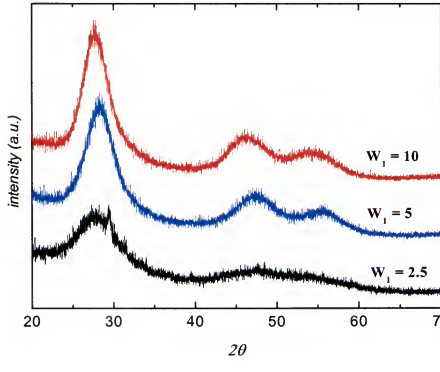


Figure 4-6. X-ray diffraction patterns from CdS:Mn/ZnS core/shell nanocrystals synthesized with different values of $W_1$.

increase of $W_1$. And as shown in Figure 4-7, smaller nanocrystals exhibit narrower peaks, presumably due to a narrower nanocrystal size distribution. The size of CdS:Mn core nanocrystals can be determined using the width of the XRD peaks reduced with the Debye-Scherrer equation. Since the shell layer does not affect the XRD peak from the

core,[27,99] the calculated average size is only for the CdS:Mn core, with resulting average diameters of 1.5, 2.0, and 2.3 nm for 2.5, 5, and 10 of $W_I$, respectively. Since both samples 1 and 2 were prepared with $W_I$=10, XRD and PLE spectra are indistinguishable.

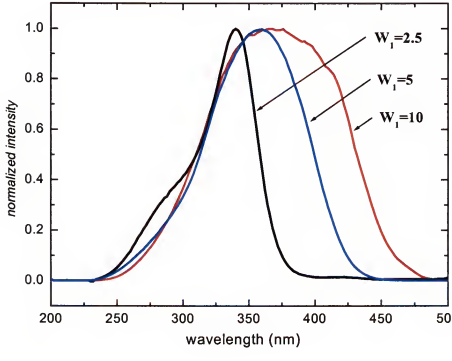


Figure 4-7. PL excitation spectra of core/shell nanocrystals synthesized with different values of $W_I$. The detected wavelength is 585 nm for all.

The relationship between W and the radius (r) of the micelle pool (and therefore nanocrystal size) is expressed as:[35]

$$[(r + 15) / r]^3 - 1 = 27.5 / W$$

On this basis for $W_I$ = 2.5, 5, and 10, CdS:Mn nanocrystals of 2.3, 3.4, and 5.4 nm in diameter, respectively, are expected. These data represent a significant deviation from the diameters determined from XRD full-width-at-half-maximum (FWHM) (Figure 4-6). An overestimate for the diameter from the above equation is consistent with results reported

by Behboudnia et al.,[104] who investigated the mismatch in size between the micelle pool and the actual size of resulting nanocrystals (specifically, reverse micelle-derived ZnS:Mn). It was observed that for pure ZnS and Mn-doped ZnS nanocrystals prepared from the identical micellar conditions, the size of ZnS:Mn nanocrystals is considerably smaller than that of pure ZnS, implying that the presence of the Mn impurity limits the size of ZnS nanocrystals, presumably due to the strain induced by the incorporation of Mn impurity.

As shown in Table 4-1, all series of samples have higher Zn/Cd ratios from XPS than those from EDS/ICP due to the spatial location of respective Zn and Cd atoms, supporting that the nanocrystals consist of layered structure. XPS (Mg $K_\alpha$ radiation) survey spectra of CdS:Mn, ZnS:Mn, and CdS:Mn/ZnS core/shell nanocrystals are shown in Figure 4-8. The same W of 10 was used for the preparation of CdS:Mn and ZnS:Mn nanocrystals, and CdS:Mn/ZnS core/shell nanocrystals are from sample 1 in Table 1. The primary Cd 3d and Zn 2p XPS lines are observed in Figure 4-8 (a) and (b), respectively, and those two lines are present in Figure 4-8 (c). Besides comparing the ratio of EDS (ICP)/XPS data, the ratios of Cd photoelectron and Auger electron peak intensities have been compared to further demonstrate that the core/shell structure was achieved in the CdSe/ZnSe[35] and CdSe/ZnS[28] nanocrystal systems. The observed intensities for photoelectron and Auger electrons are expressed as follows.

$$I = J_o N(z)_i \sigma_i Y_{i,n} F(KE) e^{-z/\lambda(KE)}$$

Where $J_o$ is x-ray flux, $N(z)_i$ is the number of *i* atoms, $\sigma_i$ is absorption cross section for atoms *i*, $Y_{i,n}$ is emission quantum yield for process *n* (photo or Auger electrons) for atoms *i*, F(KE) is an energy-dependent instrument response function, and $\lambda(KE)$ is the energy-

dependent escape depth (or attenuation length) for electrons traveling through a core or shell materials. Direct comparison of photoelectron and Auger electron signal intensities from the same atom (e.g., Cd) simplifies the above equation, eliminating the $J_o$, $N(z)_i$, and $\sigma_i$ terms. The intensity ratio $I_{core/shell}/I_{bare}$ can be defined, where $I_{core/shell}$ and $I_{bare}$ are the intensity ratios of the Cd photoelectron to Auger electron signals, i.e., $I_{Cd(PE)}/I_{Cd(Auger)}$, from core/shell and core nanocrystals, respectively. The value of $I_{core/shell}/I_{bare}$ is a function of the only relative escape depths ($\lambda$) of the photoelectron and Auger electron, and this depth is a function of their kinetic energies and the attenuating materials. The kinetic energies of Cd 3d and Auger (MNN) electrons are 849 and 375 eV, respectively. This energy difference leads to different escape lengths in the ZnS shell on the CdS:Mn

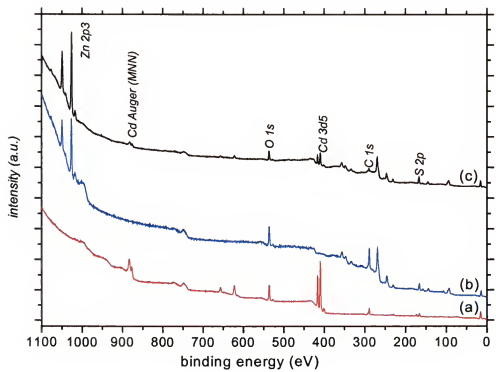


Figure 4-8. XPS survey spectra of (a) CdS:Mn, (b) ZnS:Mn, and (c) CdS:Mn/ZnS core/shell nanocrystals.

nanocrystals. Specifically, the low energy Cd Auger (MNN) electrons will be attenuated more by the ZnS layer than will the higher energy Cd 3d electrons. The observed $I_{core/shell}/I_{bare}$ value of $1.2 \pm 0.03$ is consistent with the presence of a ZnS shell on the CdS:Mn nanocrystals.

Transmission electron microscope images of CdS:Mn nanocrystals without and with ZnS shell (sample 1) are shown in Figure 4-9 (a) and (b), respectively. From these images, the average diameter of CdS:Mn nanocrystals without a ZnS shell is found to be ~2.5 nm, which is consistent with XRD diameter (2.3 nm). Similarly, the average diameter of CdS:Mn/ZnS core/shell nanocrystals was measured to be ~3.1 nm (Figure 4-9 (b)). Since a well-defined interface between CdS core and ZnS shell could not be distinguished, the thickness of the ZnS shell was difficult to obtain directly. Instead, the difference between the TEM and XRD diameters (0.4 nm) is attributed to the ZnS shell thickness (~1.5 monolayers of ZnS). Three XRD diffraction peaks from the nanocrystals (Figure 4-9 (c)) matched those of bulk zinc blende CdS, corresponding to the (111), (220), and (311) planes.[105] Also the inset in Figure 4-9 (b) shows a nanocrystal with a zinc blende structure, where $(1\bar{1}0)$ and (110) planes intersect at 90 °. The continuity of the crystal lattice over the entire particle indicates epitaxial growth of the ZnS shell on the CdS core. Due to small thickness of the ZnS layer (0.4 nm), the 7.1 % lattice mismatch between zinc blende CdS and ZnS is not expected to cause lattice relaxation.

**4.3.3 Photoluminescence (PL) and Quantum Yield**

A typical PL emission spectrum (collected from 325 nm HeCd laser excitation), observed from samples 1, 2, or 3, is shown in Figure 4-10 (a), showing a sharp Mn emission due to $^4T_1 - ^6A_1$ transition. In addition, there is significant trailing emission at

higher wavelength, suggesting that other radiative transitions may be active. This trailing emission can be found in both bulk and nanocrystalline ZnS:Mn,[106] and has been

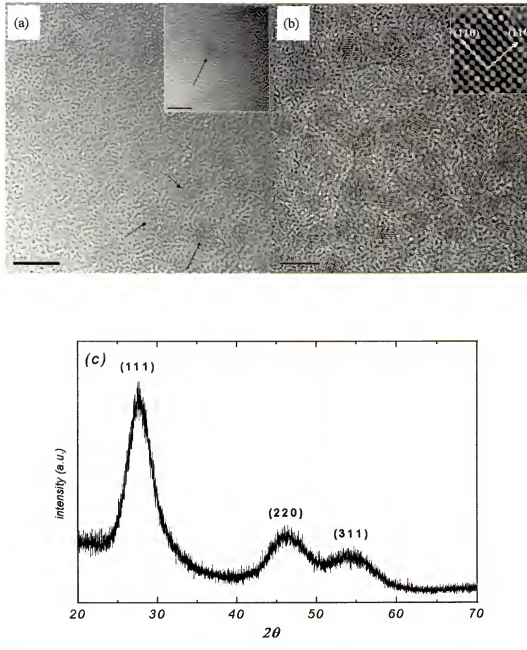


Figure 4-9. Transmission electron microscope images of CdS:Mn nanocrystals (a) without and (b) with ZnS shell. Figure 4-9 (c) shows three XRD diffraction peaks from nanocrystals, matching those of bulk zinc blende CdS. All length bars indicate 5 nm. The inset in (a) is a CdS:Mn nanocrystal without ZnS shell. The inset in (b) is a CdS:Mn/ZnS core/shell nanocrystal viewed along the [001] zone axis and (1$\bar{1}$0) and (110) planes are intersecting at 90 °.

attributed to emission at internal defects, such as sulfur vacancies.[107,108] Interestingly, the core/shell nanocrystals synthesized with a $W_I$ of 2.5 exhibited remarkably low PL emission as compared to those synthesized with a $W_I$ of 5 or 10. This indicates that the incorporation of Mn ions into extremely small nanocrystals (average size estimated to be 1.5 nm which is only ~100 atoms) is difficult. Difficulty of impurity doping in smaller nanocrystals has been reported,[109] and attributed to the fact that lattice deformation due to doping is more difficult to accommodate in small versus larger particles. This is consistent with the report by Smith et al.[43] that reverse micelle-derived 1.2 nm diameter Mn-doped ZnS nanoclusters showed negligible Mn-related emission at ~600 nm relative to surface-related defect emission at 400–450 nm. Another PL emission spectrum from undoped CdS core/ZnS shell nanocrystals is shown in Figure 4-10 (b), where broad, featureless defect-related emissions dominate. The emission intensity (at 600 nm) of Mn-doped core/shell nanocrystals is 60 times brighter than that from undoped crystals. Since close attention was paid to eliminate the possibility of Mn contamination from reaction vessels in undoped samples, the maximum emission at ~600 nm should not be involved with Mn impurity. These data indicate that several defect states exist in core/shell nanocrystals. The presence of these defect emissions from CdS core/ZnS shell nanocrystals will be discussed below with respect to the lifetimes measured from CdS:Mn/ZnS nanocrystals.

PL emission spectrum, obtained using 325 nm HeCd laser excitation, of *n*-dodecanethiol-passivated CdS:Mn nanocrystals is presented in Figure 4-11, and exhibits different peak positions and bandwidths from that of ZnS-passivated CdS:Mn

nanocrystals (Figure 4-10 (a)). The $Mn^{2+}$ $^4T_1$-$^6A_1$ transition at ~600 nm is observed from both nanocrystalline samples. In addition to the Mn emission at ~600 nm, emission from

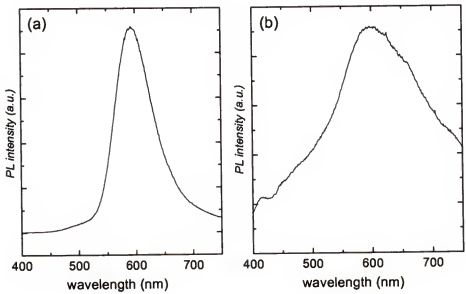


Figure 4-10. PL emission spectra of (a) ZnS-passivated CdS:Mn nanocrystals and (b) ZnS-passivated undoped CdS nanocrystals. The 325 nm HeCd laser excitation was used.

a surface-related defect (shallow trap) is observed at ~450 nm from organically passivated nanocrystals. This defect emission originates from the localized surface states in the band gap, which presumably are formed by the lack of bonding to surface S ions. In contrast, no defect-related emission is observed from inorganically passivated nanocrystals, indicating the successful complete passivation of CdS:Mn core surface by the ZnS shell layer. Besides, the bandwidth of Mn transition is different for organically versus inorganically passivated nanocrystals, showing much broader in *n*-dodecanethiol-passivated CdS:Mn nanocrystals. It was reported[88] that the electron-phonon (exciton-

phonon) interaction (coupling) plays an important role in the bandwidth of $Mn^{2+}$ emission in ZnS, with a larger interaction causing a broader emission bandwidth. For nanocrystals,

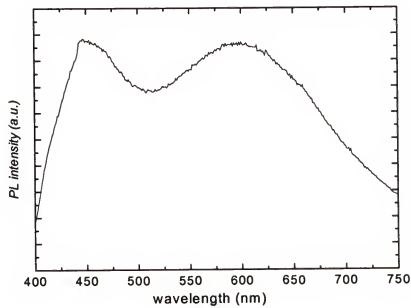


Figure 4-11. PL emission spectra of *n*-dodecanethiol-passivated CdS:Mn nanocrystals. The 325 nm HeCd laser excitation was used.

the electron-phonon coupling strength is determined by the quantum confinement and the surface characteristics,[110,111] which are also dependent on the size of nanocrystal and the type of passivation. Based on the current data, the coupling strength for *n*-dodecanethiol capped CdS:Mn nanocrystals is larger than that for ZnS capped cores due to the trapping of electrons and holes at unpassivated surface states. This leads to the broader bandwidth of the emission peak.

The quantum yields of CdS:Mn nanocrystals with either a *n*-dodecanethiol or ZnS capping layer were measured in chloroform solutions and found to be 3.7 and 18 %, respectively. Note that for quantum yield measurement, CdS:Mn/ZnS core/shell nanocrystals were capped with *n*-dodecanethiol in order to be soluble in chloroform. The

value of 3.7 % for organically capped CdS:Mn is reasonable since it is close to the quantum yields reported from organically passivated ZnS:Mn nanocrystals (1-4 %).[51,112] The enhanced quantum yield of *n*-dodecanethiol-capped CdS:Mn/ZnS nanocrystals is a direct result of more effective surface passivation, by which nonradiative recombination paths are reduced significantly. A visual comparison of organically and inorganically passivated nanocrystals is shown in Figure 4-12. Both samples are standing on a handheld-UV lamp providing 366 nm multiband irradiation, and it is obvious that the ZnS-passivated nanocrystals are much brighter.

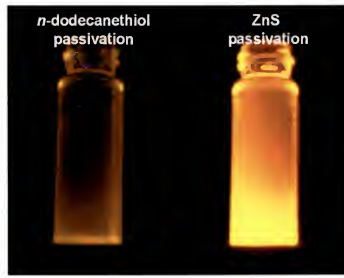


Figure 4-12. Comparison of PL brightness from *n*-dodecanethiol- and ZnS-passivated CdS:Mn nanocrystals under 366 nm UV irradiation.

**4.3.4 UV Irradiation and Photooxidation**

In Figure 4-13, the dependences of PL emission intensity are observed as a function of UV irradiation time. The 400 nm irradiation wavelength for excitation, which is monochromatized from 300 W Xe lamp source, was estimated to have a power density of 655 $\mu W/cm^2$, which corresponds to approximately $1.3\times10^{15}$ photons/s·cm$^2$. Organically

passivated CdS:Mn nanocrystals exhibit a significant reduction (~45 % after 3 hr) of the PL emission intensity upon UV exposure (Figure 4-13 (a)). The reduced PL emission intensity of *n*-dodecanethiol-passivated CdS:Mn nanocrystals presumably results from the fact that the bonding between the Cd (from nanocrystal) and S ions (from organic

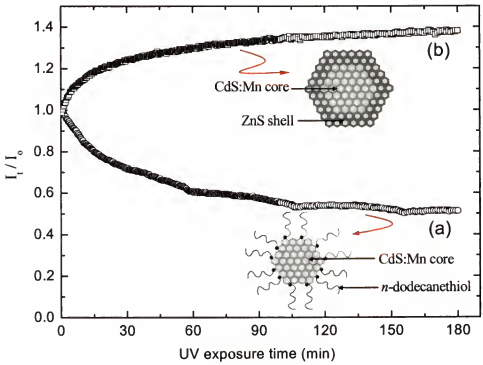


Figure 4-13. Variations of PL emission intensity of (a) *n*-dodecanethiol- and (b) ZnS-passivated CdS:Mn nanocrystals versus time exposed to 400 nm UV light. The monitored wavelengths are 580 nm and 585 nm for *n*-dodecanethiol- and ZnS-passivated CdS:Mn nanocrystals, respectively.

passivating species) at the surface is deteriorated by UV exposure. Accordingly, the density of nonradiative relaxation paths increases at the surface, resulting in a decreased PL emission intensity.[96,113] On the other hand, ZnS-passivated CdS:Mn nanocrystals (sample 1) exhibits a rapid and steady increase, followed by saturation with UV irradiation time up to 180 min (Figure 4-13 (b)). However, the sample 2 exhibits a similar

rapid and steady increase during initial UV irradiation, followed by steady decrease during further irradiation up to 90 min, as shown in Figure 4-14. Since the primary difference between sample 1 and 2 is the ratio $W_2$ which affects the growth of the ZnS shell, the different behavior should be related to the thickness and/or continuity of the ZnS passivation layer. Presumably, the ZnS layer on sample 1 is more passivating. As

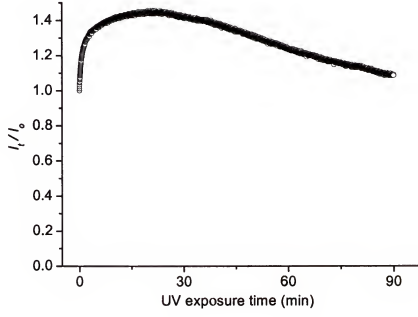


Figure 4-14. Variations of PL emission intensity of sample 2 versus time exposed to 400 nm UV light. The monitored wavelength is 585 nm.

mentioned in Experimental Section, the transparent, stable micellar solution is difficult to obtain with W≥20. This indicates that the micellar solution with an appropriate W ratio plays a critical role in synthesizing photostable nanocrystals with more robust shell layer. However, due to the limitations of structural characterizations (TEM, XPS) on such small nanocrystals, further details are not currently available.

The change in emission intensity from sample 1 during 350 nm UV irradiation (estimated power density of 513 $\mu W/cm^2$) is shown in Figure 4-15. In this case, the

sample was UV-irradiated for 90 min, irradiation was stopped for 2 hr, followed by irradiation for another 2 hr. The rapid increase of emission intensity observed during the

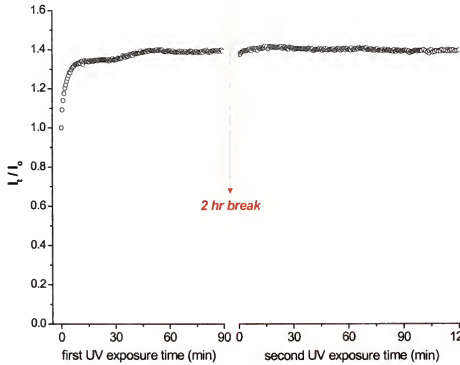


Figure 4-15. Variations of PL emission intensity of sample 1 versus time exposed to 350 nm UV light. The monitored wavelength is 585 nm. The first 90 min UV irradiation is followed by 2 hr stopping of irradiation, and the second 2 hr UV re-irradiation.

first irradiation was not observed during the second irradiation period. Instead, the PL intensity after the first 90 min period is equal to the initial and constant intensity at the start of and throughout the second 2 hr irradiation period. These data suggest that the UV irradiation makes the core/shell nanocrystals photostable.

The increased and stable PL emission intensity resulting from UV irradiation suggests that photochemical and/or photophysical processes are stimulated by this irradiation, and that these processes are irreversible. XPS high resolution scans of the S

2p peaks from CdS:Mn/ZnS nanocrystals irradiated in air with 366 nm UV for different times are shown in Figure 4-16 (a). UV irradiation causes the appearance of a S peak at ~173.8 eV, in addition to the original peak at ~166.5 eV, whose intensity increases with increasing exposure time. The original peak at ~166.5 eV originates from S bound in the CdS core and ZnS shell. However, the S peak at ~173.8 eV is attributed to S bound in $ZnSO_4$, indicating that photooxidation stimulates its formation on the ZnS shell due to oxygen in the air. The formation of $ZnSO_4$ was evident from a second S 2s peak at

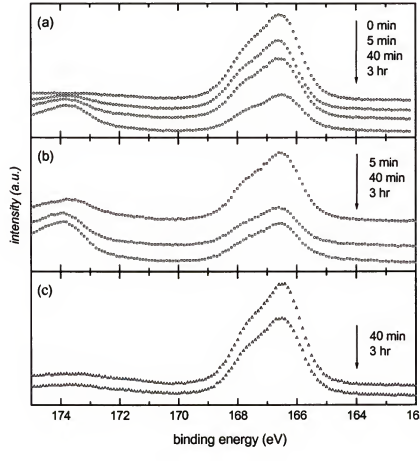


Figure 4-16. XPS scans for S 2p of CdS:Mn/ZnS nanocrystals UV-irradiated for different times, i.e., (a) 366 nm UV in air, (b) 254 nm UV in air, and (c) 366 nm UV in Ar.

~237.6 eV in addition to the original peak at ~231 eV (due to sulfide bonding) as shown in Figure 4-17. Although S 2s peak from $ZnSO_4$ appeared in the sample irradiated in air with 366 nm UV for 3 hr, this peak was not observed from the sample irradiated in Ar under the same conditions. To investigate the effect of wavelength, samples were irradiated with 254 nm rather than 366 nm, and the S 2p peaks are shown in Figure 4-16 (b). The S 2p peak from $ZnSO_4$ exhibited an increased intensity (as compared to 366 nm UV irradiation) for the same exposure times, suggesting that the photooxidation is faster for higher UV energy. To demonstrate that oxygen was important, the S 2p peaks from CdS:Mn/ZnS nanocrystals irradiated with 366 nm UV irradiation in Ar are shown in Figure 4-16 (c). A strong sulfide peak is detected, while the high binding energy peak from sulfate is very weak compared to similar conditions in air, indicating that oxygen isnecessary to form $ZnSO_4$. The appearance of a weak $ZnSO_4$ peak at ~173.8 eV is probably due to residual oxygen which adsorbed on the sample prior to UV irradiation. To evaluate the role of UV irradiation, samples stored in laboratory air for 6 months were measured with XPS and no evidence for $ZnSO_4$ was found. This suggests that UV radiation is necessary for formation of the sulfate. Consistent with formation of $ZnSO_4$, the O/Cd atomic ratios calculated from XPS data increased with longer UV exposure times and shorter UV irradiation wavelengths in air.

While the data are not sufficient to detail the reaction leading to $ZnSO_4$, it is reasonable to speculate that oxygen molecules are physisorbed onto the nanocrystal surface and subsequently photo-dissociated by UV irradiation to form a reactive atomic species, such as excited atomic oxygen ($O^*$), which leads rapidly to the formation of

$ZnSO_4$. The possibility of the formation of $Zn(OH)_2$ phase in the presence of water molecules was also considered, but the rate of photodissociation depends directly on the

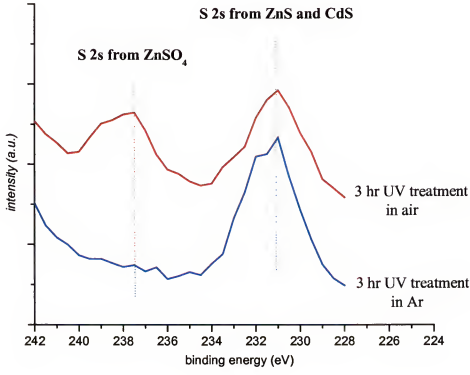


Figure 4-17. XPS scans for S 2s of nanocrystals irradiated in air and Ar under 366 nm UV for 3 hr.

absorption cross-section ($\sigma$). For radiation between 250 and 400 nm, the absorption cross-section of water is negligible compared to that of molecular oxygen,[114] indicating the low probability of $Zn(OH)_2$ formation. In principle, the presence of $Zn(OH)_2$ can be determined by XPS high resolution scans of the Zn 2p and O 1s peaks. However, since the binding energies of the Zn 2p peak in ZnS, $ZnSO_4$ and $Zn(OH)_2$, and those of the O 1s in $ZnSO_4$ and $Zn(OH)_2$ are very close each other (less than 1 eV in difference of binding energy), it was difficult to distinguish these phases by XPS. While there is clear

evidence for the formation of $ZnSO_4$, there is not clear evidence for or against formation of $Zn(OH)_2$ on the surfaces.

Several mechanisms have been proposed to explain an increase of quantum yield in luminescent nanocrystals,[52,90,99] but the XPS data from this study suggest that the enhanced PL emission can be attributed to the photochemical reaction (photooxidation) as proposed by Bol et al.[52] The stable photooxidation product, $ZnSO_4$, presumably acts as a better passivating barrier than ZnS or a 'native oxide' present on the ZnS barrier. An improved surface barrier could further reduce the probability of carriers recombining nonradiatively at surface states. In contrast, Manna et al.[99] suggested that UV light induced a structural rearrangement ("photoannealing") at the interface between CdSe nanorod core and graded CdS/ZnS shell. They suggested that a certain density of defects is likely at the core/shell interface (which are primarily caused by strain due to lattice mismatch), and that these interfacial strain-related defect states could be annealed out via a UV-induced photochemically activated process. However, enhanced luminescence by UV irradiation occurs in both CdS:Mn/ZnS core/shell and unpassivated CdS:Mn nanocrystals, and photoannealing should not occur for unpassivated CdS:Mn nanocrystals. In another study, Katari et al.[26] investigated aging (degradation) upon exposure of tri-*n*-octylphosphine oxide (TOPO)-capped CdSe nanocrystals to air without UV irradiation. They proposed that adsorbed oxygen attacked the chalcogen back bonds of the CdSe semiconductor, followed by the formation of volatile $SeO_2$ that evaporated from the nanocrystal surface ($CdSe + O_2 \rightarrow Cd + SeO_2\uparrow$). Further, it was speculated that the cycle of physisorption/chemisorption on the remaining or newly exposed Se is repeated over time, which would cause the nanocrystal surface to be depleted of Se. An

increase of the atomic ratio of Cd/Se with increased oxidation times was cited to support this mechanism. In the present case, it seems likely that $SO_2$ would not form and volatilize, unlike the case of $SeO_2$ in CdSe nanocrystals. This fact is supported by the fact that the Zn/S ratios for the samples irradiated under different UV exposure times (0, 5, 40 min, and 3 hr) were constant, consistent with non-volatile $ZnSO_4$. Note that both S 2p peaks in Figure 4-16 were used in the quantification of the Zn to S ratio.

The variation with 350 nm UV irradiation time of the PL emission intensity from *n*-dodecanethiol-capped CdS:Mn/ZnS nanocrystals is shown in Figure 4-18. A 60 % increased brightness was observed for an exposure of 3 hr, i.e., slightly greater than the increase reported above (40 %) for a 3 hr exposure of CdS:Mn/ZnS nanocrystals (no *n*-dodecanethiol capping) to 400 nm UV. While the quantum yield of *n*-dodecanethiol-

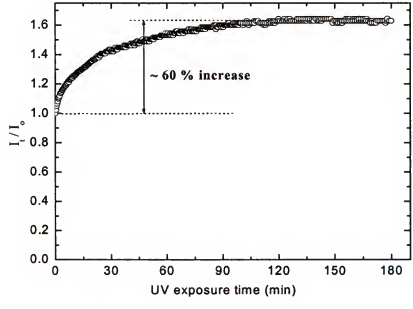


Figure 4-18. Variation of PL emission intensity of *n*-dodecanethiol-capped CdS:Mn/ZnS nanocrystals versus time exposed to 350 nm UV light. The monitored wavelength is 585 nm.

capped CdS:Mn/ZnS nanocrystals was not measured after the PL intensity was increased by UV irradiation for 3 hr, it may be estimated by multiplying the quantum yield without UV enhancement (18 %) by the enhanced brightness (60 %). Using this procedure, a final quantum yield of >28 % would be expected.

### 4.3.5 Luminescence Decay Kinetics

The decay of intensity versus time for 600 nm emission of CdS:Mn/ZnS nanocrystals is shown in Figure 4-19. Figure 4-19 shows a two exponential decay behavior with a fast initial ($\tau \approx 8$ ns) and a slower ($\tau \approx 170$ ns) decay component. Due to the minimum time resolution of the current experimental apparatus, the accuracy of the fast decay time constant is questionable. This short decay time constant of CdS:Mn/ZnS

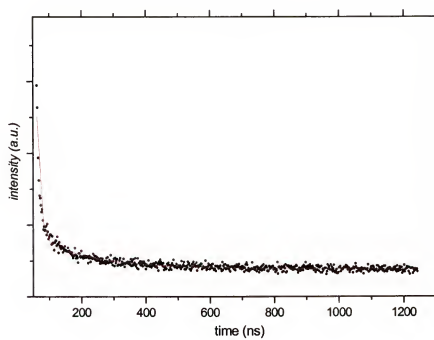


Figure 4-19. Decay curve recorded at an emission wavelength of 600 nm from CdS:Mn/ZnS nanocrystals. The sample was excited at wavelength of 370 nm.

nanocrystals (Figure 4-19) is similar to the report from Bhargava et al.,[9] who observed a dramatic shortening of the Mn emission lifetime from 1.8 ms to 20 ns in Mn-doped ZnS nanocrystals. However, noting that in CdS:Mn/ZnS nanocrystals the weak defect emission occurs over a broad range of wavelengths overlapping the Mn emission as shown in Figure 4-10, the short decay time constant of ~170 ns for CdS:Mn/ZnS nanocrystals presumably results from defect emission. Therefore, the lifetime for decay of the 600 nm emission is dominated by the lifetime of the defect emission.

To obtain the luminescent decay lifetime of Mn emission in CdS:Mn/ZnS core/shell nanocrystals, time-resolved emission spectra were collected and shown in

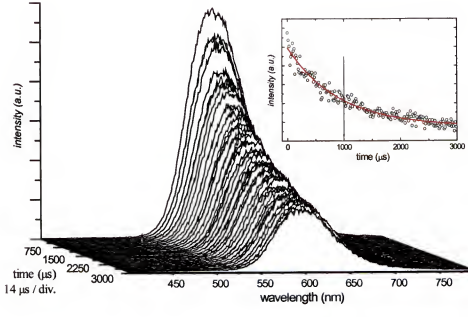


Figure 4-20. Time-resolved spectra of Mn emission of CdS:Mn/ZnS nanocrystals. The fixed gate width of 10 μs was applied and the gate delay was scanned from 14 μs to 3 ms in 14 μs increments. The inset in Figure represents a decay curve obtained by plotting respective intensity at 600 nm with time. The 355 nm (third harmonic) of YAG laser was used as an excitation source.

Figure 4-20. For these time-resolved emission spectra, the gate width of 10 μs was fixed and the gate delay was scanned from 14 μs to 3 ms in 14 μs increments. Inset in Figure 4-20 is the decay curve of the Mn emission intensity at 600 nm versus time. The decay lifetime is ~1 ms at room temperature, comparable to the reports of 0.65 ms[115] in bulk CdS:Mn and 1 ms (at 4 K)[100] in CdS:Mn nanocrystals.

Selected time-resolved emission spectra of *n*-dodecanethiol-passivated CdS:Mn nanocrystals with gate delays of 10 and 1000 ns, and fixed gate width of 10 ns are shown in Figure 4-21 (a) and (b), respectively. The normal steady-state emission spectrum is

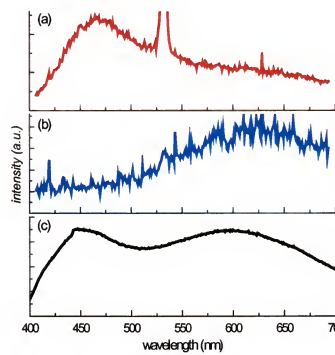


Figure 4-21. Time-resolved emission spectra (a,b) and steady-state emission spectrum (c) of *n*-dodecanethiol-passivated CdS:Mn nanocrystals. In (a) and (b), the fixed gate width of 10 ns and different gate delays of 10 and 1000 ns were applied, respectively. The 355 nm of YAG laser and 325 nm of HeCd laser were used as an excitation source in time-resolved and steady-state emission spectrum, respectively. Note that surface state-related defect emission in (a) is present in (c).

shown in Figure 4-21 (c). The sharp peak at 532 nm in Figure 4-21 (a) is the second harmonic of the YAG laser excitation source (266 nm). The broad emission spectrum recorded with a gate delay of 10 ns after the laser excitation pulse (Figure 4-21 (a)) results mainly from surface-related defect emission with a maximum at ~470 nm. However, in the spectrum recorded with gate delay of 1000 ns and the same gate width, Mn emission near ~620 nm dominates and emission from surface defects is no longer detected (Figure 4-21 (b)), suggesting that the emission lifetime from surface defect is very short (<1 μsec). The steady-state emission spectrum in Figure 4-21 (c) shows appearance of both emissions. These results are similar to those reported by Bol et al.[50] in Mn-doped ZnS nanocrystals. They observed only ZnS-related defect emission at 420 nm with no gate delay, only Mn emission at 590 nm with a gate delay of 0.5 ms in time-resolved emission spectra, and both ZnS defect and Mn emission in steady-state emission spectrum for organically capped ZnS:Mn nanocrystals. This is consistent with very incomplete passivation of the surface states by organic molecules, resulting in defect emission in steady-state as well as time-resolved spectrum.

Another selected time-resolved emission spectra with the same conditions and steady-state emission spectrum of ZnS-passivated CdS:Mn core/shell nanocrystals are shown in Figure 4-22 (a, b) and (c), respectively. As in organically passivated CdS:Mn nanocrystals, time-resolved emission spectra of inorganically passivated nanocrystals exhibit the same trends, i.e., the domination of defect emission with a gate delay of 10 ns and of Mn emission with a gate delay of 1000 ns. Note that the emission intensity at ~460 nm is absent in the steady-state emission spectrum shown in Figure 4-22 (c). The defect emission in Figure 4-22 (a) is attributed to a small concentration of unpassivated surface

defect states in the core/shell nanocrystals. However, the concentration of these surface states is too low to contribute to the steady-state emission spectrum. This is contrast to the observation of surface defect emission in both time-resolved and steady-state emission spectra from *n*-dodecanethiol-passivated CdS:Mn nanocrystals (Figure 4-21 (a), (c)).

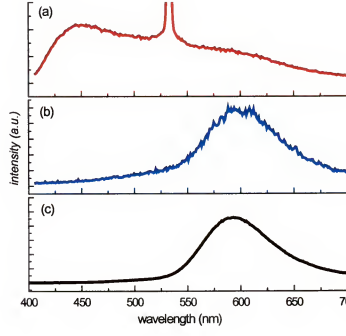


Figure 4-22. Time-resolved emission spectra (a,b) and steady-state emission spectrum (c) of ZnS-passivated CdS:Mn nanocrystals. In (a) and (b), the fixed gate width of 10 ns and different gate delays of 10 and 1000 ns were applied, respectively. The 355 nm of YAG laser and 325 nm of HeCd laser were used as an excitation source in time-resolved and steady-state emission spectrum, respectively. Note that surface state-related defect emission in (a) is absent in (c).

### 4.4 Conclusions

Synthesis of ZnS-passivated CdS:Mn core/shell nanocrystals via a reverse micelle route has been reported. Mn-doped CdS core nanocrystals were produced ranging from 1.5 to 2.3 nm in diameter with epitaxial ZnS shell. For extremely small CdS nanocrystals

(e.g., ~1.5 nm in diameter), doping with Mn apparently had a low probability resulting in lack of luminescence. Effective passivation of the CdS:Mn core surface by a ZnS shell was evident from the absence of a surface-related defect emission and a high quantum efficiency (18 %), compared to *n*-dodecanethiol-passivated CdS:Mn nanocrystals (surface defect luminescence observed and a quantum yield of only 3.7 %). Although *n*-dodecanethiol-passivated CdS:Mn nanocrystals suffered from the reduction of emission intensity during UV irradiation, ZnS-passivated core/shell nanocrystals exhibited the enhanced emission intensity during initial UV irradiation and saturated, stable emission during further UV irradiation. XPS data supported that CdS:Mn/ZnS nanocrystals experience the photooxidation during UV irradiation in air atmosphere. The surface sulfate ($ZnSO_4$), formed as a result of photooxidation, serves as a passivating layer and is responsible for the enhanced PL emission. Also it was concluded that the $ZnSO_4$ is stable and the photooxidation process is irreversible, resulting in photostability. An even higher quantum yield (>28 %) was estimated from 3 hr UV (350 nm) irradiated core/shell nanocrystals. The luminescence decay lifetimes from CdS:Mn/ZnS nanocrystals were shown to be related to the slow decay from Mn luminescent centers and to the fast decay from defect centers. Surface defects exhibited a fast decay (<1 μs), while the decay time constant from Mn emission was much slower at ~1 ms. Time-resolved and steady-state emission spectra from ZnS-passivated CdS:Mn nanocrystals suggest that only a low density of surface states is present after ZnS passivation.

# CHAPTER 5
# ELECTROLUMINESCENCE FROM HYBRID CONJUGATED POLYMERS-CdS:Mn/ZnS CORE/SHELL NANOCRYSTALS DEVICES

## 5.1 Introduction

Recently, electroluminescent (EL) devices using undoped or doped semiconductor nanocrystals have been investigated.[24,66,67,82,85-87,106,116,117] Most of the nanocrystal-based EL devices consist of a hybrid organic/inorganic structure, where either an organic conjugated polymer and inorganic nanocrystal component exist as a separate layer,[24,66,82,85,106,116] or nanocrystals are embedded in a conjugated polymer matrix.[67,117] Like organic light emitting diodes (OLEDs), efficient charge injection and transport are important in hybrid nanocrystal-based EL devices. The electrons and holes injected from respective electrodes combine inside semiconductor nanocrystal and/or conjugated polymer layers, with characteristic lights being emitted as a result of the recombination of these carriers. The electron and hole current flows across EL device are mainly determined by the energy levels of individual component of the EL device. The location of recombination and device efficiency are controlled by the mismatch of those energy levels. In general, improved device efficiency can be accomplished by adding electron transport layers (ETL) and/or hole transport layers (HTL).[91,92] Colvin et al.[24] demonstrated that while a double layer structure having separate poly(*p*-phenylene vinylene) (PPV) (as a hole transport layer) and CdSe nanocrystal layer showed reasonable EL performance, a device with only a CdSe nanocrystal layer did not exhibit detectable EL emission. Also Yang et al.[106] reported that a poly(3,4-

ethylenedioxythiophene)/poly(styrenesulfonate) (PEDOT-PSS) layer led to enhanced current flow through a ZnS:Mn nanocrystalline device because of a lower energy barrier for hole injection from the ITO electrode, as well as enhancement of the hole mobility in PEDOT-PSS.

Organically passivated nanocrystals still have a relatively large number of unpassivated surface sites.[11] These unpassivated surface sites act as nonradiative recombination and photodegradable sites, and thus suppress the efficient luminescence and promote photodegradation of the devices.[23,27] Therefore, control of nanocrystal surface has been a critical issue to obtain highly luminescent nanocrystals and enhanced photostability. Inorganically passivated nanocrystals (or core/shell structure) such as CdSe/CdS,[27] CdSe/ZnS,[23] and ZnSe/ZnS[38] have been reported to be an improvement over those passivated by organic surface layers. Using inorganic materials with a wider band gap, surface-related defect states could be effectively passivated, leading to enhanced photostability as well as improved quantum efficiency.[23,27,38] Schlamp et al.[66] reported an EL device based on CdS-passivated CdSe (CdSe/CdS) nanocrystalline and PPV layers. Simultaneous EL emissions from both the PPV and CdSe/CdS nanocrystal layers in the ITO//PPV//CdSe/CdS//Mg-Ag device structure were observed, indicating that electron-hole recombination occurs in both layers.

In this study, ZnS-passivated CdS:Mn nanocrystals are synthesized for a yellow emitting nanocrystal phosphor. EL devices having a multilayer structure were constructed using conjugated polymers (poly(vinylcarbazole) (PVK) and PPV), and ZnS-passivated CdS:Mn nanocrystals. These nanocrystal-based EL devices exhibit a single EL emission from either the conjugated polymer or CdS:Mn/ZnS nanocrystal layer, rather than

simultaneous EL emission from both layers. Based on the energy level diagrams of the EL devices, the different roles of the conjugated polymer and the nanocrystal layers for hole transport, electron transport, and recombination for emission are proposed.

## 5.2 Experimental Section

### 5.2.1 Synthesis of CdS:Mn/ZnS Core/Shell Nanocrystals

ZnS-passivated CdS:Mn nanocrystals were prepared via a reverse micelle method. In this method, $Cd(CH_3COO)_2 \cdot 2H_2O$, $Mn(CH_3COO)_2$, $Na_2S$, and $Zn(CH_3COO)_2$ were used for preparation of $(Cd^{2+} + Mn^{2+})$-, $S^{2-}$-, and $Zn^{2+}$-containing standard aqueous solutions. Each aqueous solution was stirred with dioctyl sulfosuccinate, sodium salt (AOT)/heptane solution, forming the micellar solution. Mn-doped CdS core nanocrystals were formed by mixing $(Cd^{2+} + Mn^{2+})$- and $S^{2-}$-containing micellar solutions rapidly for 10 to 15 min. For growth of a ZnS shell layer, $Zn^{2+}$-containing micellar solution is added at a very slow rate (1.5~2 ml/min) into the CdS:Mn core nanocrystal micellar solution (while maintaining a surplus of $S^{2-}$ ions to support ZnS shell growth). The homogeneous nucleation and growth of any pure ZnS crystallites were suppressed by the very slow addition of the $Zn^{2+}$ micellar solution. In this reverse micelle route, the concentrations of $Cd^{2+}$ and $Zn^{2+}$ ions in water are 0.1 and 0.065 M, respectively. Also the concentrations of water and AOT in heptane are 1 and 0.1 M, respectively, and the ratio of solution concentration of ZnS to CdS is four. The molar ratios of water-to-surfactant (*W*) are 10 for formation of CdS:Mn core nanocrystals and 20 for the ZnS shell layer. The Mn solution concentration in CdS is 2 mol %. After addition of the $Zn^{2+}$ micellar solution, a small amount of methanol was added to precipitate nanocrystals, which were washed by centrifugation (9000 rpm, 8 min.) more than 3 times with methanol and finally dispersed in methanol.

### 5.2.2 Fabrication of Hybrid Electroluminescence Devices

Two different hybrid EL device structures are shown in Figure 5-1. The hybrid EL device consisting of ITO//PEDOT-PSS//PVK//CdS:Mn/ZnS//Al was constructed as follows. The 30 nm thick PEDOT-PSS layer was spin-deposited onto the cleaned ITO-coated glass substrate. The 120 nm thick PVK layer was spin-deposited on the PEDOT-PSS layer, followed by the deposition of methanol-dispersed CdS:Mn/ZnS nanocrystals.

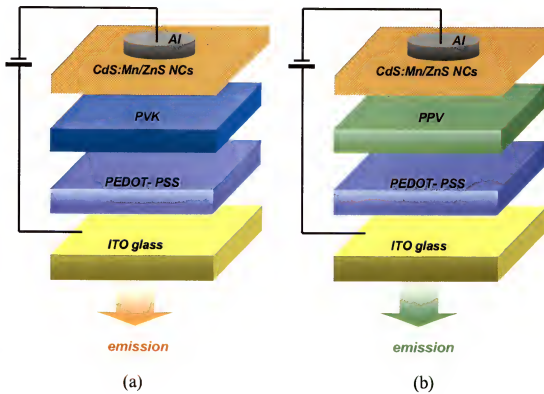


Figure 5-1. Hybrid EL device structures having (a) PVK and (b) PPV conjugated polymer. The CdS:Mn/ZnS nanocrystal layer was dried using a vacuum oven at 60 °C and resulted in a layer 80 nm thick. The 300 nm thick Al contact, 3 mm in diameter, was vacuum-evaporated onto the nanocrystal layer to complete the device. To operate the device, positive and negative voltages were applied to the ITO and Al electrodes, respectively.

The second hybrid EL structure, where PPV conjugated polymer was used instead of PVK, had a structure of ITO//PEDOT-PSS//PPV//CdS:Mn/ZnS//Al. The 20 nm PPV layer was formed by spin-depositing water-diluted poly(xylylene tetra-hydrothiophenium chloride) (precursor PPV) onto the PEDOT-PSS-deposited ITO glass substrate, and then thermally converting the precursor film into a PPV film in a vacuum oven at 160 °C for 12 h. The same procedures as above were followed to complete the EL device. In addition, an EL device without a CdS:Mn/ZnS nanocrystal layer, ITO//PEDOT-PSS//PPV//Al, was constructed for comparison.

### 5.2.3 Characterization

A JEOL 2010F transmission electron microscope (TEM) operated at 200 kV was used for imaging and direct determination of crystal size. For TEM samples, the dilute solution of nanocrystals in methanol was dropped onto a carbon-coated copper grid, dried and placed in the microscope. The film thickness was measured with a Tencor P-10 profilometer. Photoluminescence (PL) excitation and emission spectra were collected at room temperature using a monochromatized Xe light source (300 W). The EL brightness was characterized as a function of voltage across the device. EL emission was collected by a fiber optic and dispersed onto a CCD Si detector (Ocean Optics Spectrometer). The voltage was supplied by a dc power supply, and a Keithley 238 ammeter was used to measure the current.

## 5.3 Results and Discussion

### 5.3.1 Size Information on Core/Shell Nanocrystals

Transmission electron microscope (TEM) images of CdS:Mn/ZnS nanocrystals are shown in Figure 5-2. The average size of core/shell nanocrystals was observed to be 3.1 nm. The Figure 5-2 (b) shows the lattice fringes of CdS:Mn/ZnS nanocrystals clearly,

however, the image contrast between CdS core and ZnS shell is not distinguishable. The nanocrystal size was also approximated using X-ray diffraction (XRD) data and the Debye-Scherrer equation to be 2.3 nm, indicating the ZnS shell thickness of 0.4 nm. The size calculated from the XRD reflects only the CdS:Mn core, since Peng et al.[27] demonstrated that the shell layer does not affect the XRD peak width from the core in a CdSe/CdS core/shell structure.

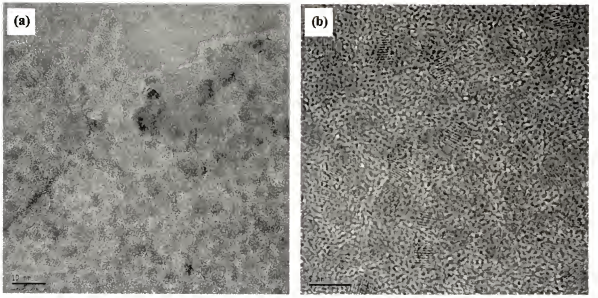


Figure 5-2. Transmission electron microscope (TEM) images with (a) low and (b) high magnification of CdS:Mn/ZnS nanocrystals, showing a mean particle size of 3.1 nm. The length bars at lower left corner in Figure 5-2 (a) and (b) indicate 10 nm and 5 nm, respectively.

### 5.3.2 Electroluminescence and Electrical Properties

Emission spectra as a function of applied voltages from an EL device consisting of ITO//PEDOT-PSS//PVK//CdS:Mn/ZnS//Al are shown in Figure 5-3. The intensity of EL emission increased with increased applied voltage without any change in emission wavelength. In the absence of the PEDOT-PSS layer, no noticeable EL emission was

observed. This is thought to result from the fact that PEDOT-PSS both lowers the energy barrier for hole injection from the ITO electrode and enhances the hole mobility.[106] PL

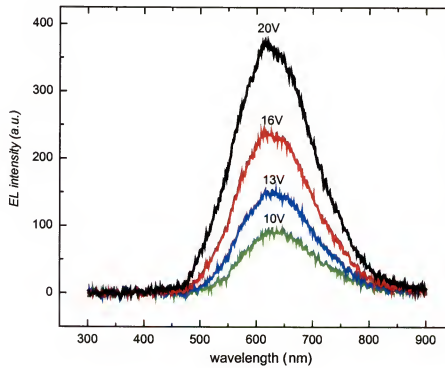


Figure 5-3. EL spectra from an ITO//PEDOT-PSS//PVK//CdS:Mn/ZnS//Al hybrid device as a function of applied voltages.

and EL emission spectra are shown in Figure 5-4 (a) and (b), respectively. The PL emission is from the CdS:Mn/ZnS nanocrystal layer on the glass substrate. The PL emission peak at ~585 nm is due to the Mn $^4T_1$-$^6A_1$ transition, but exhibits a broad tail at longer wavelengths. The EL emission peak is at ~620 nm, i.e., exhibits a relatively large red-shift and broad peak versus the PL peak, again with a long wavelength tail. Assuming PL and EL emission can be described with a Gaussian function, both emission envelopes can be fit by two peaks, as shown in Figure 5-4. The PL peak at 645 nm has been

attributed to emission from internal defects, such as sulfur vacancies.[107,108] It appears reasonable that the emission peaks at 585 and 645 nm observed in PL are red-shifted to

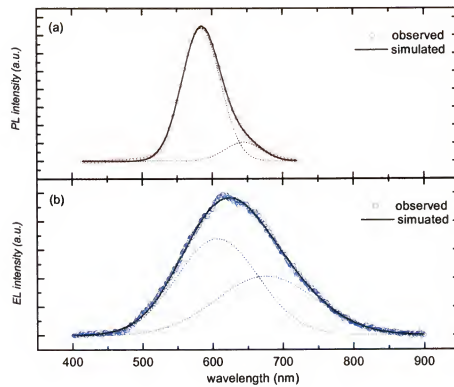


Figure 5-4. Peak fitting of (a) PL emission and (b) EL emission spectra by summation of two Gaussian peaks. The applied voltage for EL and excitation wavelength for PL emission are 16 V and 360 nm, respectively.

605 and 675 nm in EL. The red-shift and broader bandwidth of EL emission relative to PL emission are well-known in nanocrystal-based EL.[66,87,116,117] Notice that the contribution from defect-related emission is more pronounced in EL than in PL. Schlamp et al.[66] proposed that the red-shift of EL emission, observed in CdSe/CdS core/shell nanocrystal-based EL devices, could be attributed to either stronger reabsorption of the short wavelength EL emission by the quantum-shifted nanocrystal layer, or result from

size selection of either charge injection (larger injection barrier exists for smaller nanocrystals) or Föster energy transfer from small to large nanocrystals. While intrinsic semiconducting materials such as nanocrystalline CdSe may exhibit such band-edge (excitonic) transition reflecting quantum shifts of their band gap, impurity-doped semiconductors such CdS:Mn show unique impurity-related transitions. Thus, the reason for red-shift EL emission for the present material cannot be explained by these mechanisms. Rather, the red-shift as well as broader EL emission peaks relative to PL is postulated to be due to local Joule heating from the large current flux and poor thermal conductivity of the emitting layer, as reported previously.[87,117]

Recall that EL emission from PVK is not observed from a ITO//PEDOT-PSS//PVK//CdS:Mn/ZnS//Al device. Most nanocrystal-based EL devices using a conjugated polymer as a charge transport layer show emission from both the nanocrystal and polymer layers, due to electron-hole recombination in both components.[24,66,117] PL emission was collected from the same EL sample and compared with EL data (Figure 5-5). As a reference, PL emission from PVK layer only is also shown in Figure 5-5. Blue and orange PL peaks at ~405 and ~585 nm are observed due to PVK and CdS:Mn/ZnS nanocrystals, respectively.

The current-voltage (I-V) characteristic of a device consisting of ITO//PEDOT-PSS//PVK//CdS:Mn/ZnS//Al is shown in Figure 5-6 (a). EL emission was only observed under a forward bias, i.e., when a positive voltage is applied to the ITO electrode. The log I / log V plot in Figure 5-6 (b) suggests an ohmic-like behavior ($I \propto V$) at low voltages ($< 8$ V), indicating that conductance is limited by the PVK and CdS:Mn/ZnS nanocrystal layers rather than interfaces between them and/or electrode interfaces. At higher

voltages(> 8 V) the data follow the trapped-charge-limited-current (TCLC) model, i.e., $I \propto V^m$ with $m \approx 5$. This suggests that above 8 V, a fraction of carriers injected from the electrodes participates in current flows while the balance are immobilized by traps.[58,60] Several organic light emitting devices have been demonstrated to exhibit an $I \propto V^m$ relation with different values of m, depending on the type of organic materials and the depth of the trap (i.e., the trap energy).[58,118]

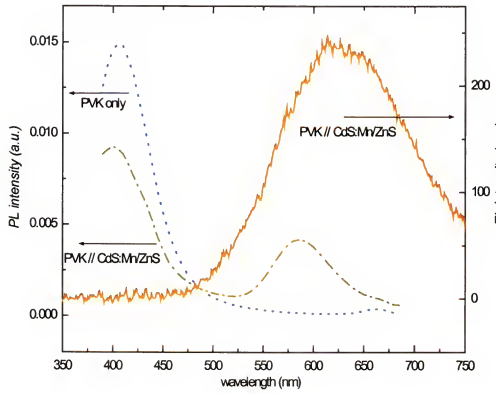


Figure 5-5. Comparison of PL and EL emission spectra obtained from an ITO//PEDOT-PSS//PVK//CdS:Mn/ZnS//Al device. PL emission spectrum of PVK only is shown for comparison. The applied voltage for EL and excitation wavelength for PL emission are 16 V and 360 nm, respectively.

PPV is a conjugated polymer, which is widely used as emitting layer in OLEDs and as a hole transport layer in nanocrystal-based EL devices. Additional multilayer EL

structures consisting of either ITO//PEDOT-PSS//PPV//CdS:Mn/ZnS//Al or ITO//PEDOT-PSS//PPV//Al were fabricated. EL emission spectra as a function of applied voltages from ITO//PEDOT-PSS//PPV//CdS:Mn/ZnS//Al and ITO//PEDOT-

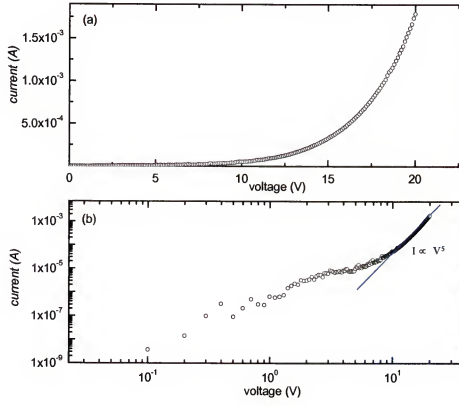


Figure 5-6. Current (I) versus voltage (V) relations from an ITO//PEDOT-PSS//PVK //CdS:Mn/ZnS//Al EL device with respect to (a) I-V and (b) log I-log V curves.

PSS//PPV//Al device are shown in Figure 5-7 (a) and (b), respectively. In terms of EL intensity, the device with the CdS:Mn/ZnS nanocrystal layer was much brighter at the same voltage than the one with only PPV. While a detectable EL emission requires ~5 V in the PPV-only device, the device with the nanocrystal layer exhibits a bright EL emission even at ~2.5 V. At 5 V, the EL emission is sufficiently intense to saturate the

detection. However, the EL emission from the nanocrystal layer devices originates from only the PPV layer, not the CdS:Mn/ZnS layer or both layers (see Figure 5-8). This is completely different from the ITO//PEDOT-PSS//PVK//CdS:Mn/ZnS//Al devices, where EL emission results from the CdS:Mn/ZnS nanocrystal layer. The EL and PL spectra collected from ITO//PEDOT-PSS//PPV//CdS:Mn/ZnS//Al devices, and PL emission from

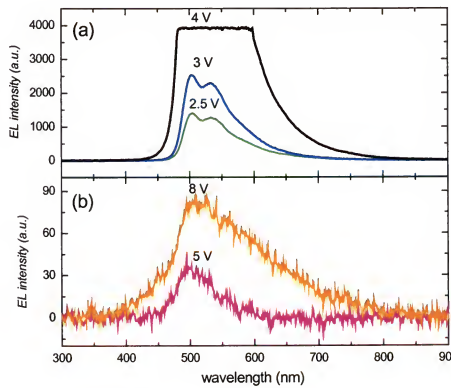


Figure 5-7. Comparison of EL emission spectra as a function of applied voltages from (a) ITO//PEDOT-PSS//PPV//CdS:Mn/ZnS//Al and (b) ITO//PEDOT-PSS//PPV// Al EL devices.

PPV-only devices are shown in Figure 5-8. In PL, green and orange PL peaks at ~500 and ~585 nm are observed from the PPV and CdS:Mn/ZnS nanocrystal layers, respectively. The I-V characteristics of ITO//PEDOT-PSS//PPV//CdS:Mn/ZnS//Al and ITO//PEDOT-PSS//PPV//Al device are shown in Figure 5-9 (a) and (b), respectively, and

the effect of the CdS:Mn/ZnS nanocrystal layer on current flow is dramatic. In the device with the CdS:Mn/ZnS nanocrystal layer, the current increased with voltage in a power law fashion. In device with only PPV, a large current flows up to an applied voltage of ~1.5 V due to the filamentary conduction, but current drops to near zero at higher

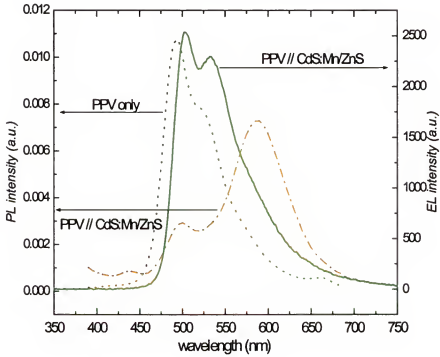


Figure 5-8. Comparison of PL emission and EL emission spectra obtained from ITO//PEDOT-PSS//PPV//CdS:Mn/ZnS//Al device structures. PL emission spectrum of PPV only is shown for comparison. The applied voltage for EL and excitation wavelength for PL emission are 3 V and 360 nm, respectively.

voltages. This filamentary current does not contribute to EL emission and did not appear upon reapplying the voltage. The inset in Figure 5-9 (b) shows that small current flows were observed between 3 and 9 V. This small and irregular current flow did result in weak EL emission from ITO//PEDOT-PSS//PPV//Al device.

### 5.3.3 Proposed Energy Diagrams of Devices

The energy level diagrams of devices consisting of ITO//PEDOT-PSS//PVK// CdS:Mn/ZnS//Al and ITO//PEDOT-PSS//PPV//CdS:Mn/ZnS//Al are shown in Figure 5-10 (a) and (b), respectively. The work functions, band gaps, and electron affinities of ITO, Al, PEDOT-PSS, PVK, and PPV are values reported in the literature. Note that since the ZnS capping layer is so thin (<1 nm), its energy levels are not shown in Figure 5-10. The electron affinity of the CdS in the nanocrystal layer is extrapolated from that (~4.4 eV) of bulk CdS,[5] based on the effective mass approximation (quantum

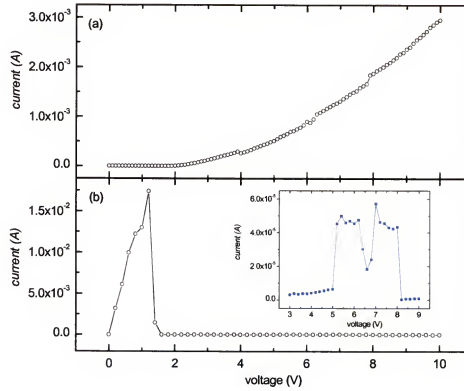


Figure 5-9. Comparison of I-V data from (a) ITO//PEDOT-PSS//PPV//CdS:Mn/ZnS//Al and (b) ITO//PEDOT-PSS//PPV//Al EL devices. The inset in Fig. 7 (b) is the magnified plot between 3 and 9 V.

confinement) theory.[5,6] Due to the lighter effective mass of electrons versus holes in CdS ($m_h/m_e$ ~4),[5,119] the electron affinity of CdS nanocrystal depends mostly on the energy of the conduction band edge. The band gap (~3.1 eV) of CdS core nanocrystal is determined from UV-visible absorption data (not shown here). An EL device with neither a PVK nor a PPV layer (i.e., ITO//PEDOT-PSS//CdS:Mn/ZnS//Al) was tested but no EL emission was observed. As shown by the energy band diagrams (Figure 5-10), this lack of emission may be attributed to a large hole injection barrier at the PEDOT-PPS// CdS:Mn/ZnS interface. The presence of a PVK layer makes hole injection into nanocrystal layer efficient by lowering this energy barrier. In the case of a PPV layer, the ionization potential of PPV is comparable to the work function of PEDOT-PSS and the PPV layer does not lower the energy barrier for hole injection into the nanocrystal layer. While the energy barrier for electron injection at the CdS:Mn/ZnS//Al interface remains constant independent of the polymer layer, the energy barrier (~0.1 eV) for hole injection at the PEDOT-PSS//PPV interface is lower than that (~0.8 eV) at the PEDOT-PSS//PVK interface. This is consistent with the fact that the PPV-based nanocrystal devices have a lower turn-on voltage and higher current flow at the same voltage as compared to the PVK-based devices. As shown in Figures 5-3 and 5-7 (a), orange emission from the CdS:Mn/ZnS nanocrystal layer is dominant from PVK-based hybrid devices, while green emission from the PPV layer is dominant from PPV-based hybrid devices. This clearly implies that the electron-hole recombination occurs in different regions for the two different EL devices. Based on the energy levels shown in Figure 5-9, the offset of the conduction bands at the PVK//CdS:Mn/ZnS heterojunction is larger (1.4 eV) than that of the valence bands (1.0 eV), therefore hole injection into the CdS:Mn/ZnS nanocrystal

layer is favored and recombination of electron and hole in the CdS:Mn/ZnS nanocrystal layer is dominant. In contrast, for a PPV-based nanocrystal device, the PPV// CdS:Mn/ZnS conduction band offset is lower (1.2 eV) than the valence band offset (1.7 eV). These offsets would favor electron injection from CdS:Mn/ZnS nanocrystals into

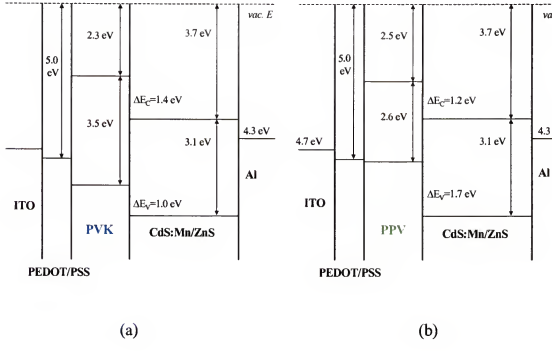


Figure 5-10. Proposed energy level diagrams of (a) an ITO//PEDOT-PSS//PVK// CdS:Mn/ZnS//Al device, and (b) an ITO//PEDOT-PSS//PPV//CdS:Mn/ZnS// Al EL device.

PPV and recombination of electron and hole in the PPV layer. The large differences in EL emission intensity and current flow of PPV-based nanocrystal and PPV-only EL devices were shown in Figures 5-7 and 5-9. Compared to PPV-only devices, PPV-based nanocrystal hybrid EL devices exhibit much greater EL brightness and larger current flows. This is presumably due to the enhanced electron injection from the nanocrystalline layer between PPV and Al. This results from the CdS:Mn/ZnS nanocrystal layer serving

as an electron transport layer with high conductance, and from enhanced electron flow due to lowering of the energy barrier for electron injection.

### 5.4 Conclusions

Nanocrystals with a CdS:Mn/ZnS core/shell structure with a core crystal diameter of 2.3 nm and a shell thickness of 0.4 nm were synthesized via a reverse micelle route. Hybrid electroluminescent devices with a multilayer structure were fabricated using CdS:Mn/ZnS core/shell nanocrystals and conjugated polymers such as PVK and PPV. In PVK-based nanocrystal devices, only orange emission from the CdS:Mn/ZnS nanocrystal layer was observed, with no emission from the PVK. However, only green EL emission was observed from the PPV layer in PPV-based nanocrystal hybrid devices, with no emission from the nanocrystalline layer. EL emission from a single layer of a multilayer structure was concluded to result from radiative electron-hole recombination occurring predominantly in that layer. The current-voltage characteristic of PVK-based nanocrystal hybrid EL devices was discussed, and the trapped-charge-limited-current (TCLC) model was suggested to describe the behavior at voltages > 8 V. PPV-only EL devices showed much smaller current flow and weaker EL emission than PPV-based nanocrystal hybrid EL devices. All of these data were interpreted in terms of energy levels for the PVK, PPV, and quantum shifted CdS:Mn/ZnS structures. When the valence band offset was smaller than the conduction band offset (PVK-based hybrid device), recombination occurred in the nanocrystalline layer. When the conduction band offset was less that the valance band offset (PPV-based hybrid device), recombination occurred in the conjugated polymer.

# CHAPTER 6
# SILICA-OVERCOATED CdS:Mn/ZnS SEMICONDUCTOR QUANTUM DOTS FOR LUMINESCENT BIOMARKERS

## 6.1 Introduction

Semiconductor quantum dots have a tremendous potential as biomarkers in the fields of molecular/cell biology, medical diagnostics and targeted therapeutics. The high-temperature organometallic procedure-derived core/shell structured quantum dots, where surface passivating layers such as CdS and ZnS are epitaxially grown on the CdSe core, have been found to dramatically enhance the quantum yields of CdSe quantum dots from <10 % up to 40–50 %.[23,27,28] In addition, luminescent quantum dots (inorganic fluorophores) have advantages over conventional organic fluorophores, since quantum dots have large absorption bands, narrow spectral emission bands, and are photochemically stable. However, poor solubility of semiconductor quantum dots in water, indicative of incompatibility with biological environments or aqueous assay conditions, has placed limits on their use.

Several strategies have been pursued to water-solubilize quantum dots with inherently hydrophobic surface.[68,70,72,74,75,77] Chan et al.[74] used mercaptoacetic acid as a coupling reagent with ZnS capped CdSe (CdSe/ZnS) quantum dots, where a thiolated group binds to a surface Zn atom, and the polar carboxylic acid group renders the quantum dots soluble in water. However, it is known that this surface modification of quantum dots, based on direct bonding of a coupling agent with a surface atom, does not ensure persistent bonding, indicating that slow desorption of mercaptoacetic acid

molecules occurs from the surface of quantum dots. This leads to poor stability of quantum dots in water. As an alternative method, complete encapsulation of individual quantum dots with silica,[68,72] amphiphilic polymer,[70,75] or micelle-forming hydrophilic polymer-grafted lipids[77] has been approached. Among them, silica coating can improve the solubility of quantum dots and the silica surface can be easily modified by conventional surface chemistry to immobilize biomolecules. Bruchez et al.[68] reported water-soluble, silica-coated CdSe/ZnS core/shell quantum dots, where the outmost silica layer renders the dots hydrophilic and water-soluble. However, the experimental procedure for silica coating was complicated and difficult to reproduce. In addition, to date these efforts have focused only on undoped CdSe- or CdTe-based quantum dots.

We have previously developed photostable, yellow-emitting ZnS-passivated, $Mn^{2+}$-doped CdS (CdS:Mn/ZnS core/shell) quantum dots with high quantum yield of 18–28 % via a reverse micelle method.[98,120] In this report, water-soluble, silica-overcoated CdS:Mn/ZnS quantum dots, synthesized using a simple reverse micelle technique, is described. The silica overcoating was accomplished by the hydrolysis of tetraethyl orthosilicate (TEOS) in the presence of $NH_4OH$, followed by condensation between hydroxyl groups (-OHs).

### 6.2 Synthesis of Water-Soluble Quantum Dots

A typical synthesis of CdS:Mn/ZnS core/shell quantum dots was described in the literature[98,120] and is presented briefly here. After ($Cd^{2+}$ + $Mn^{2+}$)-, $S^{2-}$-, and $Zn^{2+}$-containing aqueous solutions are prepared from $Cd(CH_3COO)_2 \cdot 2H_2O$, $Mn(CH_3COO)_2$, $Na_2S$, and $Zn(CH_3COO)_2$, respectively, each solution is stirred with dioctyl sulfosuccinate, sodium salt (AOT)/heptane stock solution. CdS:Mn/ZnS quantum dots are formed by mixing ($Cd^{2+}$ + $Mn^{2+}$)- and $S^{2-}$-containing micellar solutions for 15 min,

followed by the addition of $Zn^{2+}$-containing micellar solution at a very slow rate of ~1.5 ml/min for ZnS shell growth over the CdS:Mn core surface. A surplus of $S^{2-}$ ions is maintained in the CdS:Mn nanocrystal micellar solution to support further ZnS shell growth. The concentrations of $Cd^{2+}$, $S^{2-}$, and $Zn^{2+}$ in water were 0.1, 0.66, and 0.26 M, respectively (0.048 g of $Cd(CH_3COO)_2 \cdot 2H_2O$, 0.2812 g of $Na_2S$, and 0.264 g of $Zn(CH_3COO)_2$ are used). The Mn solution concentration in CdS is 2 mol %. The molar ratio of water-to-surfactant (W) is 10 for all micellar solutions. After addition of the Zn micellar solution, 3.7 ml of TEOS is injected into CdS:Mn/ZnS micellar solution and mixed for 15 min. The silica polymerization reaction is initiated by adding $NH_4OH$ in the form of micellar solution, which is prepared by mixing 2.2 ml of $NH_4OH$ (30 wt %) with AOT (5.5 g)/heptane (123 ml) stock solution. After polymerization for 48 hr at room temperature, silica-overcoated CdS:Mn/ZnS quantum dots are precipitated by addition of a small amount of methanol. After thorough washing with methanol, silica-overcoated quantum dots are solubilized and stable in a sodium phosphate buffer solution with pH ~7. Silica-overcoated CdS:Mn quantum dots without ZnS shell were prepared with the same W ratio and Mn concentration. Figure 6-1 illustrates the experimental procedures for the synthesis of silica-overcoated CdS:Mn/ZnS and CdS:Mn quantum dots, respectively.

## 6.3 Results and Discussion

### 6.3.1 Water-Soluble Quantum Dots and Formation of Silica Shell

The solubility tests in water (sodium phosphate buffer solution) of bare and silica-overcoated CdS:Mn/ZnS quantum dots are illustrated in Figure 6-2. The bare and silica-overcoated CdS:Mn/ZnS quantum dots dispersed in water initially are shown in Figure 6-2 (a), where better transparency is observed from silica-overcoated quantum dot solution,

as compared to bare quantum dot solution. These quantum dot solutions were monitored after a certain period of time (Figure 6-2 (b)). Whereas bare quantum dots precipitate

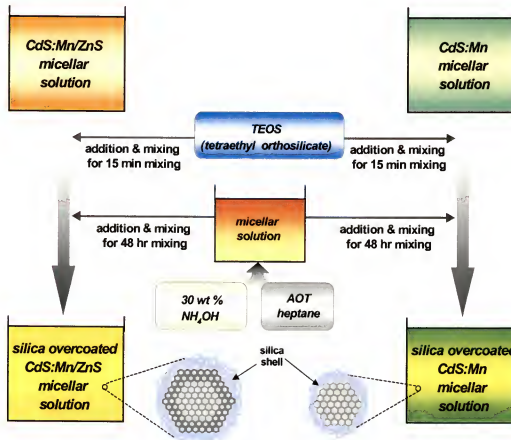
CdS:Mn/ZnS micellar solution
CdS:Mn micellar solution
TEOS (tetraethyl orthosilicate)
addition & mixing for 15 min mixing
addition & mixing for 15 min mixing
addition & mixing for 48 hr mixing
micellar solution
addition & mixing for 48 hr mixing
30 wt % NH4OH
AOT heptane
silica overcoated CdS:Mn/ZnS micellar solution
silica shell
silica overcoated CdS:Mn micellar solution

Figure 6-1. Schematic of experimental procedures of synthesis of silica-overcoated CdS:Mn/ZnS (left) and CdS:Mn (right) quantum dots.

completely 2 hr later, silica-overcoated quantum dots are still water-soluble even after 3 day. Figure 6-2 (c) shows two samples in (b) under 366 nm UV irradiation, demonstrating the opposite situations of complete precipitation versus stable solubility. The fact that silica-overcoated CdS:Mn/ZnS quantum dots are solubilized and stable in sodium phosphate buffer solution indicates that the quantum dots are surrounded by the silica shell. The silica shell renders the quantum dots water-soluble by hydrophilic hydroxyl surface groups, i.e., Si-OH.

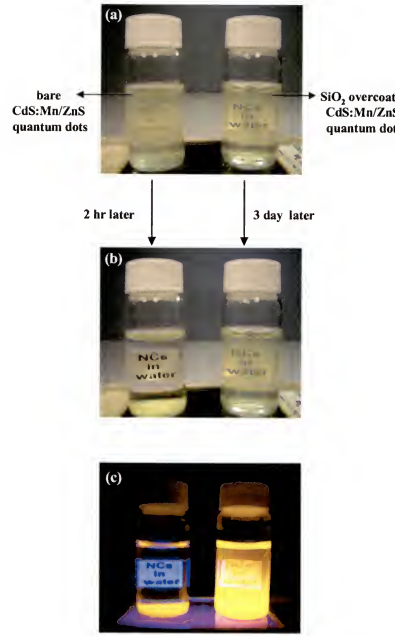


Figure 6-2. Solubility tests of bare and silica-coated CdS:Mn/ZnS quantum dots in water with time.

The FT-IR spectra of bare and silica-overcoated quantum dots are shown in Figure 6-3. The signals at 3400 and 1640 $cm^{-1}$ are attributed to adsorbed water molecules, i.e.,

O-H stretching and H-O-H bending vibrations, respectively. And the peaks at 1400 and 1050 $cm^{-1}$ are presumably attributed to organic groups due to residual AOT or organic

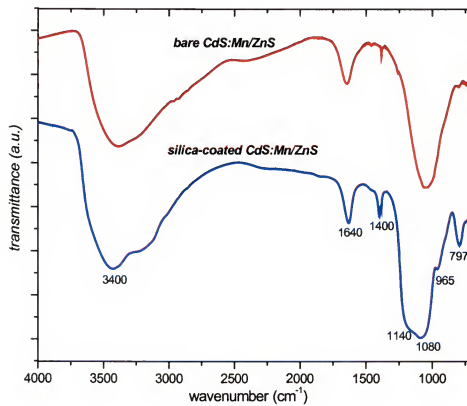


Figure 6-3. FT-IR spectra of bare and silica-coated CdS:Mn/ZnS quantum dots.

solvent. The observation of Si-O-Si and Si-OH bonding by FT-IR spectroscopy is typical of the identification of silica phase. In FT-IR spectrum of silica-overcoated quantum dots, the bands corresponding to Si-O-Si symmetric and asymmetric vibrations are observed at 1140 and 797 $cm^{-1}$, respectively.[121,122] Additionally, the peak at 965 $cm^{-1}$ can be assigned to Si-OH group.[121,123] This FT-IR study indicates that silica phase formed successfully from its precursor (TEOS).

High resolution transmission electron microscopy (HRTEM) images of silica-overcoated quantum dots are shown in Figure 6-4. The silica shell layer is very difficult

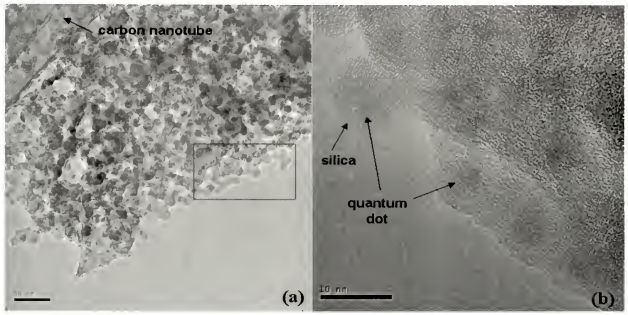


Figure 6-4. Transmission electron microscope images of silica-overcoated CdS:Mn/ZnS quantum dots at (a) low, and (b) high magnification. Figure 6-4 (b) corresponds to a part of the dotted area in (a). The length bars at lower left corner in (a) and (b) indicate 50 and 10 nm, respectively.

to image using a normal (carbon-coated) TEM grid. This is because the silica layer is amorphous and thin, making it difficult to distinguish silica from the amorphous carbon film on the TEM grid. Instead, a lacey TEM grid, which allows high definition imaging without the effects of underlying support material, was used. Silica-coated quantum dots were blended with carbon nanotubes dispersed in methanol solution, leading to rapid precipitation of the mixture (quantum dots plus nanotubes). And then, a drop of this mixture solution was placed on a lacey TEM grid. By this TEM sample preparation, aggregates of silica-coated quantum dots are attached to carbon nanotubes, which are sitting on lacey grid. An aggregated cluster of silica-coated quantum dots attached to a

carbon nanotube is shown in Figure 6-4 (a). The contrast between the light silica shell and the dark CdS:Mn/ZnS quantum dot is apparent. Lattice fringes of ~3.2 nm diameter CdS:Mn/ZnS quantum dots with ~2.5 nm thick silica shell layer can be seen in Figure 6-4 (b), taken from the dotted area of Figure 6-4 (a).

The surface sensitivity (few atom layers) of x-ray photoelectron spectroscopy (XPS) can be used to indicate whether or not the silica covers the outer surface.[27,28,35] XPS (Mg $K_\alpha$ radiation) spectra from bare and silica-overcoated CdS:Mn/ZnS quantum dots are compared in Figure 6-5. It is apparent that the intensities of the photoelectron peaks from Cd, Zn, and S are suppressed on silica-overcoated quantum dots, while the intensity from Si and O is larger, consistent with the presence of a silica surface layer. More quantitative compositional analysis is possible by comparing XPS and energy-dispersive x-ray spectroscopy (EDS) data, since XPS is a surface sensitive method and EDS is a bulk method of quantitative compositional analysis.[98] The atomic ratio of Si/Zn from XPS and EDS are determined by integrating the peak areas and dividing by the sensitivity factors. The Si/Zn ratios from EDS and XPS data were obtained to be 8.4 and 16.7, respectively, suggesting that the silica shell has formed on the CdS:Mn/ZnS quantum dot. Also, note that the ratio of Cd photoelectron and Auger electron peak intensity was used to demonstrate the formation of ZnS shell on CdS:Mn nanocrystals (see 4.3.2). Likewise, the ratio of Zn photoelelctron and Auger electron peak intensity can be used to demonstrate silica-overcoat on the CdS:Mn/ZnS quantum dots. The intensity ratio $I_{silica}/I_{bare}$ can be defined, where $I_{silica}$ and $I_{bare}$ are the intensity ratios of the Zn photoelectron to Auger electron signals, i.e., $I_{Zn(PE)}/I_{Zn(Auger)}$, from silica-coated and bare CdS:Mn/ZnS quantum dots, respectively. The kinetic energies of the Zn 2p and

Auger (LMM) electrons are 232 and 990 eV, respectively. This energy difference leads to significantly different escape lengths due to the silica-overcoat on the quantum dots. Therefore, the low energy Zn 2p electrons will be attenuated more by the silica layer than will the higher energy Zn Auger (LMM) electrons. The observed $I_{silica}/I_{bare}$ value of 0.38 is consistent with the presence of a silica-overcoat on the CdS:Mn/ZnS quantum dots.

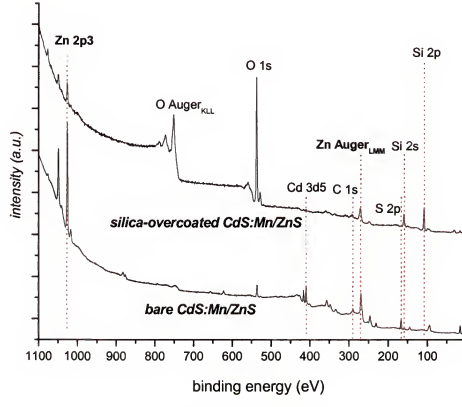


Figure 6-5. XPS survey spectra of (a) bare and (b) silica-overcoated CdS:Mn/ZnS quantum dots.

### 6.3.2 Effects of Silica-Overcoating on PL Emission

Photoluminescence (PL) emission spectra, collected from 325 nm HeCd laser excitation, of unpassivated, silica-overcoated, and ZnS-passivated CdS:Mn quantum dots are compared in Figure 6-6. Negligible PL emission is observed from unpassivated CdS:Mn, due to the predominance of nonradiative relaxation of photoexcited electron-

hole pairs at unpassivated surface sites.[98] Silica-overcoated CdS:Mn quantum dots show higher PL emission as compared to unpassivated dots, but the broad emission can be resolved into two peaks, with a peak at ~470 nm resulting from a surface defect, and the peak at ~620 nm resulting from the $Mn^{2+}$ $^4T_1$-$^6A_1$ transition. In contrast to unpassivated or silica-passivated dots, ZnS-passivated CdS:Mn (CdS:Mn/ZnS core/shell) quantum dots exhibit a very intense and sharp $^4T_1$-$^6A_1$ emission peak at ~600 nm with negligible surface state-related emission, i.e., the ZnS shell is effective in suppressing nonradiative recombination at surface states. Better suppression of surface nonradiative recombination in CdS:Mn/ZnS quantum dots probably results from the fact that the ZnS shell layer is

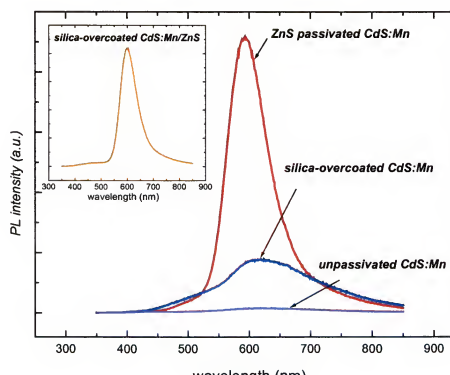


Figure 6-6. PL emission spectra of unpassivated, silica-overcoated, and ZnS-passivated CdS:Mn quantum dots using 325 nm HeCd laser excitation. The inset in Figure 6-6 is PL emission spectrum of silica-overcoated CdS:Mn/ZnS quantum dots.

grown epitaxially on the core surface.[98,120] Even though the coverage of silica shell on the CdS:Mn quantum dots appears complete, the amorphous silica layer would not form epitaxially and results in a less than complete surface passivation. Finally, the PL emission spectrum from silica-overcoated CdS:Mn/ZnS quantum dots is shown in the inset in Figure 6-6, and it is exactly the same as that from bare CdS:Mn/ZnS quantum dots, indicating that silica overcoating does not modify the PL emission properties of CdS:Mn/ZnS quantum dots.

### 6.3.3 Photooxidation of Silica-Overcoated CdS:Mn/ZnS Quantum Dots

The change of 585 nm PL emission intensity of a dried layer of silica-overcoated CdS:Mn/ZnS quantum dots versus time of irradiation by 385 nm UV photons was measured using a monochromatized 300 W Xe light excitation source at room temperature (Figure 6-7). Silica-overcoated CdS:Mn/ZnS quantum dots show an

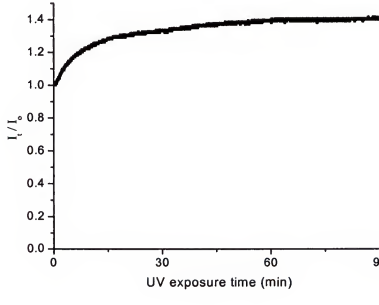


Figure 6-7. Variation of 585 nm PL emission intensity of silica-overcoated CdS:Mn/ZnS quantum dots versus time exposure to 385 nm UV light.

increased PL emission intensity of ~40 % over the first 60 min, and was stable between 60 and 90 min. We previously reported that the PL emission intensity from bare CdS:Mn/ZnS quantum dots increased as a result of UV irradiation.[120] XPS data revealed that UV irradiation in air atmosphere induces irreversible photochemical reaction (photooxidation) of the CdS:Mn/ZnS core/shell quantum dots, producing stable $ZnSO_4$ phase on the ZnS shell surface. This photooxidation product, $ZnSO_4$, serves as an improved passivation layer to further reduce the nonradiative recombination rates. High resolution XPS scans of the S 2p peak from bare and silica-overcoated CdS:Mn/ZnS quantum dots are shown in Figure 6-8. Both samples were UV-exposed in air for 3 hr. On bare CdS:Mn/ZnS quantum dots, two distinct S 2p peaks at ~166.5 eV and ~173.8 eV are

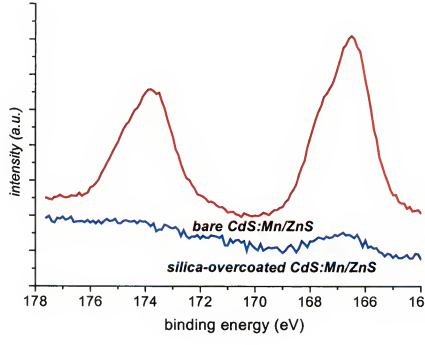


Figure 6-8. XPS spectra of bare and silica-overcoated CdS:Mn/ZnS quantum dots after 366 nm UV irradiated for 3 hr in air. Both samples were UV-treated by using a handheld UV lamp providing 366 nm multiband photons.

due to S atoms in the CdS core/ZnS shell and in $ZnSO_4$, respectively.[124] In silica-overcoated CdS:Mn/ZnS quantum dots, however, the S 2p peaks are difficult to distinguish due to the attenuation of the S signal by the overlying silica shell. However, $ZnSO_4$ is still likely to form as a photooxidation product, because the silica surface layer is amorphous and porous.

### 6.4 Conclusions

Water-soluble CdS:Mn/ZnS quantum dots were successfully synthesized by silica overcoating. The CdS:Mn/ZnS quantum dot and silica layer were found to be ~3.2 nm in diameter and ~2.5 nm in thickness, respectively. XPS analysis confirmed that the CdS:Mn/ZnS quantum dots are overcoated by a silica shell. While the silica surface coating made the quantum dots water-soluble, a silica coating on CdS:Mn dots was not sufficient to passivate the surface for photoluminescence. The silica-overcoated CdS:Mn/ZnS quantum dots were shown to be stable for 90 min exposures to 385 nm UV irradiation in air, suggesting excellent photostability.

# CHAPTER 7
# CONCLUSIONS

## 7.1 Competitive Reaction Chemistry-Based ZnS:Mn Nanocrystals

ZnS:Mn nanocrystals capped with *p*-thiocresol were synthesized from a competitive reaction chemistry which resulted in a particle size of 3 to 4 nm. The photoluminescent (PL) and electrolumnescent (EL) characterizations were studied, and the following conclusions were drawn.

1. A blue shift of 0.37 eV from 342 to 308 nm was observed for band gap absorption as a result of quantum confinement in nanocrystals versus 'bulk' micrometer sized ZnS particles.

2. Radiative recombination from both Mn (~600 nm) and localized surface states (~460 nm) was present in the PL emission spectrum of the nanocrystals, implying that the surface capping agent was not completely effective in passivating ZnS nanocrystal surfaces.

3. Variation of the Mn concentration in the nanocrystals from 0.40 to 2.14 mol % did not affect the position or shape of the of PL emission spectrum.

4. An electroluminescence nanocrystal device, consisting of a multilayer structure of ITO/PEDOT-PSS/PVK/ZnS:Mn/Al, was fabricated. The PEDOT-PSS layer increases the hole transport and injection, while the PVK layer eliminates reactions between the *p*-thiocresol-capped ZnS:Mn nanocrystals and the PEDOT-PSS layer.

5. EL emission (~600 nm) from the Mn in the ZnS nanocrystals, as well as that (~445 and ~495 nm) from the PVK was observed. The ratio of emission from Mn to that from the

PVK layer increased from 4 to 10 as the operating voltage decreased from 28 to 20 V, and from 1.3 to 4.3 as the Mn concentration increased from 0.40 to 2.14 mol %.

### 7.2 Reverse Micelle-Based CdS:Mn/ZnS Core/Shell Nanocrystals

Synthesis and characterization of efficient and photostable yellow-emitting CdS:Mn/ZnS core/shell nanocrystals via a reverse micelle route were reported.

1. Mn-doped CdS core nanocrystals were produced ranging from 1.5 to 2.3 nm in diameter with epitaxial ZnS shell of wider band gap via a reverse micelle process. For extremely small CdS nanocrystals (e.g., ~1.5 nm in diameter), Mn doping had a low probability resulting in lack of luminescence.

2. Effective passivation of the CdS:Mn core surface by a ZnS shell was evident from the absence of a surface-related defect emission and a high quantum efficiency (18 %) compared to *n*-dodecanethiol-passivated CdS:Mn nanocrystals (surface defect luminescence observed and a quantum yield of only 3.7 %).

3. Although *n*-dodecanethiol-passivated CdS:Mn nanocrystals suffered from the reduction of emission intensity during UV irradiation, ZnS-passivated CdS:Mn nanocrystals exhibited a 40 % increase in luminance during the first 90 min of UV irradiation and constant, stable luminance during continued UV irradiation.

4. XPS data revealed that $ZnSO_4$ formed on the CdS:Mn/ZnS nanocrystal surface during UV irradiation in air. This photooxidation product served as an additional passivating layer, resulting in further enhanced quantum yield and photostability because the $ZnSO_4$ is stable and the photooxidation process is irreversible.

5. An even higher quantum yield of ~28 % was estimated from *n*-dodecanethiol capped CdS:Mn/ZnS core/shell nanocrystals exposed to 350 nm UV light for 3 hr.

6. The luminescence decay lifetimes from CdS:Mn/ZnS nanocrystals were shown to be related to a slow decay (~1 msec) from Mn luminescent centers and a fast decay (~ 170 nsec) from defect centers. Time-resolved and steady-state emission spectra from ZnS-passivated CdS:Mn nanocrystals suggest that only a low density of surface states is present after ZnS passivation.

### 7.3 Electroluminescence from CdS:Mn/ZnS Core/Shell Nanocrystals

Nanocrystals with a CdS:Mn/ZnS core/shell structure with a core crystal diameter of 2.3 nm and a shell thickness of 0.4 nm were synthesized via a reverse micelle route. Hybrid electroluminescent devices with a multilayer structure were fabricated using CdS:Mn/ZnS core/shell nanocrystals and conjugated polymers (PVK and PPV).

1. In PVK-based nanocrystal devices, only orange emission from the CdS:Mn/ZnS nanocrystal layer was observed, with no emission from the PVK. On the other hand, in PPV-based nanocrystal devices, only green EL emission was observed from the PPV layer, with no emission from the nanocrystalline layer. Exclusive EL emission from a single layer of a multilayer structure resulted from radiative electron-hole recombination occurring predominantly in that layer, i.e., orange from Mn in CdS, and green from PPV.

2. The trapped-charge-limited-current (TCLC) model was found to describe the current flow behavior at voltages > 8 V of PVK-based nanocrystal hybrid EL devices.

3. PPV-only (without a nanocrystalline layer) EL devices showed much smaller current flow and weaker EL emission than PPV-based nanocrystal hybrid EL devices.

4. Two sets of energetic diagrams for PVK- and PPV-based nanocrystal device structures were proposed to interpret different EL behaviors and electrical properties. When the valence band offset was smaller than the conduction band offset (PVK-based hybrid device), recombination occurred in the nanocrystalline layer. When the conduction band

offset was less that the valance band offset (PPV-based hybrid device), recombination occurred in the conjugated polymer.

### 7.4 Silica-Overcoated CdS:Mn/ZnS Core/Shell Nanocrystals

Water-soluble CdS:Mn/ZnS quantum dots were synthesized by silica overcoating.

1. The CdS:Mn/ZnS quantum dot and silica layer were found to be ~3.2 nm in diameter and ~2.5 nm in thickness, respectively. XPS analysis confirmed that the CdS:Mn/ZnS quantum dots are overcoated by a silica shell.
2. While the silica surface coating made the quantum dots water-soluble, a silica coating on CdS:Mn dots was not sufficient to passivate the surface for photoluminescence.
3. The silica-overcoated CdS:Mn/ZnS quantum dots were shown to be stable for 90 min exposures to 385 nm UV irradiation in air, which is excellent photostability.

LIST OF REFERENCES

[1] G. Jaeckel, Z. Tech. Phys. **6,** 301 (1926).

[2] C. R. Berry, Phys. Rev. **153,** 989 (1967).

[3] C. R. Berry, Phys. Rev. **161,** 848 (1967).

[4] A. I. Ekimov and A. A. Onushchenko, Sov. Phys. Semicond. **16,** 775 (1982).

[5] L. E. Brus, J. Chem. Phys. **79,** 5566 (1983).

[6] L. E. Brus, J. Chem. Phys. **80,** 4403 (1984).

[7] C. B. Murray, D. J. Norris, and M. G. Bawendi, J. Am. Chem. Soc. **115,** 8706 (1993).

[8] W. G. Becker and A. J. Bard, J. Phys. Chem. **87,** 4888 (1983).

[9] R. N. Bhargava, D. Gallagher, X. Hong, and A. Nurmikko, Phys. Rev. Lett. **72,** 416 (1994).

[10] R. N. Bhargava, J. Lumin. **70,** 85 (1996).

[11] Y. Wang and N. Herron, J. Phys. Chem. **95,** 525 (1991).

[12] L. Brus, J. Quantum Elect. **22,** 1909 (1986).

[13] M. L. Steigerwald and L. E. Brus, Annu. Rev. Mater. Sci. **19,** 471 (1989).

[14] A. L. Efros, Sov. Phys. Semicond. **16,** 772 (1982).

[15] K. Rajeshwar, N. R. Tacconi, and C. R. Chenthamarakshan, Chem. Mater. **13,** 2765 (2001).

[16] T. Trindade, P. O'Brien, and N. L. Pickett, Chem. Mater. **13,** 3843 (2001).

[17] J. H. Adair, T. Li, T. Kido, K. Havey, J. Moon, J. Mecholsky, A. Morrone, D. R. Talham, M. H. Ludwig, and L. Wang, Mat. Sci. Eng. R **23,** 139 (1998).

[18] J. Nanda, S. Sapra, D. D. Sarma, N. Chandrasekharan, and G. Hodes, Chem. Mater. **12,** 1018 (2000).

[19] A. P. Alivisatos, J. Phys. Chem. **100,** 13226 (1996).

[20] M. Hayashi, T. Iwano, H. Nasu, K. Kamiya, N. Sugimoto, and K. Hirao, J. Mater. Res. **12,** 2552 (1997).

[21] O. AlvarezFregoso, J. G. MendozaAlvarez, and O. ZelayaAngel, J. Appl. Phys. **82,** 708 (1997).

[22] B. G. Potter and J. H. Simmons, J. Appl. Phys. **68,** 1218 (1990).

[23] M. A. Hines and P. GnyotSionnest, J. Phys. Chem. **100,** 468 (1996).

[24] V. L. Colvin, M. C. Schlamp, and A. P. Alivisatos, Nature **370,** 354 (1994).

[25] L. Xu, L. Wang, X. F. Huang, J. M. Zhu, H. M. Chen, and K. J. Chen, Physica E **8,** 129 (2000).

[26] J. E. B. Katari, V. L. Colvin, and A. P. Alivisatos, J. Phys. Chem. **98,** 4109 (1994).

[27] X. G. Peng, M. C. Schlamp, A. V. Kadavanich, and A. P. Alivisatos, J. Am. Chem. Soc. **119,** 7019 (1997).

[28] B. O. Dabbousi, J. RodriguezViejo, F. V. Mikulec, J. R. Heine, H. Mattoussi, R. Ober, K. F. Jensen, and M. G. Bawendi, J. Phys. Chem. B **101,** 9463 (1997).

[29] N. Herron, Y. Wang, and H. Eckert, J. Am. Chem. Soc. **112,** 1322 (1990).

[30] J. G. Winiarz, L. M. Zhang, M. Lal, C. S. Friend, and P. N. Prasad, J. Am. Chem. Soc. **121,** 5287 (1999).

[31] A. Agostiano, M. Catalano, M. L. Curri, M. Della Monica, L. Manna, and L. Vasanelli, Micron **31,** 253 (2000).

[32] C. Petit, T. K. Jain, F. Billoudet, and M. P. Pileni, Langmuir **10,** 4446 (1994).

[33] H. Sato, T. Hirai, and I. Komasawa, Ind. Eng. Chem. Res. **34,** 2493 (1995).

[34] J. Tanori, N. Duxin, C. Petit, I. Lisiecki, P. Veillet, and M. P. Pileni, Colloid Poly. Sci. **273,** 886 (1995).

[35] C. F. Hoener, K. A. Allan, A. J. Bard, A. Campion, M. A. Fox, T. E. Mallouk, S. E. Webber, and J. M. White, J. Phys. Chem. **96,** 3812 (1992).

[36] Z. A. Peng and X. G. Peng, J. Am. Chem. Soc. **123,** 183 (2001).

[37] J. Aldana, Y. A. Wang, and X. G. Peng, J. Am. Chem. Soc. **123,** 8844 (2001).

[38] K. Song and S. Lee, Curr. Appl. Phys. **1,** 169 (2001).

[39] A. R. Kortan, R. Hull, R. L. Opila, M. G. Bawendi, M. L. Steigerwald, P. J. Carroll, and L. E. Brus, J. Am. Chem. Soc. **112,** 1327 (1990).

[40] D. R. Vij, *Luminescence of Solids* (Plenum Press, New York, 1998).

[41] G. Blasse and B. C. Grabmaier, *Luminescent Materials* (Springer-Verlag Berlin Heidelburg, 1994).

[42] A. A. Bol and A. Meijerink, J. Lumin. **87-9,** 315 (2000).

[43] B. A. Smith, J. Z. Zhang, A. Joly, and J. Liu, Phys. Rev. B **62,** 2021 (2000).

[44] D. Gallagher, W. E. Heady, J. M. Racz, and R. N. Bhargava, J. Cryst. Growth **138,** 970 (1994).

[45] J. S. Lewis, M. R. Davidson, and P. H. Holloway, J. Appl. Phys. **92,** 6646 (2002).

[46] J. F. Wager, J. C. Hitt, B. A. Baukol, J. P. Bender, and D. A. Keszler, J. Lumin. **97,** 68 (2002).

[47] S. Gupta, J. C. McClure, and V. P. Singh, Thin Solid Films **299,** 33 (1997).

[48] M. Ihara, T. Igarashi, T. Kusunoki, and K. Ohno, J. Electrochem. Soc. **149,** H72 (2002).

[49] H. Ito, T. Takano, T. Kuroda, F. Minami, and H. Akinaga, J. Lumin. **72-4,** 342 (1997).

[50] A. A. Bol and A. Meijerink, Phys. Rev. B **58,** R15997 (1998).

[51] A. A. Bol and A. Meijerink, J. Phys. Chem. B **105,** 10197 (2001).

[52] A. A. Bol and A. Meijerink, J. Phys. Chem. B **105,** 10203 (2001).

[53] N. Murase, R. Jagannathan, Y. Kanematsu, M. Watanabe, A. Kurita, K. Hirata, T. Yazawa, and T. Kushida, J. Phys. Chem. B **103,** 754 (1999).

[54] S. Coe, W. K. Woo, M. Bawendi, and V. Bulovic, Nature **420,** 800 (2002).

[55] M. Stossel, J. Staudigel, F. Steuber, J. Simmerer, and A. Winnacker, Appl. Phys. A **68,** 387 (1999).

[56] M. Fujihira and C. Ganzorig, Mat. Sci. Eng. B **85,** 203 (2001).

[57] T. Tsutsui, Nature **420,** 752 (2002).

[58] P. E. Burrows, Z. Shen, V. Bulovic, D. M. McCarty, S. R. Forrest, J. A. Cronin, and M. E. Thompson, J. Appl. Phys. **79,** 7991 (1996).

[59] V. N. Savvateev, M. Tarabia, H. Chayet, E. Z. Farragi, G. B. Cohen, S. Kirstein, D. Davidov, Y. Avny, and R. Neumann, Synth. Met. **85,** 1269 (1997).

[60] H. Chayet, E. Z. Faraggi, H. Hong, V. N. Savvateev, R. Neumann, Y. Avny, and D. Davidov, Synth. Met. **84,** 621 (1997).

[61] M. Ben Khalifa, D. Vaufrey, A. Bouazizi, J. Tardy, and H. Maaref, Mat. Sci. Eng. C **21,** 277 (2002).

[62] A. Elschner, F. Bruder, H. W. Heuer, F. Jonas, A. Karbach, S. Kirchmeyer, and S. Thurm, Synth. Met .**111,** 139 (2000).

[63] Y. Cao, G. Yu, C. Zhang, R. Menon, and A. J. Heeger, Synth. Met. **87,** 171 (1997).

[64] J. C. Scott, J. H. Kaufman, P. J. Brock, R. DiPietro, J. Salem, and J. A. Goitia, J. Appl. Phys. **79,** 2745 (1996).

[65] J. R. Sheats, H. Antoniadis, M. Hueschen, W. Leonard, J. Miller, R. Moon, D. Roitman, and A. Stocking, Science **273,** 884 (1996).

[66] M. C. Schlamp, X. G. Peng, and A. P. Alivisatos, J. Appl. Phys. **82,** 5837 (1997).

[67] N. Tessler, V. Medvedev, M. Kazes, S. H. Kan, and U. Banin, Science **295,** 1506 (2002).

[68] M. Bruchez, M. Moronne, P. Gin, S. Weiss, and A. P. Alivisatos, Science **281,** 2013 (1998).

[69] W. C. W. Chan, D. J. Maxwell, X. H. Gao, R. E. Bailey, M. Y. Han, and S. M. Nie, Curr. Opin. Biotechnol. **13,** 40 (2002).

[70] D. R. Larson, W. R. Zipfel, R. M. Williams, S. W. Clark, M. P. Bruchez, F. W. Wise, and W. W. Webb, Science **300,** 1434 (2003).

[71] J. K. Jaiswal, H. Mattoussi, J. M. Mauro, and S. M. Simon, Nat. Biotechnol. **21,** 47 (2003).

[72] D. Gerion, F. Pinaud, S. C. Williams, W. J. Parak, D. Zanchet, S. Weiss, and A. P. Alivisatos, J. Phys. Chem. B **105,** 8861 (2001).

[73] H. Mattoussi, J. M. Mauro, E. R. Goldman, G. P. Anderson, V. C. Sundar, F. V. Mikulec, and M. G. Bawendi, J. Am. Chem. Soc. **122,** 12142 (2000).

[74] W. C. W. Chan and S. M. Nie, Science **281,** 2016 (1998).

[75] X. Y. Wu, H. J. Liu, J. Q. Liu, K. N. Haley, J. A. Treadway, J. P. Larson, N. F. Ge, F. Peale, and M. P. Bruchez, Nat. Biotechnol. **21,** 41 (2003).

[76] A. J. Sutherland, Curr. Opin. Sol. St. Mater. Sci. **6,** 365 (2002).

[77] B. Dubertret, P. Skourides, D. J. Norris, V. Noireaux, A. H. Brivanlou, and A. Libchaber, Science **298,** 1759 (2002).

[78] S. Santra, P. Zhang, K. M. Wang, R. Tapec, and W. H. Tan, Anal. Chem. **73,** 4988 (2001).

[79] G. P. Mitchell, C. A. Mirkin, and R. L. Letsinger, J. Am. Chem. Soc. **121,** 8122 (1999).

[80] H. Mattoussi, J. M. Mauro, E. R. Goldman, T. M. Green, G. P. Anderson, V. C. Sundar, and M. G. Bawendi, Phys. Status Sol. B **224,** 277 (2001).

[81] M. Y. Gao, C. Lesser, S. Kirstein, H. Mohwald, A. L. Rogach, and H. Weller, J. Appl. Phys. **87,** 2297 (2000).

[82] H. Mattoussi, L. H. Radzilowski, B. O. Dabbousi, E. L. Thomas, M. G. Bawendi, and M. F. Rubner, J. Appl. Phys. **83,** 7965 (1998).

[83] J. Lee, V. C. Sundar, J. R. Heine, M. G. Bawendi, and K. F. Jensen, Adv. Mater. **12,** 1102 (2000).

[84] W. X. Que, Y. Zhou, Y. L. Lam, Y. C. Chan, C. H. Kam, B. Liu, L. M. Gan, C. H. Chew, G. Q. Xu, S. J. Chua, S. J. Xu, and F. V. C. Mendis, Appl. Phys. Lett. **73,** 2727 (1998).

[85] M. Y. Gao, B. Richter, S. Kirstein, and H. Mohwald, J. Phys. Chem. B **102,** 4096 (1998).

[86] M. V. Artemyev, V. Sperling, and U. Woggon, J. Appl. Phys. **81,** 6975 (1997).

[87] J. M. Huang, Y. Yang, S. H. Xue, B. Yang, S. Y. Liu, and J. C. Shen, Appl. Phys. Lett. **70,** 2335 (1997).

[88] W. Chen, R. Sammynaiken, Y. N. Huang, J. O. Malm, R. Wallenberg, J. O. Bovin, V. Zwiller, and N. A. Kotov, J. Appl. Phys. **89,** 1120 (2001).

[89] C. Benecke and H.-E. Gumlich, Semicond. Semimet. **25,** 85 (1988).

[90] D. Gallagher, W. E. Heady, J. M. Racz, and R. N. Bhargava, J. Mater. Res. **10,** 870 (1995).

[91] S. E. Shaheen, G. E. Jabbour, B. Kippelen, N. Peyghambarian, J. D. Anderson, S. R. Marder, N. R. Armstrong, E. Bellmann, and R. H. Grubbs, Appl. Phys. Lett. **74,** 3212 (1999).

[92] L. Chkoda, C. Heske, M. Sokolowski, E. Umbach, F. Steuber, J. Staudigel, M. Stossel, and J. Simmerer, Synth. Met. **111,** 315 (2000).

[93] A. P. Alivisatos, Science **271,** 933 (1996).

[94] M. Nirmal and L. Brus, Acc. Chem. Res. **32,** 407 (1999).

[95] M. Kuno, J. K. Lee, B. O. Dabbousi, F. V. Mikulec, and M. G. Bawendi, J. Chem. Phys. **106,** 9869 (1997).

[96] C. M. Jin, J. Q. Yu, L. D. Sun, K. Dou, S. G. Hou, J. L. Zhao, Y. M. Chen, and S. H. Huang, J. Lumin. **66-7,** 315 (1995).

[97] D. J. Norris, N. Yao, F. T. Charnock, and T. A. Kennedy, Nano Lett. **1,** 3 (2001).

[98] H. Yang and P. H. Holloway, Appl. Phys. Lett. **82,** 1965 (2003).

[99] L. Manna, E. C. Scher, L. S. Li, and A. P. Alivisatos, J. Am. Chem. Soc. **124,** 7136 (2002).

[100] A. A. Bol, R. van Beek, J. Ferwerda, and A. Meijerink, J. Phys. Chem. Solids **64,** 247 (2003).

[101] J. F. Suyver, S. F. Wuister, J. J. Kelly, and A. Meijerink, Phys. Chem. Chem. Phys. **2,** 5445 (2000).

[102] C. R. Brundle in *Encyclopedia of Materials Characterization*, Edited by C. R. Brundle, C. A. Evans, Jr. and S. Wilson (Butterworth-Heinemann, Boston, 1992).

[103] C. D. Wagner, W. M. Riggs, L. E. Davis, J. F. Moulder, and G. E. Mullenberg, *Handbook of X-ray Photoelectron Spectroscopy* (Perkin Elmer Corp., Eden Prarie, MN, 1979).

[104] M. Behboudnia and P. Sen, Phys. Rev. B **6303,** 035316 (2001).

[105] Joint Committee on Powder Diffraction Standards (JCPDS), International Center for Diffraction Data (ICDD), Swarthmore, PA.

[106] H. Yang, P. H. Holloway, and B. B. Ratna, J. Appl. Phys. **93,** 586 (2003).

[107] L. Levy, D. Ingert, N. Feltin, and M. P. Pileni, J Cryst. Growth **185,** 377 (1998).

[108] L. D. Sun, X. F. Fu, M. W. Wang, C. H. Liu, C. S. Liao, and C. H. Yan, J. Lumin. **87-9,** 538 (2000).

[109] S. M. Liu, F. Q. Liu, H. Q. Guo, Z. H. Zhang, and Z. G. Wang, Solid State Comm. **115,** 615 (2000).

[110] J. Z. Zhang, Acc. Chem. Res. **30,** 423 (1997).

[111] M. Nirmal, C. B. Murray, D. J. Norris, and M. G. Bawendi, Zeitschrift Fur Physik D **26,** 361 (1993).

[112] T. Kubo, T. Isobe, and M. Senna, J. Lumin. **99,** 39 (2002).

[113] X. Pingbo, Z. Weiping, Y. Min, C. Houtong, Z. Weiwei, L. Liren, and X. Shangda, J. Colloid Interf. Sci. **229,** 534 (2000).

[114] K. Yoshino, A. S. C. Cheung, J. R. Esmond, W. H. Parkinson, D. E. Freeman, S. L. Guberman, A. Jenouvrier, B. Coquart, and M. F. Merienne, Planet Space Sci. **36,** 1469 (1988).

[115] C. Ehrlich, W. Busse, H. E. Gumlich, and D. Tschierse, J. Cryst. Growth **72,** 371 (1985).

[116] W. Chen, D. Grouquist, and J. Roark, J. Nanosci. Nanotechnol. **2,** 47 (2002).

[117] B. O. Dabbousi, M. G. Bawendi, O. Onitsuka, and M. F. Rubner, Appl. Phys. Lett. **66,** 1316 (1995).

[118] H. Y. Jeong, Y. K. Lee, A. Talaie, K. M. Kim, Y. D. Kwon, Y. R. Jang, K. H. Yoo, D. J. Choo, and J. Jang, Thin Solid Films **417,** 171 (2002).

[119] S. M. Sze, *Physics of Semiconductor Devices* (John Wiley & Sons, New York, 1981).

[120] H. Yang and P. H. Hollway, Accepted for the publication in Adv. Funct. Mater.

[121] G. Hernandez-Padron, F. Rojas, M. Garcia-Garduno, M. A. Canseco, and V. M. Castano, Mat. Sci. Eng. Struct. **355,** 338 (2003).

[122] G. Orcel, J. Phalippou, and L. L. Hench, J. Non-Cryst. Solids **88,** 114 (1986).

[123] J. R. Ferraro and M. Manghnan, J. Appl. Phys. **43,** 4595 (1972).

## BIOGRAPHICAL SKETCH

Heesun Yang was born in Seoul, Republic of Korea. He grew up and was educated in his hometown. He entered the Department of Ceramic Engineering at Yonsei University in 1989 to study materials science and engineering. After he finished the first two years of undergraduate course, he joined the army (KATUSA: Korean Augmentation to the United States Army) for 30 months to accomplish mandatory service. After return from army service, he rejoined the school and obtained his bachelor's degree in 1996. He continued his study and obtained his master's degree in 1998. The research topics for his master's degree were synthesis and characterization of silica aerogel thin film through ambient pressure drying for the application to intermetallic dielectric (IMD) component. After graduation, he remained at the university as a post-graduate research assistant, and then was hired by LG Electronics (Display R&D Center) as an assistant research engineer. His field at LG Electronics was the development of lower panel of plasma display panel (PDP) for the purpose of cost-down. In 1999, he was admitted to the Department of Materials Science and Engineering at the University of Florida to pursue his Ph.D degree with a specialty in electronic materials. His research areas at Dr. Holloway's group were synthesis and characterization of Mn-doped II-VI semiconductor nanocrystals. Furthermore, he extended his research interests into the application of Mn-doped semiconductor nanocrystals to electroluminescent (EL) devices and biological labels. He obtained his non-thesis Master of Science in December of 2002, and Ph.D. degree in December of 2003.

I certify that I have read this study and that in my opinion it conforms to acceptable standards of scholarly presentation and is fully adequate, in scope and quality, as a dissertation for the degree of Doctor of Philosophy.

Paul H. Holloway, Chairman
Distinguished Professor of Materials Science and Engineering

I certify that I have read this study and that in my opinion it conforms to acceptable standards of scholarly presentation and is fully adequate, in scope and quality, as a dissertation for the degree of Doctor of Philosophy.

David Norton
Professor of Materials Science and Engineering

I certify that I have read this study and that in my opinion it conforms to acceptable standards of scholarly presentation and is fully adequate, in scope and quality, as a dissertation for the degree of Doctor of Philosophy.

Wolfgang Sigmund
Associate Professor of Materials Science and Engineering

I certify that I have read this study and that in my opinion it conforms to acceptable standards of scholarly presentation and is fully adequate, in scope and quality, as a dissertation for the degree of Doctor of Philosophy.

Darryl Butt
Associate Professor of Materials Science and Engineering

I certify that I have read this study and that in my opinion it conforms to acceptable standards of scholarly presentation and is fully adequate, in scope and quality, as a dissertation for the degree of Doctor of Philosophy.

David Tanner
Professor of Physics

This dissertation was submitted to the Graduate Faculty of the College of Engineering and to the Graduate School and was accepted as partial fulfillment of the requirements for the degree of Doctor of Philosophy.

December, 2003

Pramod Khargonekar

Pramod P. Khargonekar
Dean, College of Engineering

Winfred M. Phillips
Dean, Graduate School